Graz University of Technology

Doctoral Thesis

Low-Complexity Localization using Standard-Compliant UWB Signals

Dipl.-Ing. Thomas Gigl, Bakk. techn.

Signal Processing and Speech Communication Laboratory
Graz University of Technology, Austria

Supervisor and First Examiner:
Assoc.-Prof. Dipl.-Ing. Dr. Klaus Witrisal
Graz University of Technology, Austria

Second Examiner:
Univ.-Prof. Dipl.-Ing. Dr.-Ing. Christoph Mecklenbräuker
Vienna University of Technology, Austria

Graz, December 2010

EIDESSTATTLICHE ERKLÄRUNG

Ich erkläre an Eides statt, dass ich die vorliegende Arbeit selbstständig verfasst, andere als die angegebenen Quellen/Hilfsmittel nicht benutzt, und die den benutzten Quellen wörtlich und inhaltlich entnommene Stellen als solche kenntlich gemacht habe.

Graz, am ....

(Unterschrift)

Kurzfassung

Diese Arbeit konzentriert sich auf die Analyse von Lokalisierungssystemen mit geringer Komplexität. Es ist bekannt, dass Ultra-Breitband (Ultra-Wideband, UWB) Signale robuste und genaue Lokalisierung sogar in reflexionsreichen Umgebungen ermöglichen. Allerdings bedeutet dessen sehr große Bandbreite auch sehr hohe Anforderungen an den Empfänger und es lassen sich diese Vorteile mit herkömmlichen Empfängerstrukturen kaum realisieren.

Der Energiedetektor ist eine vielversprechende Alternative. Im Gegensatz zu hoch komplexen kohärenten Empfängerstrukturen hängt aber das Ausgangssignal stark von den Systemparametern und den verwendeten Signalen ab. IEEE 802.15.4a ist derzeit der einzige Standard, der ein hoch genaues Lokalisierungssystem definiert (Genauigkeit besser als 1 m). Der Standard definiert sehr viele Systemparameter, welche in der gesamten Arbeit in Hinblick auf die Lokalisierungsfähigkeit untersucht werden. Diese Parameter haben auch einen starken Einfluss auf die erlaubte Sendeenergie und damit auf die Reichweite des Lokalisierungssystems. Daher wird die maximale Reichweite für Energiedetektoren und kohärente Empfänger studiert. Diese Analyse basiert auf dem Link Budget, der Modellierung der FCC/CEPT Regulierungen und auf statistischen Modellen der Empfängerstrukturen.

Es wurde ein UWB Demonstrator System für Lokalisierungsexperimente entwickelt. Der IEEE 802.15.4a Standard wurde implementiert und das System wurde auf die FCC/CEPT Regulierungen kalibriert. Die Datenverarbeitung erfolgt offline, um ein hohes Maß an Flexibilität zu gewährleisten. In dieser Arbeit wird der Demonstrator für das Messen von Kanalimpulsantworten in einer umfangreichen Messkampagne in Indoor und Outdoor Umgebungen eingesetzt. Mit diesen Messungen wird die Inter-Puls-Interferenz von Energiedetektoren in IEEE 802.15.4a analysiert. Außerdem werden die Kanäle mittels Pathloss Modell und Root Mean Square (RMS) Delay Spread charakterisiert.

Abschließend wird ein System-Level Simulator für Positionierung und Tracking (U-SPOT) präsentiert. Dieser dient zur Evaluierung der Einflüsse von Systemparametern und Algorithmen auf die Gesamtleistung des Lokalisierungssystems. Der Simulator basiert auf den übrigen Ergebnissen der Arbeit. Die Kanalmessungen, die Kanalmodelle, die Link Budgets, das Modell für die Regulierungen und die Empfängerstrukturen werden zu einem neuartigen statistische Simulationskonzept kombiniert. In dieser Arbeit wird mit U-SPOT der Einfluss von Links ohne direkte Sichtverbindung auf die Positionsschätzung von IEEE 802.15.4a untersucht.

Es werden sub-meter Genauigkeiten für beide Empfängerstrukturen mit und ohne direkte Sichtverbindung erreicht. Also eignen sich auch Energiedetektoren sehr gut für Lokalisierungssysteme mit niedriger Komplexität. Überraschenderweise sind Entfernungsschätzungen mit IEEE 802.15.4a für kohärente Empfänger bis einige tausend Meter und für Energiedetektoren bis einige hundert Meter möglich. Ein längerer Abstand zwischen den Pulsen führt zu zwei Vorteilen: Erstens, der Effekt von Inter-Puls-Interferenz kann reduziert werden und zweitens ist mehr Sendeenergie erlaubt, was wiederum zu größeren Reichweiten führt.

Abstract

This thesis puts a focus on the analysis of key aspects of low-complexity Ultra Wideband (UWB) localizations systems. It is well known that UWB allows for highly robust and accurate ranging even in multipath intensive environments. On the other hand, the huge bandwidth leads to very challenging receiver designs and so low complexity and low power consumption are not achieveable for common receiver structures.

The energy detector is a promising alternative. But in contrast to high-complexity coherent receivers, their performance is strongly dependent on the system parameters of the air interface protocol. IEEE 802.15.4a is a UWB standard with high-precision localization capability (better than 1m). The standard defines many system parameters, whose impact on the ranging and localization performance is studied in the thesis. These parameters have also a significant impact on the maximum allowed transmit energy, which limits the operating range of the localization system. Thus, the maximum operating distance is analyzed for energy detectors and coherent receivers. The analysis is based on a link budget according to the FCC/CEPT regulations and on statistical models of the receiver structures.

A UWB demonstrator system has been developed for ranging and positioning experiments. The IEEE 802.15.4a standard has been implemented and the system satisfies the FCC/CEPT regulations. The processing is held offline to achieve high flexibility. In this work, the demonstrator system is used to measure channel impulse responses in an extensive measurement campaign in indoor and outdoor environments. These measurements are used to study inter-pulse-interference (IPI) of energy detectors in IEEE 802.15.4a. The channels are characterized with the parameterization of a pathloss model and their root mean square (RMS) delay spread.

Finally, a system-level simulator for positioning and tracking (U-SPOT) is presented to evaluate the influence of system parameters and algorithms on the overall performance of a localization system. The simulator is based on the other outcomes of the thesis, where the measurements, channel models, link budgets, and the receiver structures are combined to form a novel statistically defined simulation framework. In this work, U-SPOT is used to study the influence of NLOS links on the localization performance of IEEE 802.15.4a.

Sub-meter accuracies are achieved by both receivers in LOS and NLOS situations. That is, energy detectors are suitable for low-complexity localization systems. Surprisingly, ranging based on IEEE 802.15.4a is possible up to several thousands of meters for coherent receivers. Even for the low-complexity energy detector, up to several hundreds of meters are achieved. A longer spacing of the pulse sequences leads to two advantages: First, it reduces inter-pulse-interference and second, more transmit power is allowed by the FCC/CEPT regulations, which leads to longer operating distances.

Danke

An dieser Stelle möchte ich mich herzlich bei allen bedanken, die mich in den letzten Jahren bei meiner Arbeit unterstützt haben.

Lieber Klaus, herzlichen Dank für die ausgezeichnete Betreuung. Ich werde mich immer gerne an die netten und ausführlichen Diskussionen erinnern, die mich in meiner Arbeit aber auch persönlich sehr viel weitergebracht haben. Meine Ideen konnte ich immer ausführlich mit dir diskutieren und gemeinsam weiterentwicklen. Dies und deine konstruktive Kritik habe ich immer sehr geschätzt. Ohne dich wäre diese Arbeit in dieser Form nicht möglich gewesen. Danke, Herr Assoc.-Prof. Dr. Klaus Witrisal (SPSC, TU Graz)!

Lieber Joe, vielen Dank für die Zusammenarbeit in den letzten Jahren. Du hast mich immer hervorragend unterstützt und von Anfang an habe ich mich immer auf dich verlassen können. Diese Unterstützung und die Möglichkeit meine Ideen immer frei umsetzen zu können haben wesentlich zum Erfolg der Arbeit beigetragen. Danke, Herr Dipl.-Ing. Josef Preishuber-Pflügl (CISC Semiconductor)!

Herzlichen Dank an Thomas Buchgraber, Berhard Geiger, Benjamin Till und Harald Kröll, die mit ihren Projekt-, Master- und Diplomarbeiten einen wertvollen Beitrag zu meiner Arbeit geleistet haben.

Lieber Herr Univ.-Prof. Dr. Gernot Kubin (SPSC, TU Graz) und Herr Dr. Markus Pistauer (CISC Semiconductor), danke für die Möglichkeit dieses Projekts durchführen zu können. Eure Unterstützung während der letzten Jahre hatte einen großen Anteil am Erfolg des Projekts. Danke an das gesamte SPSC- und CISC-Team für das gute Arbeitsklima und die Unterstützung. Ganz besonderen Dank an Daniel Arnitz für das Reviewen meiner Thesis und die gute Zusammenarbeit. Vielen Dank auch an das administrative Team Karin, Markus und Andreas für die Entlastung während des Projekts.

Danke an unsere Projektpartner von der TU Wien, Frau Dipl.-Ing. Ayse Adalan und Herr Univ.-Prof. Dr.-Ing. Christoph Mecklenbräuker für eure Unterstützung bezüglich des Demonstrators. Ihr habt unser Projekt immer tatkräftigt mit neuer Hardware versorgt, ohne die einige Ergebnisse kaum möglich gewesen wären. Herrn Univ.-Prof. Mecklenbräuker danke ich außerdem für die Begutachtung meiner Arbeit und dass er sich als Prüfer zur Verfügung gestellt hat. Danke an Florian Trösch (ETH Zürich) für die Unterstützung beim Link Budget Paper!

Mein größter Dank geht an meinen Vater Johann und meine Mutter Helene Gigl für die unbezahlbare Unterstützung in allen Bereichen meines Lebens während meiner Ausbildungszeit. Auch möchte ich mich bei meinen Freunden und meiner Schwester Karin für den nötigen Ausgleich bedanken! Vielen Dank an Christoph Meszaros und Mitja Koren für die Englischkorrektur. Abschließend bedanke ich mich bei meiner Freundin Brigitte Jud. Vielen Dank für deine Unterstützung, dein Verständnis und dass du mich bis zum Schluss motiviert hast. Bussi!

Contents

List of Tables

List of Abbreviations

AIP	Air Interface Protocol	(Section 1.5.1)
AWGN	Additive White Gaussian Noise	(Section 5.1.3)
BMVIT	Bundesministerium für Verkehr, Innovation und Technologie (Federal Ministry for Transport, Innovation and Technology)	(Section 1.3)
BPM	Burst Position Modulation	(Section 2.1)
BPSK	Binary Phase Shift Keying	(Section 2.1)
CDF	Cumulative Distribution Function	(Section 3.5.3)
CEPT	Conférence Européenne des Postes et Télécommunications	(Section 5)
CIR	Channel Impulse Reponse	(Section 1.5.1)
CLK	CLocK	(Section 3.1)
CR	Coherent Receiver	(Section 1.5.1)
CSS	Chirp Spread Spectrum	(Section 2.2)
DAA	Detect And Avoid	(Section 5.2)
DSO	Digital Storage Oscilloscope	(Section 3.1)
DSP	Digital Signal Processor	(Section 3)
DSSS	Direct Sequence Spread Spectrum	(Section 1.2)
ECMA	European Computer Manufacturers Association	(Section 1.1)
ED	Energy Detector	(Section 1.5.1)
EIRP	Equivalent Isotropically Radiated Power	(Section 2.2)
EKF	Extended Kalman Filter	(Section 1.5.1)
ESD	Energy Spectral Density	(Section 5.2)
FCC	Federal Communication Commission	(Section 1.2)
FFD	Full Functional Devices	(Section 2.1)
FFG	ForschungsFörderungsGesellschaft (Austrian Research Agency)	(Section 1.3)
FIT-IT	Forschung, Innovation, Technology - Informations Technologie (Research, Innovation, Technology - Information Technology)	(Section 1.3)
FoM	Figure of Merrit	(Section 2.1)
FPGA	Field Programable Gate Array	(Section 3.1)
GPP	General Purpose Processor	(Section 3)
GPS	Global Positioning System	(Section 1)
GSM	Global System for Mobile communications	(Section 3.1)
HAT	Hardware action group for Active Tagging	(Section 1.2)
IEC	International Electronical Commission	(Section 1.2)

IEEE	Institut for Eletrical and Electronic Engineers	(Section 1.2)
IPI	Inter Pulse Interference	(Section 1.3)
IR	Impulse Radio	(Section 1.2)
ISM	Industrial, Scientific and Medical	(Section 1.2)
ISO	International Standardization Organization	(Section 1.2)
I/O	Input / Output	(Section 3.1)
JBSF	Jump Back and Search Forward	(Section 4.3)
kbps	kilo bits per second	(Section 1.2)
LDC	Low Duty Cycle	(Section 2.2)
LE	Location Estimation	(Section 6.1)
LNA	Low Noise Amplifier	(Section 3.1)
LOS	Line Of Sight	(Section 1.5.1)
LPF	Low Pass Filter	(Section 3.2)
LS	Least Squares	(Section 1.5.1)
LSF	Large Scale Fading	(Section 1.5.1)
LSIR	LOS Signal to IPI Ratio	(Section 4.4)
LSNCR	LOS Signal to signal-by-Noise Cross term Ratio	(Section 4.4)
LSNR	LOS Signal to Noise Ratio	(Section 4.4.2)
MAC	Medium Access Control layer	(Section 1.2)
MAE	Mean Absolute Error	(Section 4.1)
MB-OFDM	MultiBand - Orthogonal Frequency Division Multiplexing	(Section 1.1)
Mbps	Mega bits per second	(Section 1.1)
MES	Maximal Energy Selection	(Section 4.3)
MF	Matched Filter	(Section 3.2)
MGT	Multi-Giga-bit Transceivers	(Section 3.1)
MRF	Mean pulse Repetition Frequency	(Section 3.3)
ND	Noise Dimentionality	(Section 4.4)
NLOS	Non Line Of Sight	(Section 1.5.1)
ns	nano seconds	(Section 1.1)
OFDM	Orthogonal Frequency Division Multiplexing	(Section 1.1)
PHY	PHYsical layer	(Section 1.2)
PL	PathLoss	(Section 3.5.2)
PRF	Peak pulse Repetition Frequency	(Section 3.1)
PSD	Power Spectral Density	(Section 2.2)

PVA	Position Velocity Acceleration	(Section 6.3.5)
RAP	Ranging Authentication Packet	(Section 2.1)
RDEV	Ranging DEVice	(Section 2.1)
RF	Radio Frequency	(Section 6.1)
RFD	Reduced Functional Devices	(Section 2.1)
RFID	Radio Frequency IDentification	(Section 1)
RMS	Root Mean Square	(Section 1.5.1)
RRC	Root Raised Cosine	(Section 3.1)
RTLS	Real Time Locating Systems	(Section 1.2)
RX	Receiver	(Section 3.5.1)
SDS	Symmetrical Double Sided	(Section 1.1)
SFD	Start of Frame Delimiter	(Section 2.1)
SHR	Synchronization Header	(Section 2.1)
SKF	Standard Kalman Filter	(Section 1.5.1)
SLAM	Simultaneous Localization And Mapping	(Section 1)
SNR	Signal to Noise Ratio	(Section 2.1)
SSF	Small Scale Fading	(Section 3.5.1)
SySe	Synchronization and Seperation	(Section 3.2)
TDoA	Time Difference of Arrival	(Section 1.2)
ToA	Time of Arrival	(Section 1.2)
TW-ToA	Two-Way Time-of-Arrival	(Section 1.1)
TX	Transmitter	(Section 3.5.1)
UHF	Ultra High Frequency	(Section 6)
USB	Universal Serial Bus	(Section 1.1)
UWB	Ultra WideBand	(Section 1.2)
U-SPOT	Ultra wideband system level Simulator for Positioning and Tracking	(Section 1.5.1)
VSG	Vector Signal Generator	(Section 3.1)
WLAN	Wireless Local Area Network	(Section 1)
WP	Working Point	(Section 4.4.3)
WSN	Wireless Sensor Network	(Section 1)

Signals and Variables

$\mathbf{1}_x$	Vector of ones with length x	(Section 3.3)
a	Acceleration of the mobile	(Section 6.3.5)
$\mathbf{A}$	State transition matrix	(Section 6.3.5)
a_x	Acceleration of the mobile in x-direction	(Section 6.3.5)
a_y	Acceleration of the mobile in y-direction	(Section 6.3.5)
B	Pulse bandwidth	(Section 1.1)
$\mathbf{B}$	State noise relation matrix	(Section 6.3.5)
B_s	Signal bandwidth	(Section 1.1)
B_{av}	Resolution bandwidth of the averaging limit defined by FCC	(Section 5.2)
B_{pk}	Resolutoin bandwidth of the peak power limit defined by FCC	(Section 5.2)
c	User defined threshold for ranging	(Section 4.3)
$\mathbf{c}$	Preamble code	(Section 3.2)
$\mathbf{C}$	Measurement covariance matrix	(Section 6.3.5)
$\mathring{\mathbf{c}}$	Communication despreading code	(Section 3.2)
$\tilde{\mathbf{c}}$	Preamble symbol despreading code	(Section 4.1)
$\mathbf{c}_{\text{auto}}$	Preamble symbol code after autocorrelation	(Section 3.3)
c_{opt}	Optimal user defined threshold	(Section 4.3)
$\mathbf{c_s}$	Preamble symbol code	(Section 3.3)
$\mathbf{c_{sp}}$	Spread preamble code	(Section 3.3)
$\mathbf{c}_{\text{NZM}}$	Non-Zero-Mean despreading code	(Section 4.2)
$\mathbf{c}_{\text{ZM}}$	Zero-Mean despreading code	(Section 4.2)
Δ	Code delay	(Section 3.4)
Δt	Update duration	(Section 6.3.5)
δ_L	Unit vector with 1 at the first position and length L	(Section 3.3)
d_0	Reference distance	(Section 3.5.2)
$d_{\text{BS}i}$	Range to the i-th base station	(Section 6.3.4)
d_{max}	Maximal operating distance	(Section 5.1.4)
e_d	Distance error	(Section 4.3)
E_{LOS}	Energy of the LOS component	(Section 4.4.2)
E_p	Energy per pulse	(Section 3.3)
E_{pr}	Preamble Energy	(Section 5.1.5)
$E_{\text{p,av}}$	Energy per pulse limited by average power limit	(Section 5.2)
$E_{\text{p,pk}}$	Energy per pulse limited by peak power limit	(Section 5.2)

E_{rp}	Received preamble energy	(Section 4.4.1)
ERF	Effective pulse repetition frequency	(Section 3.3)
η	Pathloss exponent	(Section 3.5.2)
F	Noise figure	(Section 5.3)
f_c	Carrier fequency or center frequency	(Section 1.1)
$g(t)$	Channel response passband	(Section 4.2)
$\tilde{g}(t)$	Filtered channel response passband	(Section 4.2.2)
G_{RX}	Receive antenna gain	(Section 3.1)
G_{TX}	Transmit antenna gain	(Section 3.1)
γ	Threshold for ranging	(Section 4.3)
$h(t)$	Equivalent channel response	(Section 3.3)
$\mathbf{H}$	Observation matrix	(Section 6.3.5)
$h_c(t)$	Channel impulse response	(Section 3.3)
h_{hilb}	Impulse response Hilbert filter	(Section 3.3)
$\mathbf{I}$	Identity matrix	(Section 6.3.5)
$\mathbf{J}$	Jacobian matrix	(Section 6.3.4)
$\mathbf{K}$	Kalman gain matrix	(Section 6.3.5)
κ	Boltzmann constant	(Section 5.3)
L	Code spreading length	(Section 3.3)
L_{imp}	Implementation losses	(Section 5.3)
LSIR	LOS signal to IPI ratio	(Section 4.4)
LSNCR	LOS signal to signal-by-noise-cross term ratio	(Section 4.4)
LSNR	LOS SNR	(Section 4.4)
M	Number of code elements	(Section 3.3)
M_1	Number of transmitted pulses	(Section 3.3)
M_F	Fading margin	(Section 5.3)
MRF	Mean pulse repetition frequency	(Section 3.3)
n	Time index (sampled)	(Section 3.3)
N	Number of base stations	(Section 6.3)
N_{chip}	Number of samples per chip	(Section 4.2)
$N_{\hat{h}}$	Length of the matched-filter	(Section 3.3)
N_s	Preamble sequence code length	(Section 2.1)
N_{sync}	Preamble symbol repetitions	(Section 3.3)
N_0	Noise spectral density	(Section 4.2.2)

$N_{1\text{ms}}$	Number of pulses within 1 ms	(Section 3.3)
ND	Noise dimentionality	(Section 4.4)
$\nu(t)$	Additive white Gaussian noise	(Section 1.3)
$\nu_{\text{BP}}(t)$	Band pass filtered additive white Gaussian noise	(Section 4.2)
$\nu_{\text{LP}}(t)$	Low pass filtered additive white Gaussian noise	(Section 3.3)
O_{CR}	Operations of the coherent receiver	(Section 5.4.3)
O_{ED}	Operations of the energy detector	(Section 5.4.3)
ω_c	Angular carrier or center frequency	(Section 3.2)
$P_{\text{av}}^{\text{FCC}}$	Maximal allowed average power by FCC	(Section 5.2)
$\mathbf{P}_k$	Error covariance matrix	(Section 6.3.5)
P_{LOS}	Probability for a LOS links	(Section 6.2)
P_N	Probability of N NLOS links	(Section 6.2)
$P_{\text{pk}}^{\text{FCC}}$	Maximal allowed peak power by FCC	(Section 5.2)
P_s	Switching probability	(Section 6.2)
P_T	Transition probability	(Section 6.2)
P_{TX}	Transmit power	(Section 3.5.2)
PL	Pathloss	(Section 3.5.2)
$\text{PL}^{(d)}$	Distance dependent pathloss	(Section 5.1.5)
PL_{FS}	Free-space pathloss	(Section 3.5.2)
PL_{max}	Maximal allowed pathloss	(Section 5.1.5)
PRF	Peak pulse repetition frequency	(Section 3.1)
P_{RX}	Receive power	(Section 3.5.2)
φ	Carrier phase	(Section C.1)
$\phi_a(t)$	Autocorrelation function	(Section 4.2)
$\phi_{\tilde{c}cc}$	Code despreading function	(Section 4.2.1)
$\phi_{\tilde{w}}(0)$	Equivalent bandwidth	(Section 4.2.3)
$\mathbf{Q}$	State covariance matrix	(Section 6.3.5)
$r(t)$	Received signal	(Section 1.3)
R	Pulse repetition rate	(Section 6.2)
$\mathbf{R}$	SySe matrix	(Section 3.3)
$\tilde{r}(t)$	Noise free received signal	(Section 1.3)
$r_a(t)$	Received analog signal	(Section 3.3)
r_{BP}	Bandpass filtered received signal	(Section 4.2)
$s(t)$	Transmitted signal	(Section 3.3)

σ_n^2	Variance of the additive white Gaussian noise	(Section 3.3)
t	Time	(Section 3.3)
T	Sampling interval	(Section 3.2)
T_0	Reference temperature	(Section 5.3)
T_{av}	Averaging time defined by FCC	(Section 5.2)
T_{chip}	Chip duration	(Section 3.3)
T_I	Integration time	(Section 4.1)
T_{psym}	Preamble symbol duration	(Section 3.4)
T_{round}	Round trip time	(Section 2.1)
T_{sync}	Preamble duration	(Section 3.3)
T_s	Preamble symbol duration	(Section 4.2.1)
T_{sb}	Duration of the search-back window	(Section 4.3)
T_t	Travel time of the signal	(Section 2.1)
T_{ta}	Turn around time RDEV A	(Section 2.1)
$\tau_{\max}$	Maximal access delay	(Section 3.4)
τ_{RMS}	Root-Mean-Square delay spread	(Section 3)
$\hat{\tau}_{\mathrm{LOS}}$	Estimated time-of-arrival	(Section 4.3)
$\mathbf{u}$	State noise vector	(Section 6.3.5)
v	Velocity of the mobile	(Section 6.3.5)
v_x	Velocity of the mobile in x-direction	(Section 6.3.5)
v_y	Velocity of the mobile in y-direction	(Section 6.3.5)
$w(t)$	Pulse shape	(Section 3.3)
$\tilde{w}(t)$	Upconverted pulse	(Section 4.2)
W_{RRC}	Equivalent bandwidth	(Section 4.2.3)
w_{sb}	Size of the search-back window	(Section 4.3)
WP	Working Point	(Section 4.4)
$\mathrm{WP}_{\mathrm{LSNR}}$	Working Point defined by LSNR	(Section 4.4)
WP_{E_p/N_0}	Working Point defined by E_p/N_0	(Section 4.4)
$x[n]$	Energy detector output	(Section 4.2)
$\mathbf{x}$	State vector	(Section 6.3.4)
X	Length of the trajectory	(Section 6.3.6)
$\mathbf{x}_{\mathrm{BS}i}$	Coordinates of the i-th base station	(Section 6.3.4)
$\mathbf{x}_c$	Coordinates of the mobile	(Section 6.3.4)
$\mathbf{x}_{\mathrm{LS}}$	Coordinates of the mobile estimated by least squares	(Section 6.3.4)

$\mathbf{x}_0$	Linearization coordinates	(Section 6.3.4)
$y[n]$	Estimated channel response by the energy detector	(Section 4.2)
ζ	Speed of the light	(Section 4.3)

Operators

General Notation

$\otimes$	Kronecker product
$*$	Convolution
$\mathbf{a}$	Vector a (bold lower case letter)
$\mathbf{A}$	Matrix A (bold upper case letter)
A^-	Prediced value of A
$\bar{a}$	Mean value of a
$\hat{a}$	Estimated value of a
$\|\|.\|\|$	Euclidean norm
$(.)^T$	Transpose matrix
cov$\{.,.\}$	Covariance
E$\{.\}$	Expected value
var$\{.\}$	Variance

1 Introduction

Nowadays wireless communication devices make our life easier and faster. Nearly everyone uses cell phones, Wireless LAN, the Global Positioning System (GPS), keyless entry systems, etc. It allows us to stay in contact with everyone, everywhere, at anytime, it provides to be connected to the internet, can be used for navigation, gives access to secure areas, and much more. In particular location awareness in wireless systems is getting of special interest to the industry and the research communities in recent years, with new emerging applications, e.g. (cf. [1]):

- Personal safety
  - Tracking & navigation of fire fighters [2], military personnel, and police officers [3]
  - Tracking of children and pets
- Indoor and urban canyon navigation
  - Guidance of museum visitors, passengers at airports and train stations, pedestrians at shopping centers
- Sensor networks
  - Environmental sensing, structural monitoring
- Intelligent transport systems
  - Self driving vehicles, car-to-car communication
- Inventory control
  - Tracking of goods, items, and medical equipment in hospitals
- Smart homes
  - Automatic doors,...

These applications need accurate positioning in indoor and outdoor scenarios with high reliability. Often the identification of objects with their location and some sensor data is desired. Such systems are realized as radio frequency identification (RFID) and wireless sensor networks (WSN). Battery supported systems are usually preferred to enlarge the operating distance. RFID and WSN systems need to handle hundreds or thousands of mobiles (tags), thus low cost becomes a key topic. As the replacement of the battery for such large amounts of mobile devices is quite expensive, low power consumption is crucial. Furthermore, a small form factor is required, that the sensing can take place where the desired observation is needed. High robustness against interference, small-scale fading and shadowing is required, because many applications need to work in multipath intensive environments (cf.[4]).

Similar requirements are given for the navigation and the tracking of fire fighters, law enforcement officers, and military personal [3]. E.g. the system has to be highly robust, should have small form factors, should not require a pre-installation of the system, should allow integrity monitoring and the extension by sensors for physiological monitoring, should implement simultaneous localization and mapping (SLAM), should have accuracies better than 1 m horizontal and 2 m vertical in any environment, etc.

The well established Global Positioning System (GPS) is designed for outdoor navigation. There it offers an accuracy of several meters[1]. In indoor environments the signals are often unable to penetrate the roof or the walls and get disturbed by multipath reflections. Additionally the complexity of GPS receivers is rather high, which leads to high power consumption.

Thus, special terrestrial localization solutions are necessary for the individual requirements of the specific applications. An overview on the current standardization activities for real time localization systems (RTLS) and WSN is given in Section 1.2. Ultra Wideband (UWB) signals show very interesting features for RTLS, WSN, and other localization systems. Thus it is the key technology of this work and an overview is given in the next section.

1.1 Ultra Wideband

Ultra Wideband signals are commonly defined as signals that have a -10 dB bandwidth greater than 500 MHz or a fractional bandwidth of more than 0.2 (FCC §15.503, [5]). The fractional bandwidth is defined as B_s/f_c, where B_s is the signal bandwidth and f_c is the center frequency. The very large bandwidth leads to some very important benefits (cf. [6, 7]):

- Accurate ranging due to fine delay resolution
- Reduced fading due to finer multipath resolution leading to high robustness
- Superior obstacle penetration
- Resistance to jamming
- Possible high data rates
- Coexistence to narrowband systems, where UWB occurs to them only as additional noise
- Small form factor of transceivers

In general, high-rate and low-rate systems can be distinguished. The high-rate systems are mainly driven by the WiMedia Alliance and are standardized by ECMA-368 [8] and ECMA-369 [9]. The system is based on Multiband Orthogonal Frequency Division Multiplexing (MB-OFDM) and focus on high data rates (up to 480 Mbps) and short distances (<10 m). Applications are e.g. multimedia streaming or wireless universal serial bus (wireless USB). On the other hand, ultra high data-rates are not urgently necessary for localization systems but longer range is needed. High robustness and low complexity are more important here. This is achieved with IR-UWB, where ultra short pulses, in nano seconds [ns] range, are transmitted. Some authors relate IR UWB only to the transmission of UWB pulses in baseband according to the pioneering paper of [10]. Others distinguish between carrier-less IR and carrier-based IR-UWB [11]. Carrier-less IR implements pulse shaping according to a given spectral mask and allows for ultra-low-power transmitters by avoiding the mixer. However, such approaches are quite inflexible [11–13]. As flexibility is very important to satisfy the regulations

and the channel allocation of standards, this work only deals with carrier-based IR, which is shortly called IR in the rest of the work.

The very large bandwidth also makes the technology very challenging for researchers and developers. While transmitters can be implemented with low power consumption and low complexity, the receivers are quite challenging. Coherent receivers can exploit the absolute phase information of the carrier-modulated signal, while a non-coherent receiver can only exploit the magnitude of the signal [14]. Coherent receivers suffer from the huge bandwidth, as they have to apply Nyquist sampling, and they have to recover the carrier frequency. Non-coherent receivers are expected to relax the challenging requirements of UWB. The energy detector performs the down-convertion with a squaring and integration device. This makes the receiver independent of Nyquist sampling and a carrier recovery is not needed. On the other hand, the signal processing can only be done on the magnitude of the signal, thus the phase information is lost and a performance loss occurs. A detailed tutorial paper on non-coherent receivers is given by [14].

1.2 Standardization

Real Time Locating Systems (RTLS) and WSNs are currently a hot topic in research and industry. Therefore standardization activities are ongoing at the Institute for Electrical and Electronics Engineers (IEEE), GS1 EPCglobal, the International Standardization Organization (ISO), and International Electrotechnical Commission (IEC). ISO and IEC has issued a sequence of standards for RTLS under ISO/IEC 24730.

A wideband direct sequence spread spectrum (DSSS) system in the 2.4 GHz Industrial, Scientific and Medical (ISM) band is defined under ISO/IEC 24730-2 [15]. The system uses a bandwidth of 60 MHz and is designed for long range and low complexity. The system shows one-way communication, where the tag is transmitting at random times and the position is determined by time difference of arrival (TDoA). The mandatory data rate is quite low with 57.9 kbps. Products promise accuracies in many environments (industrial and outdoor) of better than 2 m and an operating distance for ranging of up to 1000 m outdoors [16].

ISO/IEC 24730-5 [17] also works in the 2.4 GHz ISM band. The communication scheme is based on Chirp Spread Spectrum (CSS), where a carrier is swept over 80 MHz. The communication scheme is bi-directional and allows for time-of-arrival (ToA) ranging. The system supports a data rate of up to 1 Mbps. Products promise a ranging accuracy of 2 m indoors and 1 m outdoors [18] and an operating distance of 180 m [19].

The IEEE 802.15.4a standard [20] focuses on ultra-low power consumption, low cost, and localization with accuracies better than 1 m. The standard has been issued in 2007 as an amendment to the IEEE 802.15.4 standard [21]. It defines an alternative physical (PHY) layer and an extended Medium Access Control (MAC) layer. The signalling scheme is (carrier-based) IR-UWB and supports one-way (TDoA) and two-way (ToA) ranging. The system typically operates within the Federal Communication Commission (FCC) UWB band, which is defined from 3.1 to 10.6 GHz. Its signals have a bandwidth between 500 and roughly 1355 MHz. Products promise an accuracy of 10 cm and an operating distance beyond 500 m [22]. A detailed description of the standard can be found in Chapter 2.

Standardization activities for RTLS are still ongoing. A revision of ISO/IEC 24730-2 is under development, which should improve the robustness, data-rate and avoids synchronization of the base

stations. The IEEE 802.15.4f Task Group currently develops a new standard for active RFID systems, which also enables high precision UWB localization from the tag to the base station and additionally defines an optional 2.4 GHz narrowband link from the reader to the tag. GS1 EPCglobal is currently evaluating specific air interface protocols (AIPs) for active tagging in the Hardware Action Group for active tagging (HAT) ad hoc committee, where localization and sensor capability is one of the key issues.

Other localization systems are available on the marked, but they do not implement a released standard, e.g. an UWB RTLS is presented in [23]. Others are based on standards that are not specifically designed for localization systems and so achieve only moderate accuracy, e.g. an WLAN based RTLS is shown in [24].

1.3 Motivation and Objectives

The final performance of an UWB positioning system depends on many parameters, such as parameters of the transmitted waveform, radio regulations, channel, receiver architectures, ranging-, positioning- and tracking algorithm, and finally the geometric setup. This summarizes the overall goal of this thesis, which is **the better understanding of low-complexity UWB localization systems**.

Standardization activities for UWB localization systems are still ongoing. Currently the only released low-data-rate and low-complexity UWB standard with high-accuracy localization is IEEE 802.15.4a. Some manufacturers are unsatisfied with the current IEEE 802.15.4a standard, as they believe that the standard is too complicated and allows for too many settings[1]. In principle everyone would like to have a low-cost and ultra-low-power system with highly accurate localization and high reliability. All of these requirements are tough too achieve, especially for the strict UWB regulations (see Section 2.2). Furthermore, the regulation process is not completed, as satisfying outdoor and unified global regulations are still missing. Thus the **analysis of the IEEE 802.15.4a standard and the current regulations** is necessary for further standardization and regulatory activities. The analysis should show the influence of system parameters on low-complexity localization systems. Chapter 2 gives a short overview on this topic and also discusses the UWB regulations.

As mentioned before, an important part for low-cost and low-power-consuming systems is the receiver. Thus the **energy detector** is studied in this thesis, which is given by

$$x[n] = \int_{nT_I}^{(n+1)T_I} (\tilde{r}(t) + \nu(t))^2 dt = \int_{nT_I}^{(n+1)T_I} \tilde{r}^2(t) + 2\tilde{r}(t)\nu(t) + \nu(t)^2 dt \tag{1.1}$$

where $\tilde{r}(t)$ is the received signal without noise, $\nu(t)$ is additive white Gaussian noise, and $x[n]$ is the output of the energy detector. The squaring causes quadratic noise and signal-by-noise cross terms, which harms the performance [14]. The channel causes inter-pulse-interference (IPI), which can not be completely canceled after the squaring via despreading even if the codes have perfect autocorrelation properties (see Chapter 4). The performance becomes strongly dependent on parameters of the AIP. Thus, the **influence of system parameters** on low complexity receiver architectures and the whole localization system has to be studied.

It is of crucial importance for realistic results, that the analysis is based on realistic channels from typical application environments. Therefore, the **demonstrator system** of [25] has been extended

[1] Please note, that this is not necessarily the opinion of the author.

to the IEEE 802.15.4a standard to perform ranging and communication experiments. The channels need to be analyzed and characterized for the simulation frameworks.

The energy detector shows a lack of performance due to non-coherent combining losses, squared noise terms and signal-by-noise crossterms. Thus **a comparison to high complexity coherent receivers** becomes important to show the trade-off between low complexity and high performance.

Often UWB has been indicated to reach only tens of meters. Thus an analysis is needed to show the **maximum operating distance** of low-complexity UWB localization systems.

Another goal is the implementation of a **positioning simulator** to evaluate the influence of specific system parameters on the overall system performance for localization.

Central research questions are defined as follows:

- What is the influence of the system parameters on the performance of energy detectors?
- What are the differences between low-complexity energy detectors and high-complexity coherent receivers?
- What are the operating distances of IEEE 802.15.4a based UWB localization systems?
- What is the localization capability in NLOS scenarios using the IEEE 802.15.4a standard?

1.4 Framework of the PhD Thesis

The thesis was performed in cooperation with CISC Semiconductor Design+Consulting GmbH, which exploits the created expertise in their standardization and development activities. The project was funded by the Austrian Federal Ministry for Transport, Innovation and Technology (BMVIT) and the Austrian Research Promotion Agency (FFG) in the framework of the Austrian research programme for Research, Innovation, Technology and Information Technology (FIT-IT) with project number 814560.

1.5 Outline and Scientific Contribution

This section shows the outline and the scientific contribution of this thesis.

1.5.1 Outline

Chapter 2 introduces the IEEE 802.15.4a standard with a special focus on its signal design and the defined ranging protocols. The UWB regulations for specific countries are discussed with respect to the standard. Chapter 3 presents the UWB demonstrator system, which is used for the experiments in indoor and outdoor environments. The demonstrator system was used for collecting and estimating the channel impulse responses for the subsequent chapters with a coherent receiver architecture. A large scale fading (LSF) channel model has been derived for the specific environments and is used for the simulation framework in Chapter 6. In Chapter 4, a statistical model for the low-complexity energy detector is introduced and the effects of inter pulse interference (IPI) are studied for the preamble symbols of the IEEE 802.15.4a standard. The maximum operating distance of the standard is evaluated in Chapter 5 for coherent and non-coherent receivers. For this purpose, a link budget is defined and the FCC/CEPT regulations are modeled. Chapter 6 presents a system-level simulator for

positioning and tracking (U-SPOT). The simulator is based on the results of the previous chapters. It combines the measurements, channel models, link budgets according to the FCC/CEPT regulations, and the receiver structures to form a statistically defined simulation framework. In this work, U-SPOT is used to show the influence of NLOS links on the localization performance of the IEEE 802.15.4a. Chapter 7 concludes the thesis.

1.5.2 Scientific Contribution

In the following a detailed overview of the scientific contribution is given:

Chapter 3: Experimental Characterization of UWB Channels

As mentioned before, the wireless channel is one of the most important parts for analysis and simulation of communication and positioning systems. Often specific situations and environments are interesting for such studies, e.g.: How is the performance of the positioning system in office NLOS situations? Thus, it is worthwhile to use real (measured) channels for further simulations and collect a data base of channels for the specific situations.

In this chapter, we present a modular UWB demonstrator platform for communication and ranging experiments. The system is based on an FPGA, which generates the base band pulse sequences according to IEEE 802.15.4a. High performance laboratory equipment is used for phase synchronous up-conversion and sampling. The received signals are stored by a digital storage oscilloscope for offline data processing. This keeps the system as flexible as possible and enables the creation of a database of the received signals. Finally, the demonstrator satisfies the FCC/CEPT regulations.

An extensive measurement campaign was performed in LOS and NLOS scenarios in outdoor, industrial, office, and residential environments. A coherent receiver architecture is presented, which is used for the estimation of the channel responses. The channel responses are later used for the simulations in Chapter 4 and 6. The channel estimation and the parameterization of the pathloss model are carried out and the major differences between the scenarios are pointed out. The channel models are used in Chapter 6 for the simulations with U-SPOT. Finally, the root mean square (RMS) delay spread is analyzed for the specific environments. It is shown that in LOS environments the pathloss exponent can be between 1.5 and 2, while in NLOS the value reaches up to 5 due to multiple wall penetrations. The RMS delay spread is also strongly environment dependent and achieves values up to 100 ns.

Chapter 4: Statistical Modeling of the Energy Detector

The IEEE 802.15.4a standard defines a large number of different system parameters for the preamble, which are analyzed in detail for energy detectors. The focus of this work is on statistical modeling of IPI, noise terms, and correlation properties of two despreading methods. One method shows perfect crosscorrelation properties and the other one shows a zero-mean noise floor. An IPI-intensive LOS industrial environment was chosen to verify the theoretical results and to evaluate both despreading methods for different system settings. It is shown that one method performs better if IPI is the limiting factor, while the other one is suitable if noise is dominant. It is shown that the system parameters have a significant impact on the performance of the energy detector.

Chapter 5: Maximum Operating Distance Estimation for IEEE 802.15.4a

In this chapter, the maximum operating distance is analyzed for ranging, using a coherent receiver and an energy detector under FCC/CEPT regulations. The analysis is based on the working points of the receivers and a link budget calculation. It takes into consideration the parameters of the preamble that influence the allowed FCC transmit power, and the free space losses. The best performance is achieved by using the code sequences with the longest pulse spacing, where coherent receivers can achieve a maximum operating distance up to several thousand meters and energy detectors up to several hundred meters. Finally, a complexity analysis compares the two receivers.

Chapter 6: UWB System-Level Simulator for Positioning and Tracking (U-SPOT)

Realistic simulation of UWB positioning and tracking is a tough and challenging task. Many parameters have a significant impact on the final performance of the positioning system, such as parameters of the transmitted waveform, radio regulations, channel, receiver, ranging-, positioning- and tracking-algorithm, and finally the geometric setup. A realistic simulation framework is needed to develop and optimize UWB methods and algorithms. This chapter proposes a novel framework for realistic UWB positioning simulations. While ray-tracing simulators focus on a given user-defined scenario, our approach uses statistically defined environments. Random processes are used to select channel impulse responses from the measurement database created in Chapter 3, according to an algorithm that introduces realistic large and small-scale variability with space. In particular, LOS and NLOS channels are used at a defined ratio.

In this work the application of the simulation framework is used to compare the performance of a least-squares (LS) positioning algorithm to a standard and an extended Kalman filter (SKF and EKF) tracking algorithm in environments with a large fration of NLOS links. Furthermore, the IEEE 802.15.4a standard is analyzed with respect to its positioning performance. It is shown that the localization accuracy and reliability can be improved significantly with the tracking algorithms, but their performance drops significantly with increasing probability of NLOS links.

1.5.3 List of Author's Publication

The thesis is partly based on previously published work, which is listed in Tables 1.1 and 1.2. The relation of the papers to the specific chapters is indicated and classified into major and minor relations. The author has cooperated during his work with partners from CISC Semiconductor GmbH (Austria), ETH Zurich (Switzerland), Vienna University of Technology (Austria), NXP Semiconductors (Austria), and Delft University of Technology (The Netherlands).

Table 1.1 Relation of the author's publications to the chapters of this thesis.
●: major relation; ○: minor relation

	Chapter			
Publication	3	4	5	6
T. Gigl, F. Troesch, J. Preishuber-Pfluegl, and K. Witrisal "Ranging Performance in IEEE 802.15.4a for Coherent and Non-Coherent Receivers" IEEE Transactions on Microwave Theory Techniques, MTT, 2011 (submitted)			●	○
B. Geiger, T. Gigl, and K. Witrisal "Enhanced-Accuracy Channel Estimation and Ranging for IR-UWB Energy Detectors" Ultra-Wideband, ICUWB 2010, IEEE International Conference on		○		
T. Gigl, F. Troesch, J. Preishuber-Pfluegl, and K. Witrisal "Maximal Operating Distance Estimation using IEEE 802.15.4a Ultra Wideband" Positioning, Navigation and Communication, WPNC 2010, 7th Int. Workshop on			●	○
T. Gigl, F. Troesch, J. Preishuber-Pfluegl, and K. Witrisal "Maximal Operating Distance Estimation using IEEE 802.15.4a Ultra Wideband" Impact on Ubiquitous IT Co-Design to Industry, KOALA 2010, Int. Conference on			●	○
T. Gigl, P. Meissner, J. Preishuber-Pfluegl, and K. Witrisal "Ultra-Wideband System-Level Simulator for Positioning and Tracking (U-SPOT)" Indoor Positioning and Indoor Navigation, IPIN 2010, Int. Conference on				●
P. Meissner, T. Gigl, and K. Witrisal "UWB Sequential Monte Carlo Positioning using Virtual Anchors" Indoor Positioning and Indoor Navigation, IPIN 2010, Int. Conference on				○
A. Adalan, T. Gigl, M. Fischer, and K. Witrisal "A Modular Impulse Radio Ultra-Wideband Research & Development Platform for IEEE 802.15.4a" Wireless Technology Conference, 2009. EuWIT 2009. European	○			
T. Gigl, J. Preishuber-Pfluegl, D. Arnitz, and K. Witrisal "Experimental Characterization of Ranging in IEEE 802.15.4a using a Coherent Reference Receiver" Personal, Indoor and Mobile Radio Communications, PIMRC 2009, IEEE 20th Int. Symposium on	●		○	○
B. Geiger, T. Gigl, J. Preishuber-Pfluegl, K. Witrisal "Experimental Characterization of System Parameters for Ranging in IEEE 802.15.4a using Energy Detector" Radioengineering, Vol. 18, Nr. 3, 2009		○		
T. Gigl, T. Buchgraber, B. Geiger, A. Adalan, J. Preishuber-Pfluegl, and K. Witrisal "Pathloss and Delay-Spread Analysis of Multipath Intensive Environments using IEEE 802.15.4a UWB Signals" COST 2100 Management Committee Meeting, Vienna 2009	●			○
T. Gigl, J. Preishuber-Pfluegl, and K. Witrisal "Statistical Analysis of a UWB Energy Detector for Ranging in IEEE 802.15.4a" Ultra-Wideband, ICUWB 2009, IEEE International Conference on		●	○	○

Table 1.2 Relation of the author's publications to the chapters of this thesis. (continued)

●: major relation; ○: minor relation

	Chapter			
Publication	3	4	5	6
A. Adalan, M. Fischer, T. Gigl, K. Witrisal, A.L. Scholtz, C.F. Mecklenbräuker "Ultra-Wideband Radio Pulse Shaping Filter Design for IEEE 802.15.4a Transmitter" Wireless Communications and Networking Conference, WCNC 2009, IEEE	○			
T. Gigl, T. Buchgraber, A. Adalan, J. Preishuber-Pfluegl, M. Fischer, and K. Witrisal "UWB Channel Characterization using IEEE 802.15.4a Demonstrator System" Ultra-Wideband, ICUWB 2009, IEEE International Conference on	●			
D. Arnitz, U. Mühlmann, T. Gigl, and K. Witrisal "Wideband System-Level Simulator for Passive UHF RFID" RFID, RFID 2009, IEEE Int. Conference on				○
T. Gigl, G. Janssen, V. Dizdarevic, K. Witrisal, Z. Irahhauten, "Analysis of a UWB Indoor Positioning System Based on Received Signal Strength" Positioning, Navigation and Communication, WPNC 2007, 4th Int. Workshop on				○
Supervised Master Thesis				
B. Till "IEEE 802.15.4a-UWB compliant Positioning using Energy Detectors" Master Thesis, Graz University of Technology, 2010	○			
B. Geiger "Enhanced Accuracy Channel Estimation and Ranging for Energy Detectors" Diploma Thesis, Graz University of Technology, 2009		○		
T. Buchgraber "Experimental Evaluation of the IEEE 802.15.4a Standard" Diploma Thesis, Graz University of Technology, 2008	●			

2

An Overview of IEEE 802.15.4a and UWB Regulations

One of the central points of this thesis is the analysis of the IEEE 802.15.4a standard with respect to the defined system parameters and their influence on the ranging and localization performance. This section gives an overview of the structure of the 4a-signals and illustrates the defined ranging mechanisms. Finally, the UWB regulations are discussed and they are compare to the signal design of the standard.

2.1 IEEE 802.15.4a Standard

The IEEE 802.15.4 [21] standard defines the Physical (PHY) and the Medium Access Control (MAC) layer for low-rate wireless personal area networks (WPAN) focusing on low power, low data rate, and low-complexity short-range devices. IEEE 802.15.4a is an amendment to IEEE 802.15.4 [21] adding high precision ranging / localization capability with 1 meter accuracy and better, high aggregate throughput, scalability w.r.t. data rates, longer range, lower power consumption and lower cost [26].

The standard defines a UWB and a Chirp Spread Spectrum (CSS) PHY Layer, where the CSS modulation scheme is intended only for robust communication and the UWB PHY additionally allows for high accuracy ranging. This work deals only with the UWB PHY of the standard. The standard defines 16 frequency channels in three bands, namely, the Sub-Gigahertz Band (<1 GHz), the Low-Band (3.3 to 4.8 GHz), and the High-Band (5.9 to 10.3 GHz), cf. Figure 2.4. The channels have a bandwidth between 500 MHz and 1.35 GHz, which allows for very accurate ranging and positioning, because a larger bandwidth leads to better accuracy [27].

IEEE 802.15.4 distinguishes between full functional devices (FFD) for high performance and high-complexity devices, where the power consumption is not the major restriction, and reduced functional devices (RFD) for low-complexity and low-cost. The 4a-standard allows for both types. Binary Phase Shift Keying (BPSK) and Burst Position Modulation (BPM) are defined for FFD using coherent processing, while only BPM is used for RFD using non-coherent processing. A burst is a randomly coded sequence of pulses, which is transmitted per bit and is used to increase the Signal-to-Noise Ratio (SNR). Data rates are defined from 110 kbps (for long range links) up to 27 Mbps (for high throughput). The nominal data rate is 850 kbps.

Figure 2.1 shows the general package structure. The synchronization header (SHR) preamble consists of the preamble and the start-of-frame delimiter (SFD). The preamble is used for signal detection,

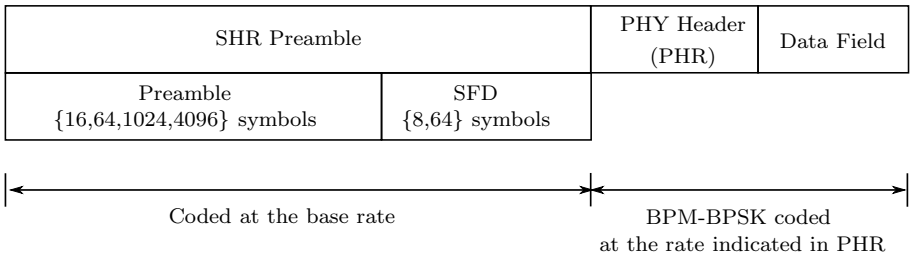

Figure 2.1 Illustration of the IEEE 802.15.4a package structure [28].

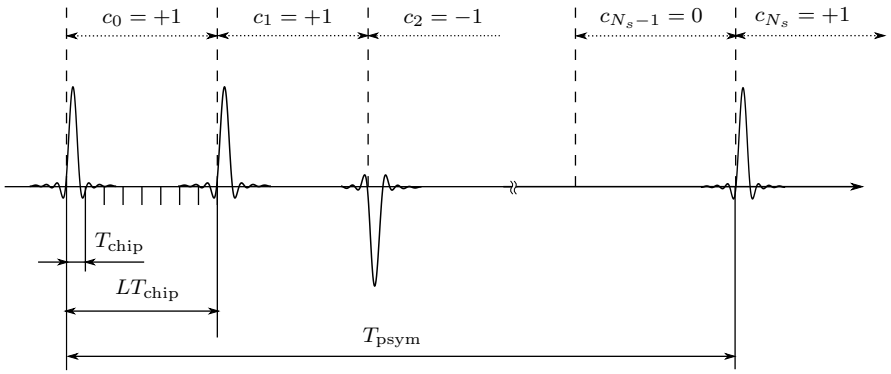

Figure 2.2 IEEE 802.15.4a preamble symbol

channel estimation, synchronization, and ranging. The SFD is necessary for establishing the frame timing, and its detection is important for accurate counting of the turn-around time (see below) and to evaluate the figure-of-merit (FoM) (see [28] and [20]). The PHR contains information necessary for successful decoding of the data.

This work focuses on ranging and localization, where the most important part of the standard is the SHR. An example preamble sequence is shown in Figure 2.2. The preamble consists of ternary code sequences of length $N_s = 31$ or $N_s = 127$, where the code elements are $c_i \in \{-1, 0, +1\}$. One code element is spaced by L chip elements with duration $T_{\text{chip}} = 2$ ns. In the standard L is called spreading factor, which implies a spacing of the pulses. Usually spreading in communication engineering means to spread the signal in frequency domain. In the rest of the work the meaning of spreading is chosen according to the standard. A spread ternary code sequence is called a preamble symbol and the duration of the preamble symbol is given by T_{psym}. The preamble symbols are repeated up to 4096 times with a specific symbol repetition rate (base rate). The preamble shows perfect circular autocorrelation properties for coherent and non-coherent receivers.

Figure 2.3 shows the ranging protocols defined by the standard. The recommendation of the standard is to implement two-way ranging with ToA estimation (TW-ToA). First ranging device (*RDEV*) *A* initializes the ranging with D_2 and *RDEV B* responds with A_2. The round trip time is measured by *RDEV A* and consists of the signal travel time T_t, the turn around time T_{ta}^B from *RDEV B* and the return travel time (again T_t). Next, a time-stamp report D_4 is transmitted that contains the reception time of D_2 and the transmission time of A_2, some characterization of the crystal, and the FoM for the quality of the arrival time estimation. The accuracy can be improved by the optional

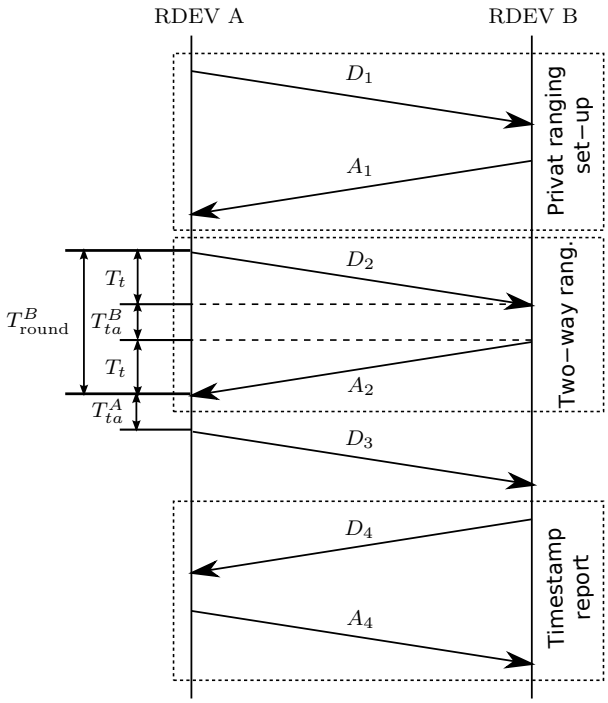

Figure 2.3 Illustration of the ranging protocols supported by the IEEE 802.15.4a [28].

symmetric double sided (SDS) TW-ToA protocol mode, where also *RDEV B* measures the round trip time between A_2 and D_3. Some applications require to protect the location of the mobiles, for these an optional private ranging mode is defined, where an authentication phase has to be performed first with the range authentication packet (RAP) D_1 and A_1 (optional). The RAP contains some encrypted data about used code sequences of both devices. If *RDEV B* finds *RDEV A* authentic, the ranging process starts as described before. An encrypted time stamp report additionally increases the security level. Further information about the ranging in IEEE 802.15.4a can be found in [28].

As the radio spectrum is very scarce, the propagation of UWB has to be regulated very strictly by the local public authorities. This ensures that UWB systems do not harm or impair others.

2.2 UWB Regulations

Many countries have their own regulations, which make global standardization activities and system implementation rather difficult. Furthermore, the usage of a fixed infrastructure is widely prohibited outdoors, which is a big hurdle for the application area and the market penetration of UWB systems.

USA

The first UWB regulations have been issued by the FCC in 2002 and revised in 2004 [5]. These regulations show the most relaxed conditions for UWB, allowing the transmission of UWB signals from 3.1 to 10.6 GHz in indoor environments (§15.517). An average power limit and a peak power limit are defined in terms of power spectral density (PSD) and the equivalent isotropically radiated

power (EIRP). The maximum average PSD is limited to -41.3 dBm/MHz by averaging over 1 ms (§15.521) and the maximum peak PSD limit is defined at 0 dBm/50 MHz. The transmission of UWB below 960 MHz is also allowed at -41.3 dBm/MHz (see [29]).

Europe

In Europe a signal with a bandwidth greater than 50 MHz is defined as a UWB signal [30]. This is a significant order below the common definition. In the rest of the work UWB is defined according to the FCC definition. The limits are defined according to the FCC regulations, but with some additional restrictions. The usage of UWB devices from 3.1-4.8 GHz is allowed when applying low duty cycle (LDC) or detect and avoid (DAA) mitigation techniques. The LDC mode stipulates additionally that the transmitted signal is only allowed to occupy 5% each second and 0.5% of each hour. Furthermore, it is not allowed to exceed 5 ms per signal[1]. The band from 6 to 8.5 GHz is usable without any mitigation technique and from 8.5 to 9 GHz again DAA has to be applied [31].

Asia

The Asian countries have regulations similar to the European. Japan allows the use of UWB from 3.4 to 4.8 GHz using DAA and 7.25 to 10.25 GHz without. In contrast to any other country, a minimum data rate of 50 Mbps is necessary for transmission. Thus, low data rate systems such as IEEE 802.15.4a ($\leq$ 27 Mbps) are currently not allowed. Korea defines the UWB-Bands from 3.1 to 4.8 GHz using DAA and 7.2 to 10.2 GHz. Singapore allows the usage from 3.4 to 4.8 GHz with appropriate mitigation techniques and 6 to 9 GHz without. A good overview of current regulations is given in [32].

Comparison of the regulations with the IEEE 802.15.4a channel map

Figure 2.4 shows an overview of the channels defined in IEEE 802.15.4a and their usage in the specific countries. Although 4a does not fulfill the data rate limit of Japan, the spectral mask is shown in the figure for completeness. The regulations for the USA support all channels of the IEEE 802.15.4a standard, whereas in other countries only a subset is permitted. The Low-Band is nearly everywhere allowed. Only Channel 1 and 4 are not fully included in the spectral masks of Japan and Singapore. Europe and Singapore allow the usage of the lower frequency channels of the High-Band, where Channel 7 with a bandwidth of approx. 1.1 GHz and a carrier frequency of 6.5 GHz is not fully included in the spectral masks. Korea and Japan only allow the use of the high-frequency channels, where also two large bandwidth channels are fully included. The mandatory channel of the Low- and the High-Band are allowed in every country. The Sub-Giga-Hertz channel is allowed in the USA only [1] [2].

[1] Therefore, 4a-signals with the longest preamble symbols are not allowed.
[2] Note, this information is not available for Korea and Singapure.

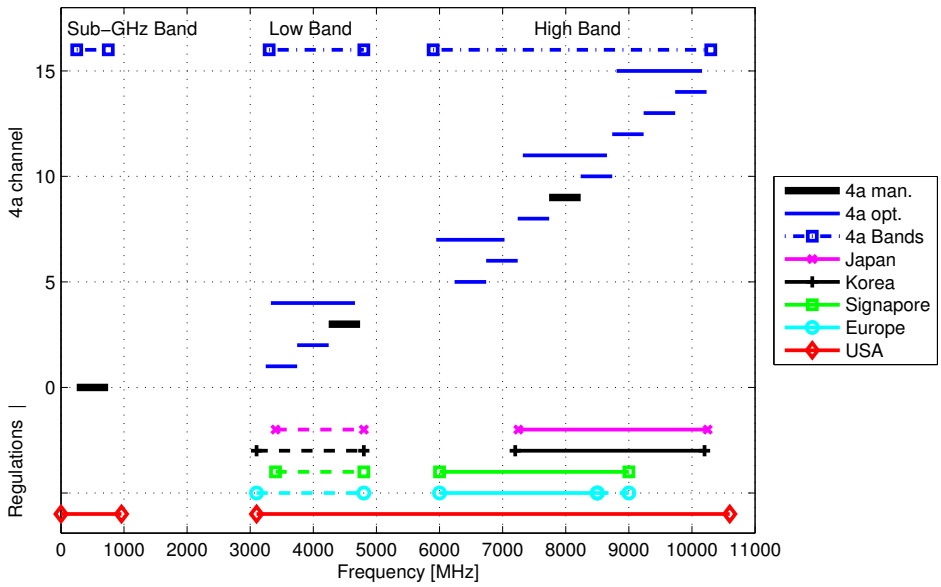

Figure 2.4 Overview of UWB regulations and the IEEE 802.15.4a channels, where *4a man* are the mandatory IEEE 802.15.4a channels and *4a opt.* indicates the optional channels. The dashed lines indicate bands where mitigation techniques has to be applied.

3

Experimental Characterization of UWB Channels

As already mentionend in the previous section, the IEEE 802.15.4a standard [20] was designed to support low-cost and low-complexity hardware and software for mobile devices. Nevertheless the development of hardware and software for UWB systems is very challenging, emphasizing the need for testbeds and demonstrator systems for development and evaluation.

In this section, a UWB demonstrator system for transmitting and receiving IEEE 802.15.4a compliant signals is presented. The experimental setup is used for performing measurements in indoor and outdoor environments. Channel estimation and the parameterization of a pathloss model have been carried out in these environments. Finally, the RMS delay spread and the major differences between the scenarios are pointed out. The channel impulse responses of the measurement campain and the channel models are used in the subsequent chapters and are a central part of the simulation framework of Chapter 6.

In literature we can find several IR-UWB testbeds and platforms for research and development [13, 33–37]. Most of the reported systems are highly integrated testbeds thus only software can be evaluated by using these platforms. The systems of [34, 36] are based on the generation of Gaussian monocycles, which is not a good choice for testbeds and evaluation systems as this method is quite inflexible [33]. This is given by the fact, that the pulses are not easy to generate. An up-conversion and baseband pulse shaping is an easy and flexible alternative. Furthermore Gaussian monocycles cannot achieve the pulse requirements of the IEEE 802.15.4a standard [13]. Thus, [13, 33] and our system are based on an up-conversion by oscillators. The flexibility can also be increased using digital signal processors (DSP) or general purpose processors (GPP) for the receiving algorithms[13, 35].

In contrast to the other test systems, our approach implements both, a highly flexible hardware and software solution for various kinds of applications of IR-UWB. We propose a modular UWB demonstrator for low range low data rate applications where each module is substitutable for unit testing and verification of the hardware itself, or the software. As the demonstrator system uses very high quality hardware components, it can be used as a reference system to evaluate other more integrated testbeds [38]. Furthermore, the demonstrator system can be used for performance analysis of the IEEE 802.15.4a standard with respect to communications and ranging. This is highly necessary

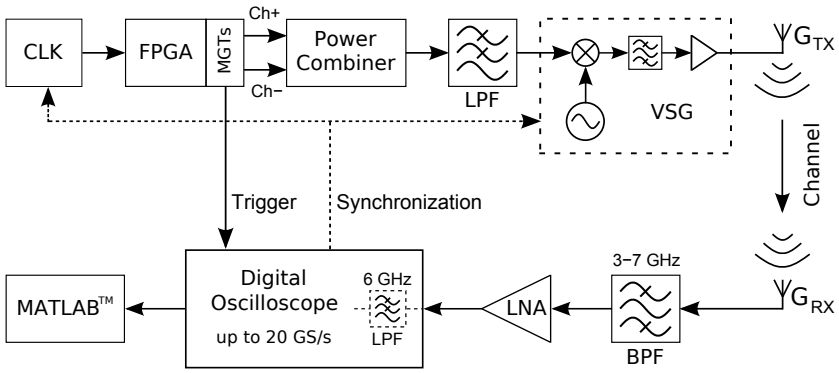

Figure 3.1 Modular concept of the demonstrator system ([39], © [2009] IEEE)

because the standard defines a large number of user-assignable parameters. The optimal parameters often depend on environmental conditions as well. Hence, the demonstrator is used in this chapter to parameterize the pathloss model and the log-normal large scale fading (LSF) from specific indoor and outdoor LOS and NLOS environments.

The high performance laboratory equipment makes our system quite bulky, thus an extension has been implemented which substitutes these very expensive devices by more integrated self-made RF devices. The principle structure is nearly unchanged and the modular concept is kept for high flexibility. A comparison between the two systems can be found in [38].

The rest of this chapter is organized as follows: In the next section we describe the hardware and signal generation principle of the UWB Demonstrator System. In Section 3.2, we present the software receiver architecture followed by the mathematical description of the channel estimation in Section 3.3. In Section 3.4 it is shown, that the inter pulse interference can be canceled perfectly for coherent receivers. Then, in Section 3.5, we verify the demonstrator system in an LOS outdoor, an LOS/NLOS industrial, an LOS and two NLOS office, and a residential environment. The parameters of the pathloss model and the root mean square delay spread are determined. Finally, in Section 3.6, we sum up our results and conclude.

3.1 UWB Demonstrator System

In this section we describe the practical implementation of the modular UWB demonstrator system. Figure 3.1 illustrates the necessary parts for the unidirectional signal transmission scheme, starting from pulse generation up to signal reception and evaluation.

The core element for UWB pulse generation is a Field Programmable Gate Array (FPGA), which is programmed according to the UWB PHY specification of the IEEE 802.15.4a standard. The FPGA is externally clocked by a clock-generator (CLK), which is used to force the FPGA to the desired peak pulse repetition frequency (PRF). The FPGA has high-speed serial Input/Outputs (I/Os) which are called Multi-Gigabit Transceivers (MGTs). Two of them are used for creating the UWB pulses [40]. One stream implements the positive (Ch+) and the other one the negative pulse sequences (Ch-) of the ternary data. To combine the two separate channels into a single one with positive and

negative pulses, a passive power combiner circuit is used. Since the pulse shape at the output of the power combiner is not compliant with the IEEE 802.15.4a standard, additional pulse shaping has to be implemented. In the time domain, the standard restricts the magnitude of the cross-correlation function of the generated pulse and a pre-defined Root Raised Cosine (RRC) reference pulse. In the frequency domain, it must be checked if the passband signal fits into a given spectral mask. In our case, pulse shaping is done in baseband with an optimized 5^{th} order Bessel lowpass filter [41].

After pulse shaping, the baseband signal is up-converted to a carrier frequency by a vector signal generator (VSG). The output gain of the VSG is adjusted to comply with the allowed power spectral density at the antenna. The emitted signal from the transmit antenna (G_{TX}) propagates through the radio channel and is received by another UWB antenna (G_{RX}).

The received signal is bandpass filtered from 3 to 7 GHz to reduce unwanted noise from other frequency bands and to protect the low noise amplifier (LNA) from strong interferers like the Global System for Mobile communications (GSM) and WLAN. The LNA amplifies the filtered input signal for a digital oscilloscope (DSO) that is capable of sampling the received UWB signals directly in passband. This concept offers the possibility to simulate different receiver structures or analyze the data in software. Under-sampling is also possible in this constellation and allows to obtain longer sampling sequences due to the limited memory size of the oscilloscope. Offline processing of the signals enables flexible choices of software receiver architectures and channel estimation algorithms. Since the sampled data must be stored in the oscilloscope's memory before being available for analysis, real-time applications are not possible in the current setup. An extension of this demonstrator to a pseudo-real time positioning system has been developed within an MSc project [42]. This positioning system is presented in Appendix A and the current hardware configuration of the demonstrator is shown in Appendix B.

We use an extra MGT output of the FPGA to provide a trigger pulse for the oscilloscope on start of each UWB packet transmission. This trigger provides a time reference for sampling the received signal. Furthermore, it can be used as a rigid reference for ToA ranging experiments.

Optionally, the measurement equipment allows external synchronization by a 10 MHz reference signal, which has been used to lock the external clock generator with the up-converter and the sampling oscilloscope. This locks the PRF to the carrier frequency, and thus generates phase synchronous up-converted pulses. Furthermore if the DSO is synchronized to these devices, phase synchronous sampling is applied. However, the measurement equipment is usually not flexible enough to use multiples of the PRF of 499.2 MHz as sampling frequency. Thus, the PRF is set to 500 MHz and the carrier frequency f_c and the sampling frequency $1/T$ is set to multiples of it. This slight change is negligible for research on the properties of the standard. Without coherent sampling the system is still usable at the original frequencies.

In Figure 3.2 we can see two different views on the same baseband example sequence. Figure 3.2(a) shows a UWB packet consisting of synchronization header (SHR) preamble, physical header (PHR) and the data field. Figure 3.2(b) presents a closer look at the start of the preamble sequence with Code 6. This code is defined as `[++00+00---+-0++-000+0+0-+0+0000]`, where + and - represent positive and negative pulses respectively and `0` means that no pulse is generated in the corresponding time-slot.

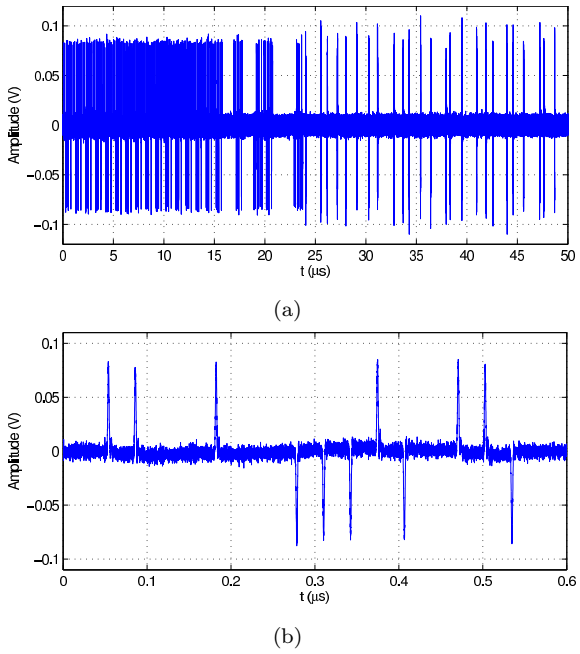

Figure 3.2 Example of a UWB baseband signal, (a): A UWB packet in baseband; (b): Preamble in baseband (Code 6) ([39], © [2009] IEEE)

3.2 Synchronized Coherent Receiver

As mentioned before, synchronization can easily be achieved in the experimental setup. Thus, a synchronized coherent receiver as shown in Figure 3.3 can be used to perform channel measurements. The analog part of the receiver containing the UWB antenna, amplifier, and sampling device with sampling frequency $1/T$ has been described in the previous section. The digitized received signal is filtered by a Hilbert filter to cancel the negative parts of the signal spectrum. Next, the signal is down-converted to baseband with an estimated carrier frequency. The estimation of the carrier frequency is not necessary in the synchronized setup. A lowpass filter (LPF) reduces the out-of-band noise in the input signal. Next, the signal is divided into a channel estimation path (upper signal path) and a communication path (lower signal path). The receiver is assumed to be synchronized, thus a code frame separation is applied in the Synchronized Separation (SySe) block (see Section 3.3). The channel estimation is performed in the preamble. Code despreading is performed to exploit processing gain and to cancel inter-pulse-interference, where c_i are the preamble code elements. Finally, the channel estimation is done by averaging over the received despread code frames (avg).

The channel response can be used as a matched filter (MF) for communications, which is shown in the lower part of the receiver. After code despreading the signal is downsampled to the symbol rate for the data signal, where $\mathring{c}$ is the communication symbol despreading code. The statistical analysis of this receiver architecture for ranging in IEEE 802.15.4a can be found in [43] and a similar coherent receiver architecture is analyzed in Section C.

The next chapter shows the signal model for the channel estimation.

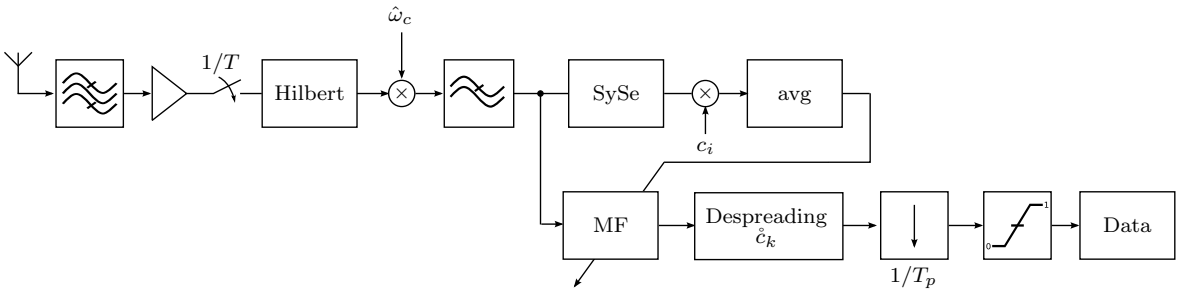

Figure 3.3 Synchronized Coherent Receiver (cf. [43], © [2009] IEEE)

3.3 Signal Model for Channel Estimation

The following notations are used: Column vectors and matrices are denoted by lower and upper-case boldface symbols, respectively. Estimated values are marked by hats.

As mentioned in Section 2.1 above, the channel estimation is performed on the preamble, thus this section introduces a signal model of the preamble. The IEEE 802.15.4a preamble code sequence $\mathbf{c}_s$ has a length N_s of 31 or 127 [20] and it consists of ternary elements $\in \{-1, 0, 1\}$. The spread preamble code vector $\mathbf{c}_{sp}$ is created as

$$\mathbf{c}_{sp} = \mathbf{1}_{N_{\text{sync}}} \otimes \mathbf{c}_s \otimes \boldsymbol{\delta}_L = \mathbf{c} \otimes \boldsymbol{\delta}_L \tag{3.1}$$

where $\otimes$ denotes the Kronecker product, $\boldsymbol{\delta}_L$ is a unit vector with a one at the first position and length L to extend the spacing between the preamble chips, and $\mathbf{1}_{N_{\text{sync}}}$ denotes a vector of ones to repeat the preamble sequence N_{sync} times. The vector $\mathbf{c}$ results from the periodically repeated preamble symbols. The transmitted signal $s(t)$ is defined as

$$\begin{aligned} s(t) =& \Re\left\{ \sqrt{E_p} \sum_{m=0}^{M-1} c_m w(t - mLT_{\text{chip}}) e^{j\omega_c t} \right\} \\ =& \sqrt{E_p} \sum_{m=0}^{M-1} c_m \tilde{w}(t - mLT_{\text{chip}}) \end{aligned} \tag{3.2}$$

where E_p is the energy per pulse, c_m represents the m-th element of $\mathbf{c}$, $w(t)$ stands for the energy normalized pulse shape, M is the number of code elements in the preamble, ω_c represents the carrier frequency, T_{chip} stands for the chip duration, and $\tilde{w}(t)$ is the up-converted pulse assuming the carrier and the pulse are phase synchronous.

Table 3.1 shows the timing characteristics of the preamble, where T_{synch} is the total duration of the preamble, *MRF* is the mean pulse repetition frequency, and $N_{1\text{ms}}$ is the number of preamble sequences within 1 ms. *ERF* is the effective pulse repetition frequency according to the regulations (see Section 5.2).

The transmitted signal (3.2) is sent over a multipath channel with channel impulse response $h_c(t)$, where also the effects of the antenna are contained for simplicity. Furthermore, $h_c(t)$ is assumed to be constant during T_{synch}. Thus, the analog received signal is

$$r_a(t) = s(t) * h_c(t) + \nu(t) \tag{3.3}$$

where $\nu(t)$ is modeled as additive white Gaussian noise and $*$ is the convolution.

Table 3.1 Preamble characteristic

N_s	L	N_{synch}	T_{chip} [ns]	T_{synch} [μs]	PRF [MHz]	MRF [MHz]	ERF [MHz]	$N_{1\text{ms}}$
31	16	16	2.0032	15.897	31.2	16.1	**0.256**	1006
31	16	64	2.0032	63.590	31.2	16.1	1.024	1006
31	16	256	2.0032	254.358	31.2	16.1	4.096	1006
31	16	1024	2.0032	**1017.436**	31.2	16.1	16.1	1006
31	16	4096	2.0032	**4069.744**	31.2	16.1	16.1	1006
31	64	16	2.0032	63.590	7.8	4.03	**0.256**	251
31	64	64	2.0032	254.359	7.8	4.03	1.024	251
31	64	256	2.0032	**1017.433**	7.8	4.03	4.03	251
31	64	1024	2.0032	**4069.744**	7.8	4.03	4.03	251
31	64	4096	2.0032	**16278.974**	7.8	4.03	4.03	251
127	4	16	2.0032	16.282	124.8	62.89	1.024	982
127	4	64	2.0032	65.128	124.8	62.89	4.096	982
127	4	256	2.0032	260.512	124.8	62.89	16.384	982
127	4	1024	2.0032	**1042.051**	124.8	62.89	62.89	982
127	4	4096	2.0032	**4168.205**	124.8	62.89	62.89	982

The analog input signal is sampled by $1/T$, thus the discrete time signal is defined by $r_a[n]{=}r_a(nT)$. Next, the negative frequencies are canceled by a Hilbert filter $h_{\text{hilb}}[n]$ and the complex baseband signal is obtained by down-converting the signal with the estimated carrier frequency $\hat{\omega}_c$. The digital baseband signal $r[n]$ is defined as

$$\begin{aligned} r[n] &= \left\{ (r_a[n] * h_{\text{hilb}}[n])\, e^{-j\hat{\omega}_c nT} \right\} * h_{\text{LP}}[n] \\ &= \sum_{m=0}^{M-1} c_m h(nT - mT_c) e^{j[\omega_c - \hat{\omega}_c]nT} + \nu_{\text{LP}}[n] \end{aligned} \tag{3.4}$$

where $h(t)$ is an equivalent channel response incorporating the pulse $w(t)$, the channel $h_c(t)$, the lowpass filter $h_{\text{LP}}[n]$, and the carrier phase offset. The filter $h_{\text{LP}}[n]$ is implemented to reduce the noise energy in the received signal. The noise signal $\nu_{\text{LP}}[n]$ is band limited $\nu_{\text{LP}}[n]{=}\nu[n] * h_{\text{LP}}[n]$, where $\nu[n]$ is assumed to be white Gaussian with variance σ_n^2, because of the much smaller bandwidth of $h_{\text{LP}}[n]$ in comparison to the frontend filter. Assuming the carrier frequency is perfectly known, (3.4) simplifies to

$$r[n] = \sum_{m=0}^{M-1} c_m h[n - mLN_{\text{chip}}] + \nu_{\text{LP}}[n] \tag{3.5}$$

where $h[n]{=}h(nT)$. The number of samples within a chip is defined by N_{chip}. Due to synchronization the code frames can be separated by the following method: A matrix $\mathbf{R}$ with dimensions $N_{\hat{h}} \times M$ is defined. $N_{\hat{h}}$ is the length of the matched filter and should be chosen such that the maximum excess delay of the channel is included. Note that inter-pulse-interference (IPI) can occur, i.e. $N_{\hat{h}}$ can be greater than N_c. $\mathbf{R}$ is filled by $\mathbf{R}_{a,b}{=}r[a + bN_c]$, in which the channel impulse responses will partly overlap in the columns, if $N_{\hat{h}}{>}N_c$. This is shown in Figure 3.4(a), where the normalized magnitude of the matrix $\tilde{\mathbf{R}}^T$ is shown. The matrix $\tilde{\mathbf{R}}^T$ is $\mathbf{R}^T$, where the m-th row is multiplied with c_m and the zero coded rows are canceled. The synchronized pulses are observable at 2 ns, with a magnitude that

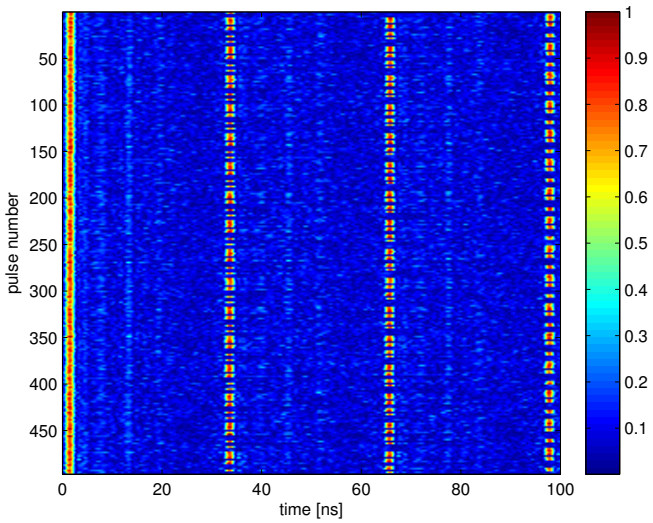

(a)

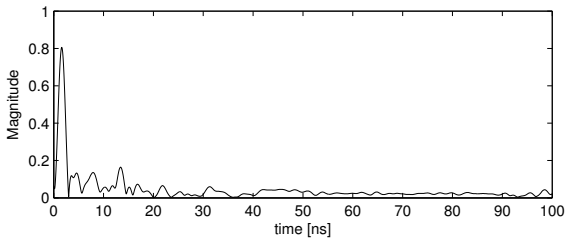

(b)

Figure 3.4 Synchronized despreading: (a) Matrix $\tilde{\mathbf{R}}^T$, (b) the estimated channel impulse response $\hat{h}[n]$ is obtained after averaging the rows.

is nearly constant. Every LT_{chip} (32 ns), a pulse sequence is transmitted. Thus at 34 and 66 ns the next pulses occur, encoded with the next code elements. Several multipath components are observable up to 20 ns. Due to averaging over the pulse repetitions (see Figure 3.4(b)), in other words averaging over the columns of $\tilde{\mathbf{R}}^T$, the differently coded pulses cancel out and the channel impulse response is estimated. This is due to the fact that the preamble code has perfect circular autocorrelation properties [44], thus IPI cancels for coherent receivers and the observed multipath components are well reconstructed. In other words, channel impulse responses with a longer maximal excess delay than the pulse repetition frequency (PRF) can be estimated. The mathematical proof of the IPI cancellation for coherent receivers is given in Section 3.4. The despreading and the estimation of the channel impulse response can be written in matrix notation by

$$\hat{\mathbf{h}} = \frac{\mathbf{R}\,\mathbf{c}}{M_1} \quad . \tag{3.6}$$

The numerator expresses the despreading operation, while M_1 is used to normalize the result. Only the non-zero elements of $\mathbf{c}$ contribute to this equation, thus the number of non-zero coded pulses is taken into account, hence $M_1{=}(N_s+1)N_{\text{sync}}/2$.

3.4 Analysis of Inter Pulse Interference Cancellation for Coherent Receivers

The noise term is not needed to show the effect of IPI cancellation, thus $\nu(t)$ is neglected. Assuming perfect circular autocorrelation properties of the code, the autocorrelation c_{auto} is given by

$$c_{\text{auto}}[\Delta] = \sum_{n=0}^{N_s-1} c_s[n]c_s[(n-\Delta) \bmod N_s] = \begin{cases} 1 & \text{for } \Delta = kN_s \\ 0 & \text{else} \end{cases} \tag{3.7}$$

for $k \in \mathbb{Z}$ and mod is the modulo operator. Equation (3.6) can be rewritten as

$$\hat{h}[n] = \frac{1}{M_1} \sum_{m=0}^{M-1} \sum_{\Delta=0}^{N_s-1} c[m]c[m+\Delta]\, h[n+\Delta L N_{\text{chip}}]. \tag{3.8}$$

To obtain the perfect autocorrelation properties, we assume $0 \le \Delta \le N_s - 1$, which allows the IPI-free estimation of the channel response with a maximal access delay $\tau_{\max} < N_s L T_{\text{chip}} = T_{\text{psym}}$. T_{psym} is the preamble symbol duration. This allows for the coding of the 4a standard a $\tau_{\max}$ of up to 4 μs . It follows with (3.7)

$$\begin{aligned} \hat{h}[n] &= \frac{1}{M_1} \sum_{m=0}^{M-1} c^2[m]h[n] \\ &= \frac{1}{M_1} \sum_{m=0}^{M_1-1} h[n] \\ &= h[n] \end{aligned} \tag{3.9}$$

due to $\sum_{m=0}^{M-1} c^2[m] = M_1$. It follows that the channel impulse response can be reconstructed perfectly.

Table 3.2 Signal parameters of the IEEE 802.15.4a standard

$Ch_{\#}$	f_c [MHz]	B_s [MHz]	N_s	$C_{\#}$	N_{sync}	L
3	4.5	500	31	6	1024	16

3.5 UWB Channel Modeling

This section shows experimental results for the demonstrator system. Channel measurements have been performed in six LOS and NLOS environments. The analysis of the measurements includes the parameterization of the pathloss model and the calculation of the root mean square delay spread (τ_{RMS}) for each scenario.

3.5.1 Measurement Scenarios

The measurement scenarios are shown in Figures 3.5 and 3.6. Figure 3.5(a) shows the outdoor scenario and the 5 measured locations. The distances range from 4.1 to 16.3 m, where behind location 2 is a tree and behind location 4 is a big building made of concrete and big metalized windows (see Figures 3.5(b) and 3.5(c)). The second scenario (see Figures 3.5(d)-(f)), was a workshop with big machines and cars. Three LOS locations were measured and one NLOS behind a metal cabinet. The distances range from 6.4 m to 18.1 m. Note, that Location 4 was a LOS scenario, because the antenna is mounted higher than the car. Figure 3.5(g) shows the office corridor LOS environment, where measurements have been taken at 5 m, 10 m, 15 m, 20 m, 30 m, 40 m and 50 m. The corridor is nearly empty. The walls are made of concrete and several metal doors are present. Next, two scenarios offices NLOS are measured, where one wall separates transmitter (TX) and receiver (RX) (see Figures 3.6(a)-(c) and Figures 3.6(d)-(f)). The wall is, at different locations, made of plaster, bricks or concrete. The distances range from approximately 2.5 m to 7.5 m. Both measurement scenarios are combined in the further analysis to achieve a better estimation of the channel parameters. The last measurements are performed in a residential NLOS environment depicted in Figure 3.6(g). The signals are transmitted through several concrete walls. The rooms are relatively small and the measurements are taken between approximately 2.5 m and 6.5 m. The rooms are a bedroom (TX), a living room (1,2,4), a kitchen (7), a corridor (3), a restroom (5) and a bathroom (6).

The following settings were used for the demonstrator. The carrier frequency f_c=4.5 GHz, the signal bandwidth represents B_s=500 MHz, PRF=500 MHz, $1/T$=2 Gsamples/s, and the measurement equipment was synchronized. Thus, undersampling was applied, where the signal is downconverted to an intermediate frequency of 500 MHz, which allows the sampling of longer sequences in comparison to passband sampling. Note, that due to the large input filter bandwidth of 3 GHz some noise is aliased into the desired band. On the other hand, the high-end quality of the measurement equipment still shows a low noise floor. Table 3.2 shows the IEEE 802.15.4a-parameters of the measured signals, where $Ch_{\#}$ is the channel number and $C_{\#}$ is the preamble code number. The measurements are performed according to the European transmission regulations [31]. Several locations were measured in every scenario. At each location 15 measurements were performed on a 5x3 grid, which allows the analysis of the small scale fading (SSF) [45]. In the outdoor and the industrial environment a spacing 5 and 7.5 cm is applied for the 5 measurement direction and the other one respectively. The grid had

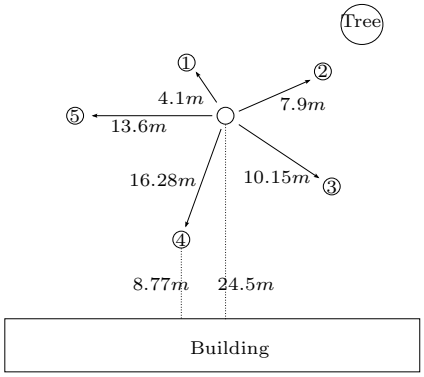

(a) ([39], © [2009] IEEE)

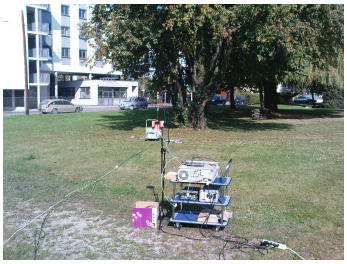

(b)

(c)

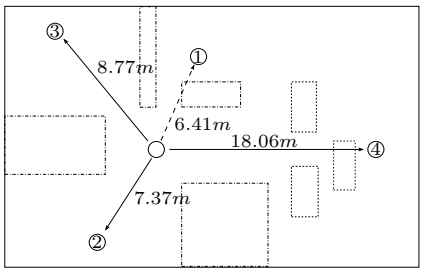

(d) ([39], © [2009] IEEE)

(e)

(f)

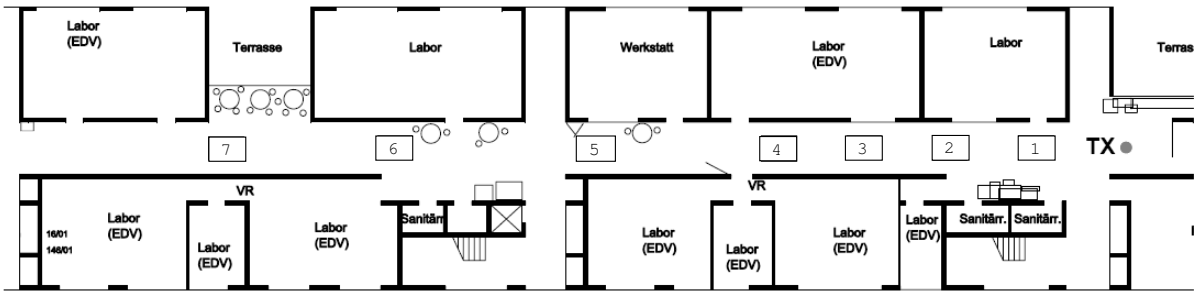

(g)

(h)

(i)

Figure 3.5 Measurement scenarios. (a)-(c): Outdoor LOS environment, (b) Transmitter (TX), (c) Receiver (RX) Location 2; (d)-(f): Industrial LOS/NLOS environment, (d) Map: (dashed-dotted) cabinets, (dashed) cars, (dashed arrow) NLOS scenario, (e) TX, (f) RX; (g)-(i): Office corridor LOS, (h) TX, (i) RX location ;

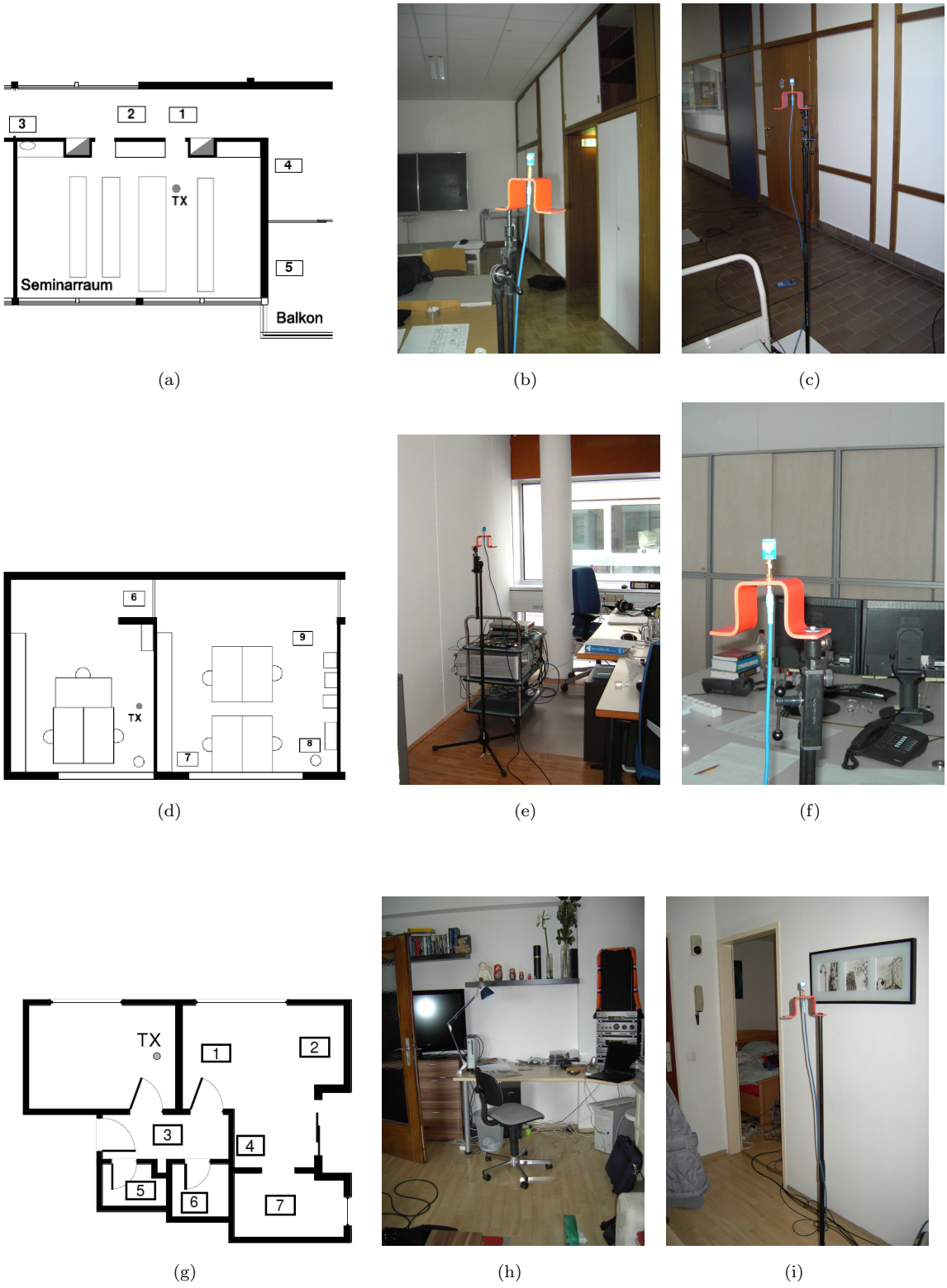

Figure 3.6 Measurement scenarios. (a)-(c): Office NLOS 2: (b) TX, (c) RX Location 2; (d)-(f): Office NLOS 1: (e) TX, (f) RX Location 9; (g)-(i): Residential NLOS (h) RX Location 2, (i) RX Location 3

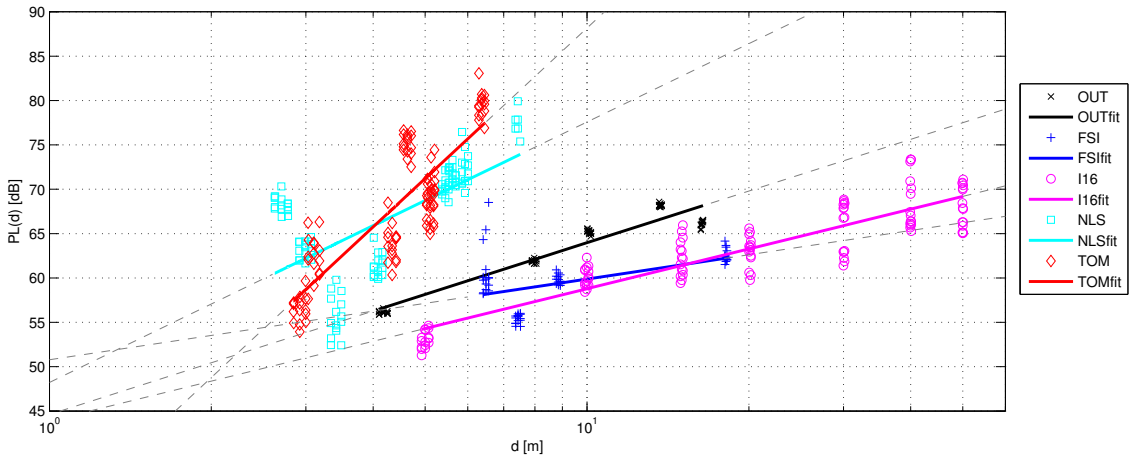

Figure 3.7 Pathloss of the measurement campain. The following abbreviations are defined: Outdoor (OUT), industrial (FSI), office LOS corridor (I16), residential (TOM) environment and the NLOS office scenarios (NLS). The `fit` extension to the scenario names means the fitted pathloss models. The dashed lines are the extrapolated values of the pathloss models.

a spacing of 10cm in both directions for the other scenarios. The transmitter is stationary while the receiver is moved to the specific positions.

3.5.2 Pathloss Model

The pathloss (PL) [dB] is defined as follows

$$\begin{aligned} \mathrm{PL} = 10\log\frac{P_{\mathrm{TX}}}{P_{\mathrm{RX}}} &= 10\log\frac{\frac{E_p}{T_{\mathrm{avg}}}}{\frac{1}{T_{\mathrm{avg}}}T\sum_{n=0}^{N-1}|\hat{h}'[n]|^2} \\ &= 10\log\frac{E_p}{T\sum_{n=0}^{N-1}|\hat{h}'[n]|^2} \end{aligned} \tag{3.10}$$

where P_{TX} is the transmit power, P_{RX} is the received power, T_{avg} is the averaging time. $\hat{h}'[n] = \hat{h}[n]$, if $|\hat{h}[n]|^2$ is greater than the noise level, else $\hat{h}'[n] = 0$. N limits the channel response to the last significant path. The pathloss model [dB] is defined as [46]

$$\mathrm{PL}(d) = \mathrm{PL}(d_0) + 10\eta\log\left(\frac{d}{d_0}\right) + S \tag{3.11}$$

where $\mathrm{PL}(d_0)$ [dB] is the reference pathloss at the reference distance $d_0 = 1$ m. d is the distance of the received signal, η is the pathloss exponent, and S is the zero-mean log-normal shadowing with standard deviation σ_s. Table 3.3 shows the values of the pathloss models, which are valid within the measured distances $d\,[m]$.

Figure 3.7 shows the measured and modeled pathloss with respect to their distances.A much higher pathloss is obtained in LOS in comparison to NLOS, which results from the wall penetration of the NLOS links. Significant deviations occur between the pathlosses of the LOS scenarios due to different contributions of multipath components. The pathloss factor varies strongly between the scenarios. In

Table 3.3 Pathloss model parameters

scen	*Walls*	$d\,[m]$	$\mathrm{PL}(d_0)\,[dB]$	η	$\sigma_s\,[dB]$
OUT	0	4 ... 17	44.61	1.94	1.43
FSI	0 ... 1	6 ... 18	50.78	1.03	2.09
I16	0	5 ... 50	43.89	1.49	1.15
NLS	1	2 ... 10	48.22	2.92	5.12
TOM	1 ... 3	2 ... 7	31.81	5.65	3.79

the LOS outdoor environment only a few multipath reflections arrive, thus the pathloss factor is very close to the free space factor 2. The waveguiding effects of the corridor lead to the low pathloss factor of ≈ 1.5, which corresponds to [47]. Significantly higher pathloss factors are obtained in the NLOS scenarios. A very high pathloss factor of ≈ 5.7 is obtained for the residential environment, because the signals have to penetrate more walls at higher distances. The low pathloss factor of the industrial environment is obtained form the attenuation of the NLOS location at 6 m.

Figures 3.8(a) and (b) show two example channel responses of the outdoor and industrial environment. The outdoor environment shows only a few multipath reflections, while the industrial environment shows many significant multipath reflections due to the big metallic machines. Thus, more energy is received for the industrial environment, which leads to a lower pathloss. The low pathloss of the office corridor scenario occurs due to strong reflections from the walls and wave guiding effects.

Strong LSF can be observed for the NLOS situations and the industrial environment, because of different materials and thicknesses of the walls or due to large reflectors e.g. big machines made of metal. Figure 3.8(c) shows the NLOS channel response from the residential environment, where the LOS component is strongly attenuated and the multipath components can also be greater and dominate the received signal strength. Thus, in addition to the LSF, significant local deviations occur, the SSF, which has to be taken into account for further analysis (see Chapter 6). Strong SSF effects are observable in the NLOS scenarios and the office LOS corridor environment.

3.5.3 RMS Delay Spread

The RMS delay spread is defined as (cf. [48])

$$\tau_{\mathrm{RMS}} = \sqrt{\frac{\sum_{n=0}^{N-1} \tau_n^2 |\hat{h}'[n]|^2}{\sum_{n=0}^{N-1} |\hat{h}'[n]|^2} - \left(\frac{\sum_{n=0}^{N-1} \tau_n |\hat{h}'[n]|^2}{\sum_{n=0}^{N-1} |\hat{h}'[n]|^2} \right)^2} \tag{3.12}$$

where τ_n is the excess delay of the n-th sample. Figure 3.9 shows the cumulative distribution function (CDF) of τ_{RMS} of the scenarios. It can be observed that the outdoor environment shows the highest RMS delay spread, since in this scenario only some reflections arrive at very large delays, which boosts τ_{RMS} (see Figure 3.8(a)). The industrial environment shows a much smaller τ_{RMS}, because many strong reflections arrive within short time. Strong reflections also occur in the LOS corridor environment, which leads to an RMS delay spread similar to the outdoor environment. Furthermore, the NLOS scenarios show the shortest RMS delay spread, because many multipath components are attenuated below the noise floor. The CDFs do not always achieve 1, because sometimes no signal

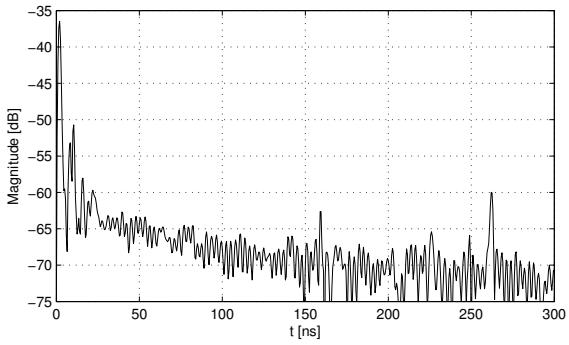

(a)

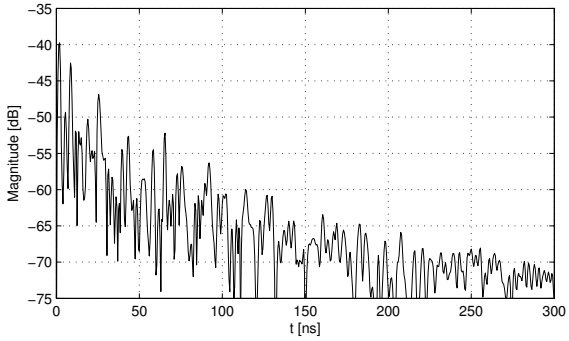

(b)

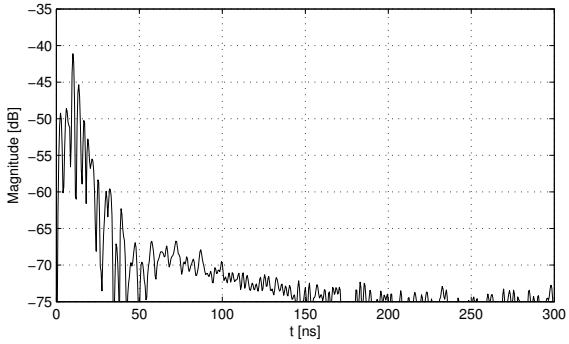

(c)

Figure 3.8 Example channel responses, (a): Channel response outdoor: Location 1 (d=4.1 m); (b): Channel response industrial: Location 2 (d=7.4 m); (c): Channel response residential: Location 1 (d=2.9 m)

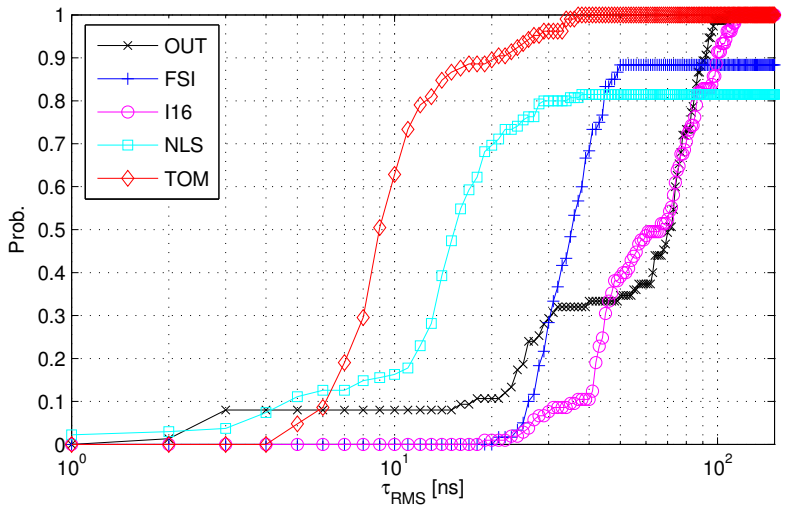

Figure 3.9 CDF of the RMS delay spread (τ_{RMS}) ([39], © [2009] IEEE)

was detected above the noise floor. It can be seen that the RMS delay spread strongly depends on the environment. It ranges for a quantile of 80% from 12 ns to approximately 90 ns.

3.6 Summary

A modular UWB demonstrator system is presented, where specific elements can be substituted for development and testing purposes. The concept conforms to the IEEE 802.15.4a standard and the baseband signal is generated by an FPGA. The demonstrator system implements a one-way communication setup which allows the analysis of communication and ranging performance of the standard and the hardware elements. The data is processed offline, which enables very flexible implementation of software receivers and ranging algorithms. A machted-filter receiver is introduced, which is used to verify the demonstrator system by channel measurements and analyzes in an office LOS, an industrial LOS/NLOS, an office corridor LOS, a residential NLOS environment, and two office NLOS scenarios. The pathloss model and the RMS delay spread are calculated for all scenarios. It has been observed that the parameters strongly depend on the environment. The pathloss exponent can be four times higher in NLOS than in LOS scenarios. The RMS delay spread varies for a quantile of 80% from 12 ns in the residential environment to approximately 90 ns in the office LOS corridor and the outdoor environment, respectively.

4

Statistical Modeling of the Energy Detector

This chapter analyzes the impact of the IEEE 802.15.4a system parameters on the ranging performance of energy detectors. The perfect autocorrelation properties of the standard do not prevent IPI for energy detectors, because of the non-linear squaring operation (see Figure 4.1). Thus, its effect is analyzed for the system parameters of the standard. As the standard shows many system parameters, the analysis can be used for further standardization activities especially for less flexible systems. The effect of IPI for energy detectors has not been studied to the best knowledge of the author. A ranging analysis with measured channel impulse responses is performed in an industrial LOS environment (see Section 3.5.1) is performed to define a working point of the energy detector and to show the achievable accuracy.

A statistical model for the energy detector for the detection of unknown deterministic signals is given in [50]. The modelling of energy detectors for communications can be found in [14, 51]. Low-complexity ranging with energy detectors has been a hot topic in research. Several papers have been published recently on that topic (e.g. [52–54]). An enhanced concept of energy detectors for channel estimation and ranging has been studied in a diploma thesis [55, 56]. In this work the energy detector slides over the preamble, which leads to a better resolution of the detector without increasing the sampling rate. This allows a more accurate estimation of the channels and the ranging.

The detection of the LOS component is of crucial importance for accurate and robust ranging. Unfortunately the LOS is not always the strongest component of the channel impulse response (e.g. [52]). Thus, several approaches have been studied in recent years. Maximum likelihood estimators show high computational effort and/or need apriori knowledge of the channel, which is not always available [1]. Low-complexity and more practical ranging algorithms are usually threshold based, where the first component exceeding a specific threshold is taken as reference for arrival time and range estimation. One drawback of these approaches is that the optimal value of this threshold is hard to define, because this value depends strongly on the environment. A good overview on threshold-based ranging algorithms is given in [53].

The rest of this chapter is organized as follows: Section 4.1 gives an overview of the energy detector, while a statistical analysis of the receiver is given in Section 4.2, which is analyzed in detail in Section 4.4 with measured channel impulse responses of an industrial LOS environment. The ranging algorithm

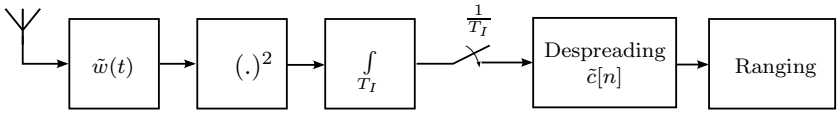

Figure 4.1 Energy detector (cf. [57], © [2010] IEEE)

is presented in Section 4.3 and the ranging performance is evaluated in Section 4.4. Finally, Section 4.5 sums up the results.

4.1 System Model

The energy detector works as shown in Figure 4.1. The signal is received by a UWB antenna and filtered by a bandpass filter, which ideally is a filter matched to the pulse shape. Next, the signal is squared and integrated for short time periods T_I. The length of T_I also defines the sampling period. It causes a mean absolute error (MAE) greater or equal $T_I/4$ [52], which limits T_I to a few ns for highly accurate ranging. The signal is correlated and despread with the corresponding despreading code $\tilde{c}[n]$. This delivers the channel response, where the ranging algorithm is applied.

4.2 Statistical Analysis

This section analyzes the first and second-order statistics of the energy detector for ranging in IEEE 802.15.4a. For this purpose, again only the preamble is modeled and analyzed, because it is the most important signal part for ranging. The analysis is based on the signal model of the previous section, in which the received signal has been defined in (3.3). Next, $r_a(t)$ is bandpass filtered by $\tilde{w}_r(t) = \tilde{w}(-t)$, which is a filter matched to the pulse. It follows

$$r_{\mathrm{BP}}(t) = s(t) * h_c(t) * \tilde{w}(-t) + \nu(t) * \tilde{w}(-t) \ . \tag{4.1}$$

The detector output after squaring, integration and sampling is given by

$$x[n] = \int_{nT_I}^{(n+1)T_I} \left(\sum_{m=0}^{M-1} c_m \phi_{\tilde{w}}(t - mLT_{\mathrm{chip}}) * h_c(t) + \nu_{\mathrm{BP}}(t) \right)^2 dt \tag{4.2}$$

where $\phi_{\tilde{w}}(t)$ is the autocorrelation function of the pulse shape and the band limited noise is given by $\nu_{\mathrm{BP}}(t) = \nu(t) * \tilde{w}(-t)$. The channel response $g(t) = \phi_{\tilde{w}}(t) * h_c(t)$. The estimated channel response

$y[n]$ is obtained by despreading $x[n]$,

$$\begin{aligned} y[n] &= \sum_{q=0}^{N_{\text{sync}}-1} \sum_{i=0}^{N_s-1} \tilde{c}_i \, x[n + iLN_{\text{chip}} + q\, N_s\, LN_{\text{chip}}] \\ &= \underbrace{\sum_{q=0}^{N_{\text{sync}}-1} \sum_{i=0}^{N_s-1} \tilde{c}_i \int_{nT_I+iLT_{\text{chip}}+qT_{\text{psym}}}^{(n+1)T_I+iLT_{\text{chip}}+qT_{\text{psym}}} \left(\sum_{m=0}^{M-1} c_m g(t - mLT_{\text{chip}}) \right)^2 dt}_{y_{ss}[n]} \\ &\quad + \underbrace{2 \sum_{q=0}^{N_{\text{sync}}-1} \sum_{i=0}^{N_s-1} \tilde{c}_i \int_{nT_I+iLT_{\text{chip}}+qT_{\text{psym}}}^{(n+1)T_I+iLT_{\text{chip}}+qT_{\text{psym}}} \sum_{m=0}^{M-1} c_m g(t - mLT_{\text{chip}}) \nu_{\text{BP}}(t)\, dt}_{y_{s\nu}[n]} \\ &\quad + \underbrace{\sum_{q=0}^{N_{\text{sync}}-1} \sum_{i=0}^{N_s-1} \tilde{c}_i \int_{nT_I+iLT_{\text{chip}}+qT_{\text{psym}}}^{(n+1)T_I+iLT_{\text{chip}}+qT_{\text{psym}}} \nu_{\text{BP}}^2(t)\, dt}_{y_{\nu\nu}[n]} \\ &= y_{ss}[n] + y_{s\nu}[n] + y_{\nu\nu}[n] \end{aligned} \tag{4.3}$$

where T_{psym} is the preamble symbol duration and N_s is the preamble sequence code length. The code despreading is performed symbol-wise with $\sum_q$ and $\sum_i$ with the despreading code $\tilde{c}_i$. Two despreading codes are analyzed in this paper, which are shown in Figure 4.2. The first one shows perfect circular crosscorrelation properties to the squared $\mathbf{c}_s$ (see Figure 4.2(c)), which means that only for a delay of zero the crosscorrelation is not zero. On the other hand, the code is not zero-mean. It is shortly denoted as $\tilde{\mathbf{c}}_{\text{NZM}}$. $\tilde{\mathbf{c}}_{\text{NZM}}$ is created by squaring $\mathbf{c}_s$ and setting all zeros to -1 [44] (see Figure 4.2(b)). The other code $\tilde{\mathbf{c}}_{\text{ZM}}$ is again obtained by squaring $\mathbf{c}_s$, but all zero values are set to $-16/15$ and $-64/63$ for short and long preamble symbols respectively [58](see Figure 4.2(d)). Thus, the code is zero mean but looses the perfect crosscorrelation properties, which can be observed in Figure 4.2(e). $y_{ss}[n]$ is the signal-by-signal term, $y_{s\nu}[n]$ is the signal-by-noise cross term and $y_{\nu\nu}[n]$ is the noise-by-noise term.

The expected value of $y[n]$ is given by

$$\text{E}\{y[n]\} = \text{E}\{y_{ss}[n]\} + \text{E}\{y_{s\nu}[n]\} + \text{E}\{y_{\nu\nu}[n]\} \tag{4.4}$$

and the variance is obtained from

$$\begin{aligned} \text{var}\{y[n]\} = &\text{var}\{y_{ss}[n]\} + \text{var}\{y_{s\nu}[n]\} + \text{var}\{y_{\nu\nu}[n]\} \\ &+ 2\text{cov}\{y_{ss}[n], y_{s\nu}[n]\} + 2\text{cov}\{y_{s\nu}[n], y_{\nu\nu}[n]\} + 2\text{cov}\{y_{ss}[n], y_{\nu\nu}[n]\} \end{aligned} \tag{4.5}$$

where all covariance terms $\text{cov}\{.,.\}$ become zero since $y_{ss}[n]$ is deterministic and $y_{s\nu}[n]$ is independent from $y_{\nu\nu}[n]$ (see Appendix D.1). Thus, it follows that

$$\text{var}\{y[n]\} = \text{var}\{y_{ss}[n]\} + \text{var}\{y_{s\nu}[n]\} + \text{var}\{y_{\nu\nu}[n]\} \ . \tag{4.6}$$

4.2.1 Signal-by-Signal Term $y_{ss}[n]$

$y_{ss}[n]$ is the deterministic part of the signal. Thus $\text{E}\{y_{ss}[n]\} = y_{ss}[n]$ and $\text{var}\{y_{ss}[n]\} = 0$. The inter pulse interference (IPI) is analyzed for $y_{ss}[n]$. It is assumed, that the maximum excess delay $\tau_{\max}$

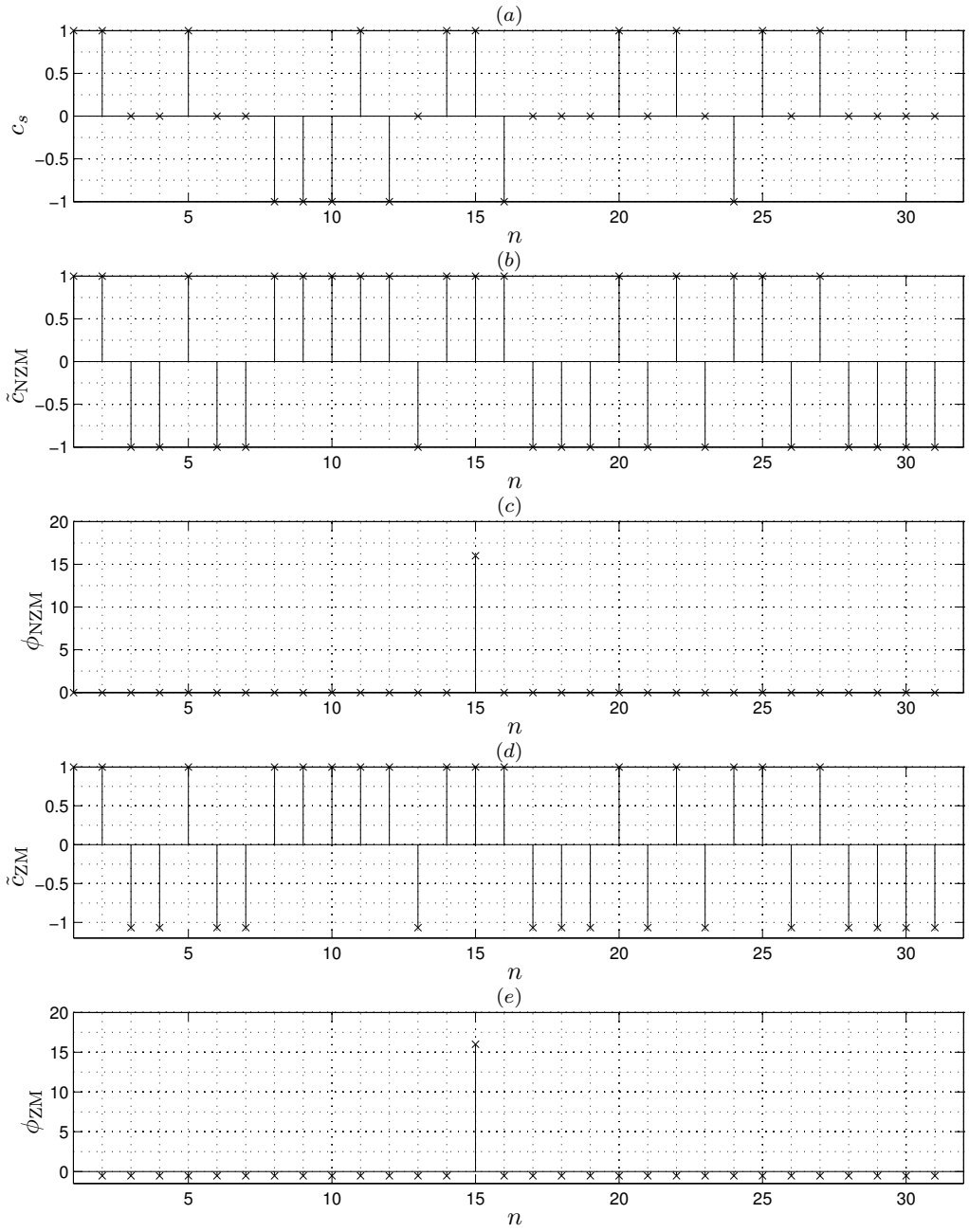

Figure 4.2 Code correlations for preamble code number 6: (a) preamble code sequence $\mathbf{c}_s$, (b) NZM symbol $\tilde{c}_{\mathrm{NZM}}$, (c) circular autocorrelation of the NZM code ϕ_{NZM}, (d) ZM symbol $\tilde{c}_{\mathrm{ZM}}$, (e) autocorrelation of the ZM code ϕ_{ZM}

is less than the code symbol length T_{psym}, such that the crosscorrelation properties of the code are applicable. Furthermore, it is assumed that the code appears circularly in the received signal and the transients at the beginning and the end of the correlation sequence are ignored for simplicity. Thus, the first sum in (4.3) simplifies to a factor of N_{sync} and

$$y_{ss}[n] = N_{\mathrm{sync}} \sum_{i=0}^{N_s-1} \sum_{m=0}^{M-1} \sum_{k=-m}^{M-m-1} c_m c_{(m+k)} \tilde{c}_i \int_{nT_I}^{(n+1)T_I} g(t-(m-i)LT_{\mathrm{chip}}) g(t-(m+k-i)LT_{\mathrm{chip}})\, dt. \tag{4.7}$$

Squaring leads to a second sum with an index m' that has been substituted by $m'{=}(m+k)$. With $l{=}i-m$ follows that

$$y_{ss}[n] = N_{\mathrm{sync}} \sum_{i=0}^{N_s-1} \sum_{l=i-M+1}^{i} \sum_{k=l-i}^{M+l-i-1} c_{(i-l)}\, c_{(i-l+k)}\, \tilde{c}_i \int_{nT_I}^{(n+1)T_I} g(t+lLT_{\mathrm{chip}}) g(t+(l-k)LT_{\mathrm{chip}})\, dt. \tag{4.8}$$

Due to the assumption of $\tau_{\max} < T_{\mathrm{psym}}$, and due to the periodicity of the preamble sequence, k and l can be limited to fixed intervals $[-N_s ... N_s - 1]$. The integral is independent of i, thus (4.8) simplifies to

$$y_{ss}[n] = N_{\mathrm{sync}} \sum_{k=-N_s}^{N_s-1} \sum_{l=-N_s}^{N_s-1} \phi_{\tilde{c}cc}[l,k] \int_{nT_I}^{(n+1)T_I} g(t+lLT_{\mathrm{chip}}) g(t+(l-k)T_{\mathrm{chip}})\, dt \tag{4.9}$$

where $\phi_{\tilde{c}cc}[l,k] = \sum_i \tilde{c}_i\, c_{(i-l)}\, c_{(i-l+k)}$ is used to express the despreading of the folded code sequences. This is illustrated for $\tilde{\mathbf{c}}_{\mathrm{NZM}}$ in Figure 4.3(a). The correlation function shows perfect matching with a high peak at $\phi_{\tilde{c}cc}[0,0]$ and zero sidelobes for $l = 0$ or $k = 0$. If both indices are $\neq 0$, the correlation function shows peaks, which correspond to IPI in the channel estimate $y[n]$. Due to the code, the IPI is attenuated by a factor of 4 and 8 in comparison to $\phi_{\tilde{c}cc}[0,0]$, for the short and long preamble, respectively. The location of the peaks (in k and l) depends on the code number, but the level does not. Note from (4.9) that the actual strength of the IPI also depends on the autocorrelation function of the received pulse at lag $k\,LT_{\mathrm{chip}}$ for an integration interval determined by $n\,T_I$ and a shift of $l\,LT_{\mathrm{chip}}$.

Figure 4.3(b) shows the code despreading function of the zero-mean despreading sequence $\tilde{\mathbf{c}}_{\mathrm{ZM}}$, $\phi_{\tilde{c}cc}[l,k]$ shows similar behavior. But since the perfect correlation property is lost, $\phi_{\tilde{c}cc}[l,k] \in [256, 0, -8.533, -66.133, +66.133]$. The value -8.533 occurs at $k = 0 \wedge l \neq 0$, which leads to a suppression of the magnitude of approximately 14.8 dB for the short preamble symbol and 21 dB for the long one. Note, these values are independent of N_{sync} and the location of the peaks is also despreading code independent (except $k = 0 \wedge l \neq 0$).

The index k models the lag of the code and channel autocorrelation functions in (4.8). For the analysis of the cross correlation properties of the codes, the IPI caused by the squaring device is canceled. Thus, we set $k = 0$ and we get

$$y_{ss}{}^{(0)}[n] = N_{\mathrm{sync}} \sum_{l=-N_s}^{N_s-1} \sum_{i=0}^{N_s-1} c_{(i-l)}^2 \tilde{c}_i \int_{nT_I}^{(n+1)T_I} g^2(t+lLT_{\mathrm{chip}})\, dt \tag{4.10}$$

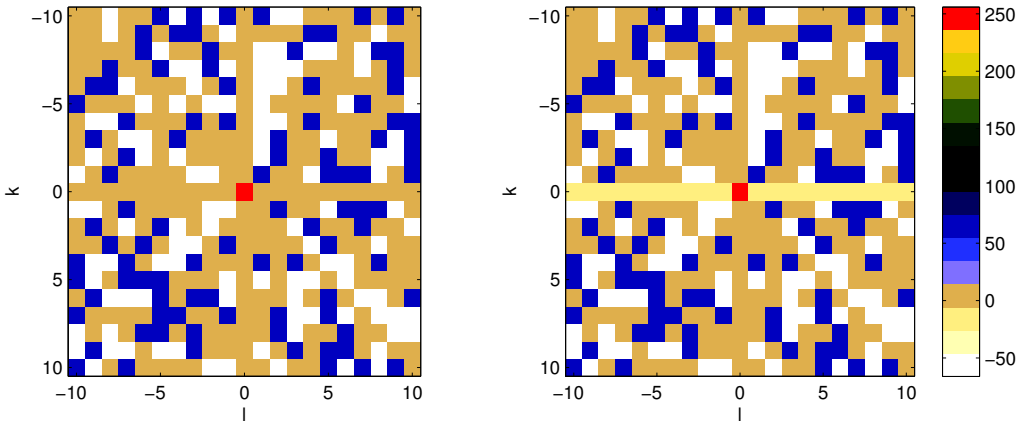

(a) ([59], © [2009] IEEE) (b)

Figure 4.3 Code despreading function $\phi_{\tilde{c}cc}$ of code c6 with N_{sync}=16 using despreading code (a) $\tilde{\mathbf{c}}_{\text{NZM}}$ and (b) $\tilde{\mathbf{c}}_{\text{ZM}}$.

which includes the desired term. Defining the received channel response energy $E_g(a, T_I) = \int_a^{a+T_I} g^2(t)dt$ and $\phi_{\tilde{c}cc}[l, k] = \xi$ for $k = 0$ and $l \neq 0$, (4.10) is rewritten by

$$\begin{aligned} {y_{ss}}^{(0)}[n] =& \frac{N_s + 1}{2} N_{\text{sync}} E_g(nT_I, T_I) \\ &+ \xi N_{\text{sync}} \sum_{l=-N_s}^{N_s-1} E_g(nT_I + lLT_{\text{chip}}, T_I)|_{l\neq 0} \end{aligned} \tag{4.11}$$

where $N_{\text{sync}}\,(N_s + 1)/2$ is the number of transmitted pulses in the preamble. The first part of (4.11) is the desired term, which is IPI free, and the second term contains the IPI from the crosscorrelation. The influence of the IPI is attenuated by ξ for the specific codes. $\xi = 0$ for $\tilde{\mathbf{c}}_{\text{NZM}}$, $\xi = -0.533$ for the short preamble of $\tilde{\mathbf{c}}_{\text{ZM}}$ and $\xi = -0.508$ for the long preamble symbols of $\tilde{\mathbf{c}}_{\text{ZM}}$. Thus, it is shown that $\tilde{\mathbf{c}}_{\text{NZM}}$ cancels this part of the IPI and increases the robustness by the second term in comparison to $\tilde{\mathbf{c}}_{\text{ZM}}$.

4.2.2 Signal-by-Noise Term $y_{s\nu}[n]$

The expected value of the signal-by-noise term is given by

$$\begin{aligned} \mathrm{E}\{y_{s\nu}\} &= 2 \sum_{q=0}^{N_{\text{sync}}-1} \sum_{i=0}^{N_s-1} \tilde{c}_i \int_{nT_I}^{(n+1)T_I} \sum_{m=0}^{M-1} c_m g(t - (m-i)LT_{\text{chip}} + qT_{\text{psym}}) \mathrm{E}\{\nu_{\text{BP}}(t)\}\, dt \\ &= 0, \end{aligned} \tag{4.12}$$

because the noise term is zero mean. Thus, it follows for the variance $\mathrm{var}\{y_{s\nu}[n]\} = \mathrm{E}\{y_{s\nu}^2[n]\}$ and

$$\begin{aligned}\mathrm{var}\{y_{s\nu}[n]\} = 4 \sum_{q=0}^{N_{\mathrm{sync}}-1} \sum_{q'=0}^{N_{\mathrm{sync}}-1} \sum_{i=0}^{N_s-1} \sum_{i'=0}^{N_s-1} \sum_{m=0}^{N_s-1} \sum_{k=-m}^{M-m-1} c_m c_{(m+k)} \tilde{c}_i \tilde{c}_{i'} \\ \times \int_{nT_I}^{(n+1)T_I} \int_{nT_I}^{(n+1)T_I} g(t + (i-m)LT_{\mathrm{chip}} + qT_{\mathrm{psym}}) g(\tau + (i'-m-k)LT_{\mathrm{chip}} + q'T_{\mathrm{psym}}) \\ \times \mathrm{E}\{\nu_{\mathrm{BP}}(t + iLT_{\mathrm{chip}} + qT_{\mathrm{psym}}) \nu_{\mathrm{BP}}(\tau + i'LT_{\mathrm{chip}} + q'T_{\mathrm{psym}})\}\, d\tau\, dt\,.\end{aligned} \tag{4.13}$$

The noise is uncorrelated for a time delay of T_{psym}, which forces $q{=}q'$ and $\sum_q(...){=}N_{\mathrm{sync}} \times (...)$. Furthermore, it is also uncorrelated for a lag of LT_{chip}, hence it follows that $i = i'$ and

$$\begin{aligned}\mathrm{var}\{y_{s\nu}[n]\} = 4N_{\mathrm{sync}} \sum_{i=0}^{N_s-1} \sum_{m=0}^{N_s-1} \sum_{k=-m}^{M-m-1} c_m c_{(m+k)} \tilde{c}_i^2 \\ \times \int_{nT_I}^{(n+1)T_I} \int_{nT_I}^{(n+1)T_I} g(t + (i-m)LT_{\mathrm{chip}}) g(\tau + (i-m-k)LT_{\mathrm{chip}}) \\ \times \mathrm{E}\{\nu_{\mathrm{BP}}(t + iLT_{\mathrm{chip}}) \nu_{\mathrm{BP}}(\tau + iLT_{\mathrm{chip}})\}\, d\tau\, dt\,.\end{aligned} \tag{4.14}$$

As $\tilde{c}_i \in [1, -1]$, it follows that for $\tilde{c}_{\mathrm{NZM}}$ ${\tilde{c}_i}^2 = 1$ and for $\tilde{c}_{\mathrm{ZM}}$ $\tilde{c}_i^2 \approx 1$. By substituting $\tau = t + \mu$ and $\mathrm{E}\{\nu_{\mathrm{BP}}(t)\nu_{\mathrm{BP}}(t+\mu)\} = N_0/2\, \phi_{\tilde{w}}(\mu)$ (for the derivation see Appendix D.2), where $N_0/2$ is the two-sided noise spectral density, (4.14) reduces to

$$\begin{aligned}\mathrm{var}\{y_{s\nu}[n]\} = 2N_0 N_{\mathrm{sync}} \sum_{i=0}^{N_s-1} \sum_{m=0}^{M-1} \sum_{k=-m}^{M-m-1} c_m c_{(m+k)} \\ \times \int_{nT_I}^{(n+1)T_I} \int_{nT_I-t}^{(n+1)T_I-t} g(t + (i-m)LT_{\mathrm{chip}}) g(t + \mu + (i-m-k)LT_{\mathrm{chip}})\, \phi_{\tilde{w}}(\mu)\, d\mu\, dt\,.\end{aligned} \tag{4.15}$$

Defining $l = i - m$ and substituting m, the integrals become independent of i. Next, the perfect autocorrelation properties of $\mathbf{c}$ are used, thus only at $k = 0$ the term is non-zero. In other words the signal-by-noise term does not depend on sidelobes of the code despreading or channel correlation function. Thus, (4.15) reduces to

$$\begin{aligned}\mathrm{var}\{y_{s\nu}[n]\} =& 2N_0 N_{\mathrm{sync}} \sum_{i=0}^{N_s-1} \sum_{l=i}^{M+i-1} c_{(i-l)}^2 \int_{nT_I}^{(n+1)T_I} \int_{nT_I-t}^{(n+1)T_I-t} g(t + lLT_{\mathrm{chip}}) g(t + \mu + lLT_{\mathrm{chip}})\, \phi_{\tilde{w}}(\mu)\, d\mu\, dt \\ =& 2N_0 N_{\mathrm{sync}} \sum_{i=0}^{N_s-1} \sum_{l=i}^{M+i-1} c_{(i-l)}^2 \int_{nT_I}^{(n+1)T_I} g(t + lLT_{\mathrm{chip}}) \int_{nT_I-t}^{(n+1)T_I-t} g(t + \mu + lLT_{\mathrm{chip}})\, \phi_{\tilde{w}}(\mu)\, d\mu\, dt \\ \approx& 2N_0 N_{\mathrm{sync}} \sum_{i=0}^{N_s-1} \sum_{l=i}^{M+i-1} c_{(i-l)}^2 \int_{nT_I}^{(n+1)T_I} g(t + lLT_{\mathrm{chip}}) \tilde{g}(t + lLT_{\mathrm{chip}}) dt\end{aligned} \tag{4.16}$$

where $\tilde{g}(t) = \int_{-\infty}^{\infty} g(\mu)\phi_{\tilde{w}}(t-\mu)$. As different integration limits occur in comparison to (4.16) for the convolution, the approximation notation has been chosen. Furthermore, $\tilde{g}(t) \approx g(t)$, since the

bandwidth of the pulse shape is equal to the bandwidth of the input filter. Thus, (4.16) simplifies approximately to

$$\begin{aligned}\mathrm{var}\{y_{s\nu}[n]\} \approx & 2N_0 N_{\mathrm{sync}} \sum_{i=0}^{N_s-1} \sum_{l=i}^{M+i-1} c_{(i-l)}^2 \int_{nT_I}^{(n+1)T_I} g^2(t + lLT_{\mathrm{chip}})dt \\ = & (N_s+1) N_{\mathrm{sync}} N_0 \sum_{l=-N_s}^{N_s-1} E_g(nT_I + lLT_{\mathrm{chip}}, T_I)\end{aligned} \tag{4.17}$$

Note that the signal-by-noise term cannot suppress IPI. It depends on the accumulated channel energies for energy samples spaced by lLT_{chip}.

4.2.3 Noise-by-Noise Term

Certainly, $\tilde{\mathbf{c}}_{\mathrm{ZM}}$ shows $\mathrm{E}\{y_{\nu\nu}[n]\} = 0$. The expected value for $\tilde{\mathbf{c}}_{\mathrm{NZM}}$ is given by

$$\begin{aligned}\mathrm{E}\{y_{\nu\nu}[n]\} = & \sum_{q=0}^{N_{\mathrm{sync}}-1} \sum_{i=0}^{N_s-1} \tilde{c}_i \int_{nT_I + iLT_{\mathrm{chip}} + qT_{\mathrm{psym}}}^{(n+1)T_I + iLT_{\mathrm{chip}} + qT_{\mathrm{psym}}} \mathrm{E}\left\{\nu_{\mathrm{BP}}^2(t)\right\} dt \\ = & \frac{N_0}{2} T_I N_{\mathrm{sync}} \phi_{\tilde{w}}(0)\end{aligned} \tag{4.18}$$

since $\sum_{i=0}^{N_s-1} \tilde{c}_i = 1$ and $\mathrm{E}\left\{\nu_{\mathrm{BP}}^2(t)\right\} = N_0/2\phi_{\tilde{w}}(0)$ (for the derivation see Appendix D.2), where $\phi_{\tilde{w}}(0)$ is the equivalent bandwidth.

The variance $\mathrm{var}\{y_{\nu\nu}[n]\} = \mathrm{E}\left\{y_{\nu\nu}^2[n]\right\} - \mathrm{E}^2\{y_{\nu\nu}[n]\}$. As assumed in Section 4.2.2 $q = q'$, $\sum_q(...) = N_{\mathrm{sync}} \times (...)$ and $i = i'$. Thus, the first term is given by

$$\mathrm{E}\left\{y_{\nu\nu}^2[n]\right\} = N_{\mathrm{sync}} \sum_{i=0}^{N_s-1} \tilde{c}_i^2 \int_{nT_I}^{(n+1)T_I} \int_{nT_I}^{(n+1)T_I} \mathrm{E}\left\{\nu_{\mathrm{BP}}^2(t + iLT_{\mathrm{chip}}) \nu_{\mathrm{BP}}^2(\tau + iLT_{\mathrm{chip}})\right\} dt\, d\tau \tag{4.19}$$

The fourth-order moment is reduced to second-order moments as shown in [60] and with $\tau = t + \mu$ it follows

$$\begin{aligned}\mathrm{E}\left\{y_{\nu\nu}^2[n]\right\} = & N_{\mathrm{sync}} \sum_{i=0}^{N_s-1} \tilde{c}_i^2 \Bigg\{ \int_{nT_I}^{(n+1)T_I} \int_{nT_I - t}^{(n+1)T_I - t} \mathrm{E}\left\{\nu_{\mathrm{BP}}^2(t + iLT_{\mathrm{chip}})\right\} \mathrm{E}\left\{\nu_{\mathrm{BP}}^2(t + \mu + iLT_{\mathrm{chip}})\right\} \\ & + 2\mathrm{E}^2\{\nu_{\mathrm{BP}}(t + iLT_{\mathrm{chip}}) \nu_{\mathrm{BP}}(t + \mu + iLT_{\mathrm{chip}})\}\, d\mu\, dt \Bigg\} .\end{aligned} \tag{4.20}$$

The first part of (4.20) cancels with $\mathrm{E}^2\{y_{\nu\nu}[n]\}$ in the variance calculation. $\sum_{i=0}^{M-1} \tilde{c}_i^2 = M$ for $\tilde{\mathbf{c}}_{\mathrm{NZM}}$ due to $\tilde{c}_i \in [+1, -1]$ and $\sum_i \tilde{c}_i^2 \approx M$ for $\tilde{\mathbf{c}}_{\mathrm{ZM}}$. Thus, the variance is given by

$$\begin{aligned}\mathrm{var}\{y_{\nu\nu}[n]\} = & 2M \int_{nT_I}^{(n+1)T_I} \int_{nT_I - t}^{(n+1)T_I - t} \left(\frac{N_0}{2} \phi_{\tilde{w}}(\mu)\right)^2 d\mu\, dt \\ = & \frac{{N_0}^2}{2} N_{\mathrm{sync}} N_s T_I W_{\mathrm{RRC}}\end{aligned} \tag{4.21}$$

where $M = N_{\mathrm{sync}} N_s$ and W_{RRC} is an equivalent bandwidth defined as $W_{\mathrm{RRC}} = \int_{-T_{\tilde{w}}}^{T_{\tilde{w}}} \phi_{\tilde{w}}^2(\mu) d\mu$. $T_{\tilde{w}}$ is the pulse length.

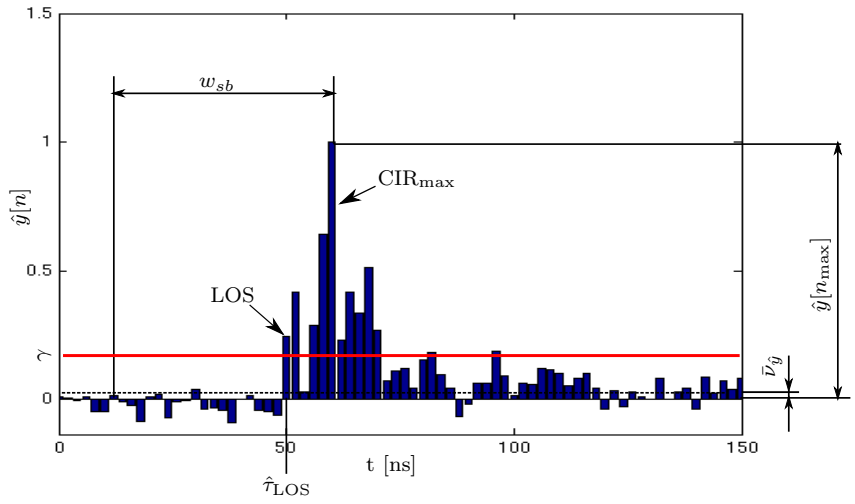

Figure 4.4 Principle of the Jump Back and Search Forward Algorithm

4.3 Threshold-Based Ranging Algorithm

The detection of the LOS component for range estimation is implemented as a jump back and search forward (JBSF) algorithm [53] applied to the estimated channel response $\hat{y}[n]$. Figure 4.4 illustrates the principle of the JBSF algorithm, which is shown on an example channel impulse response measured in the NLOS residential environment (see Section 3.5). Obviously, the LOS component is not the strongest component of the CIR and a maximal energy selection (MES) algorithm, which takes just the strongest component, would lead to a large error. Thus, a JBSF algorithm is applied to the experiments to detect the LOS component. First the maximum of $\hat{y}[n]$ is detected and within a search back window with length w_{sb} the first sample that exceeds a specific threshold γ is chosen as the estimated LOS component.

The estimated time of arrival $\hat{\tau}_{\mathrm{LOS}}$ is given by

$$\hat{\tau}_{\mathrm{LOS}} = \left[\min_{n \in [n_{\max} - w_{sb}, n_{\max}]} \{ n | \, \hat{y}[n] \geq \gamma \} - \frac{1}{2} \right] T \tag{4.22}$$

where $n_{\max} = \mathrm{argmax}(\hat{y}[n])$ and T is the sampling interval. Note, for the coherent receiver the ranging is based on the absolute value of $\hat{y}[n]$ (see Chapter 5). The threshold γ is defined as [61]

$$\gamma = \bar{\nu}_{\hat{y}} + c(\hat{y}[n_{\max}] - \bar{\nu}_{\hat{y}}) \tag{4.23}$$

where $\bar{\nu}_{\hat{y}}$ is the mean magnitude of the noise in $\hat{y}[n]$, and $0 < c \leq 1$ is a user-defined coefficient, where $c = 1$ implements MES. The optimal threshold depends on the channel statistics, which can vary strongly from scenario to scenario (see Chapter 3) and thus a general optimal threshold is difficult to define. In scenarios with high SNR a low threshold will lead to the most accurate results as the attenuated LOS component is detectable, while in scenarios with low SNR a higher threshold will lead to more robust results as the probability of detecting a noise component decreases [62]. Another factor of influence is the length of w_{sb}, because a longer search back window increases the probability that the LOS component is included, while it increases also the probability of detecting a strong noise component.

Table 4.1 Signals of the analysis

	Signal	**IPI**	**Noise**
Signal	$y''_{ss}[n]$	$y_{\mathrm{ipi}}[n]$	$y_{s\nu}[n]$
IPI	$y_{\mathrm{ipi}}[n]$	$y_{\mathrm{ipi}}[n]$	$y_{s\nu}[n]$
Noise	$y_{s\nu}[n]$	$y_{s\nu}[n]$	$y_{\nu\nu}[n]$

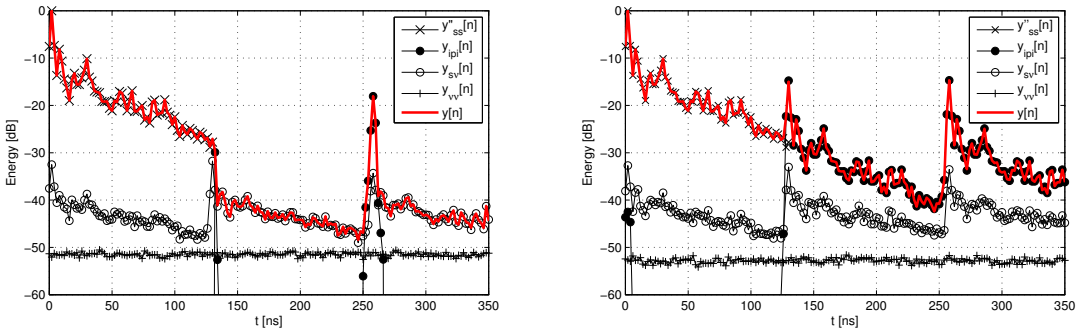

(a) (b)

Figure 4.5 Magnitude of the estimated channel response of code c6, $E_{\mathrm{rp}}/N_0 = 70$ dB, $L = 64$: (a) non-zero-mean despread code, (b) zero-mean despreading code ([59], © [2009] IEEE)

4.4 Verification

This section quantifies the effects of IPI and noise on the ranging performance with measured channel impulse responses in the industrial environment (see Section 3.5.1). Only the LOS measurements were taken. The channel impulse responses are convolved in a simulation framework with IEEE 802.15.4a compliant preamble codes and artificial noise is added according to the received preamble energy E_{rp} to N_0 ratio, where $E_{\mathrm{rp}} = M_1 E_g$. A time invariant channel is assumed over the whole preamble. The first part of this section gives a signal and IPI analysis. Next the system parameters are analyzed with respect to input and output SNRs and finally the ranging performance is determined with an empirically evaluated working point.

4.4.1 Signal and IPI Analysis

Table 4.1 shows the signal terms for the analysis, where $y''_{ss}[n]$ is the IPI-free signal-by-signal term, $y_{\mathrm{ipi}}[n]$ is the IPI term, $y_{s\nu}[n]$ is the signal-by-noise term and $y_{\nu\nu}[n]$ is the noise-by-noise term. The signal terms show up in multiple cells, which means the signal terms contain these specific (cross) parts. The specific signal terms are obtained by using only parts of the noisy received signal $r(t)$ as input for the energy detector. $y''_{ss}[n]$ is obtained by using $g(t)$ as input signal. The output had to be multiplied with $(N_s + 1)\, N_{\mathrm{sync}}/2$ to obtain the same energy as in the whole preamble. $y_{\mathrm{ipi}}[n]$ is obtained when $s(t)$ is used as input and $y''_{ss}[n]$ is subtracted. $y_{\nu\nu}[n]$ is obtained, when $\nu(t)$ is chosen as input signal. $y_{s\nu}[n]$ is obtained if $r(t)$ is chosen as input signal and all other terms are subtracted.

Figure 4.5(a) shows the estimated mean magnitude channel response of code c6 [20] under usage of

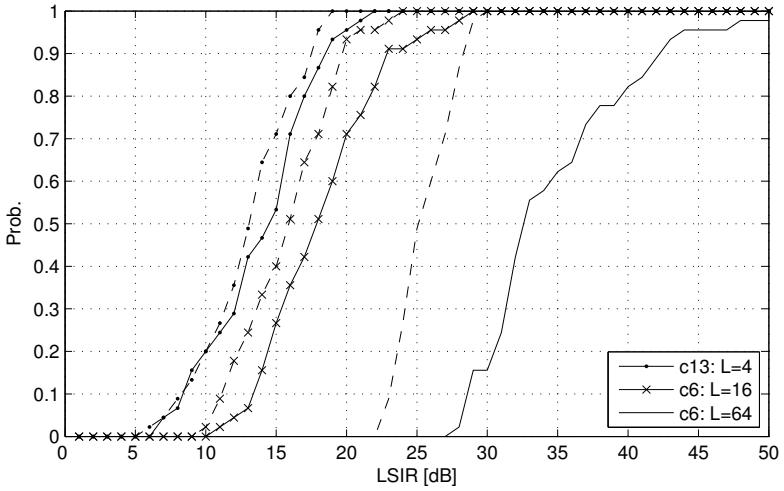

Figure 4.6 Cumulative distribution function (CDF) of LSIR with respect to δ_L for $\tilde{\mathbf{c}}_{\mathrm{NZM}}$ (solid) and $\tilde{\mathbf{c}}_{\mathrm{ZM}}$ (dashed) ([59], © [2009] IEEE)

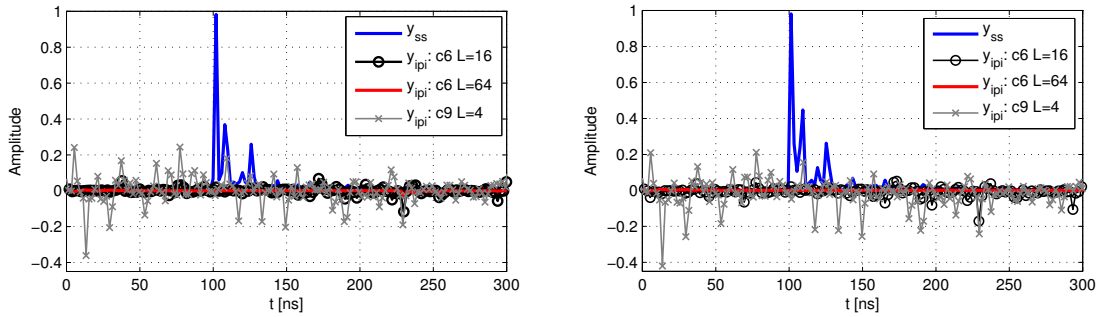

Figure 4.7 IPI Analysis for specific preamble codes using (a) $\tilde{c}_{\mathrm{NZM}}$ and (b) $\tilde{c}_{\mathrm{ZM}}$

$\tilde{\mathbf{c}}_{\mathrm{NZM}}$ with perfect correlation properties. The output signal of the receiver $y[n]$ is dominated from 0 to 125 ns by the $y''_{ss}[n]$ part. The IPI part is much less than -60 dB within this zone, but shows peaks every $k\,LT_{\mathrm{chip}}$, where the IPI parts are overlapping. The peaks depend on $\phi_{\tilde{c}cc}[l,k]$ of the specific code symbols. Between the peaks, the perfect cross-correlation properties attenuate the IPI to a negligible level and $y[n]$ is defined by the signal-by-noise term and the noise-by-noise term, see (4.17).

Figure 4.5(b) shows the output of $\tilde{\mathbf{c}}_{\mathrm{ZM}}$ and in contrast to $\tilde{\mathbf{c}}_{\mathrm{NZM}}$ the IPI dominates from 130 to 250 ns, due to the non-perfect crosscorrelation properties of the codes, see (4.10). Certainly, this relation will change for lower SNR values. The noise levels are approximately the same for both code sequences.

The LOS-component-to-IPI-Ratio (LSIR) is used as performance metric of the receiver and is defined as

$$\mathrm{LSIR}_{\mathrm{dB}} = 10\log\left\{\frac{y_{ss}^2[n_{\mathrm{LOS}}]}{\max\{|y_{\mathrm{ipi}}[n]|^2\}}\right\} \tag{4.24}$$

where $y_{ss}[n_{\mathrm{LOS}}]$ is the sample at n_{LOS} containing the line of sight component of $y_{ss}[n]$. Figure 4.6

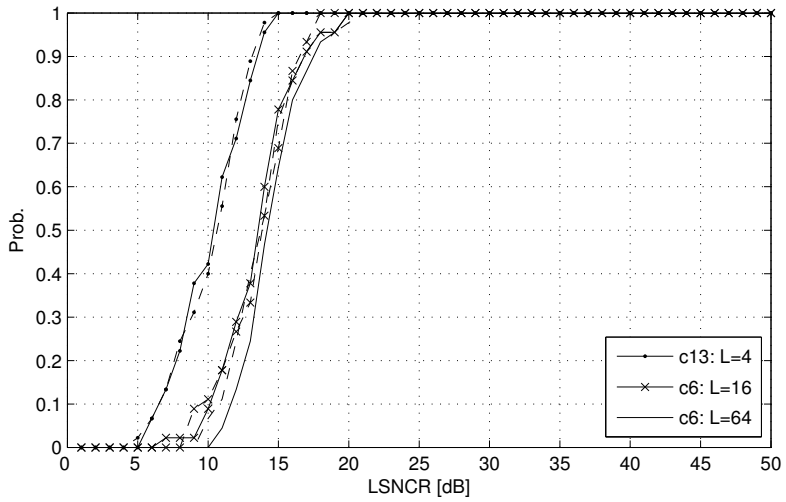

Figure 4.8 CDF of LSNCR with respect to L. The solid lines belong to $\tilde{\mathbf{c}}_{\mathrm{NZM}}$ and the dashed ones to $\tilde{\mathbf{c}}_{\mathrm{ZM}}$ ([59], © [2009] IEEE)

shows the effect of the spreading factor L on the LSIR. A higher L leads to higher LSIRs, due to less IPI. The long preamble (c13) shows the worst performance. Apparently, its increased despreading gain is not able to balance its closer spacing of preamble symbols using $L = 4$. The despreading sequence $\tilde{\mathbf{c}}_{\mathrm{ZM}}$ is limited because of its imperfect correlation properties with sidelobes at 30 dB, while $\tilde{\mathbf{c}}_{\mathrm{NZM}}$ can further improve the LSIR with c6 and $L = 64$. Furthermore, the LSIR is independent of the preamble symbol repetitions N_{sync}.

Figure 4.7 shows the effect of the preamble codes on the IPI for both despreading codes on an example channel impulse response. Obviously, IPI is negligible for the short preamble symbols with $L = 64$, while some IPI can be observed at $L = 16$ which can lead to false detection for low thresholds. The long preamble symbols show significant IPI which can harm the performance for ranging significantly. A comparison of $\tilde{c}_{\mathrm{NZM}}$ (see 4.7(a)) and $\tilde{c}_{\mathrm{ZM}}$ (see 4.7(a)) shows similar behavior for the specific codes.

The next performance metric is the LOS-Signal-to-Noise-Cross-Term Ratio (LSNCR), which is defined as follows

$$\mathrm{LSNCR}_{\mathrm{dB}} = 10 \log \left\{ \frac{y_{ss}^2[n_{\mathrm{LOS}}]}{\mathrm{var}\{y_{s\nu}[n]\}} \right\} . \tag{4.25}$$

The variance is sufficient, because $\mathrm{E}\{y_{s\nu}\}=0$ for both codes. Figure 4.8 shows the influence of IPI on LSNCR with respect to L, see (4.17). The simulations are performed with N_{sync}=16 and E_{rp}/N_0=25 dB for c6 (see working point 4.4.3) and E_{rp}/N_0=31 dB for c13, because four times more pulses are transmitted in c13. The performance of c6 is very similar for $L = 16$ and $L = 64$, which means that the IPI term is not decreasing for a higher spreading factor. The higher E_{rp}/N_0=31 of the long premable (c13) does not lead to better performance due the noise scales with the signal power (cf. (4.9) and (4.17)). It performs again worst due to the higher IPI, which causes a loss of approx. 3 dB in comparison to the others.

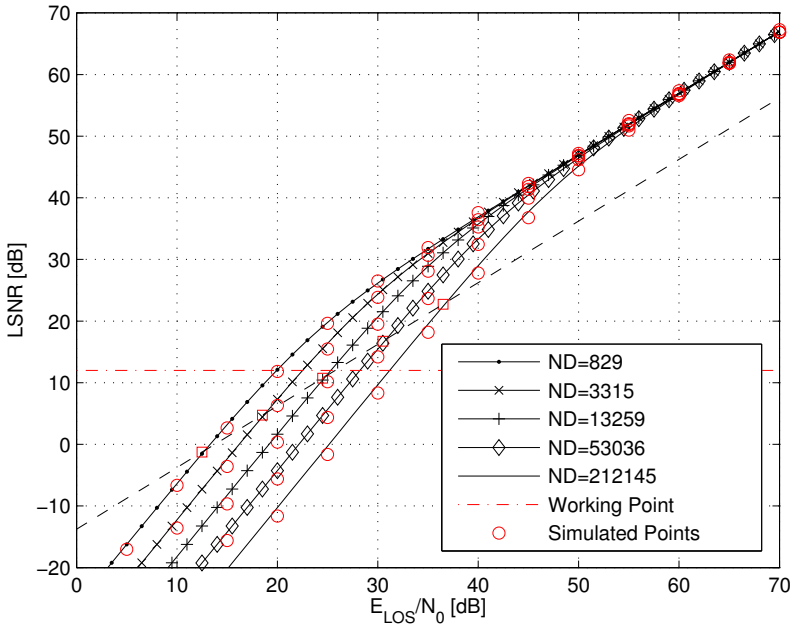

Figure 4.9 Relation of the detector input SNR E_{LOS}/N_0 and output SNR LSNR with respect to the noise dimensionality $\mathrm{ND} = N_s\, N_{\mathrm{sync}}\, T_I\, W_{RRC}$. The dashed line depicts the practical case, when the energy scales linearly with N_{pr} and the squares denote the crossing points. (cf. [59], © [2009] IEEE)

4.4.2 Noise Analysis

The analysis of the IPI free noise terms is done analytically. Simulations have shown that both despreading codes perform very similarly and so only one result is depicted. The LOS signal-to-noise-ratio is defined by

$$\begin{aligned}\mathrm{LSNR}_{\mathrm{dB}} &= 10\log\left(\frac{y_{ss}^2[n_{\mathrm{LOS}}]}{\mathrm{var}\{y_{s\nu}[n_{\mathrm{LOS}}]\} + \mathrm{var}\{y_{\nu\nu}[n]\}}\right) \\ &= 10\log\frac{2\left(\frac{E_{\mathrm{LOS}}}{N_0}\right)^2}{4\frac{E_{\mathrm{LOS}}}{N_0} + N_s N_{\mathrm{sync}} T_I W_{RRC}}\end{aligned} \tag{4.26}$$

where $E_{\mathrm{LOS}} = y_{ss}[n_{\mathrm{LOS}}]$. The first term of the denominator corresponds to the linear and the second to the quadratic noise term. The quadratic noise term depends on the receiver parameters, which can be combined to the noise dimensionality ND=$N_s\, N_{\mathrm{sync}}\, T_I\, W_{RRC}$ [14].

Figure 4.9 shows the relation of the detector input SNR E_{LOS}/N_0 and the output LSNR based on equation (4.26). The depicted curves are obtained by increasing N_{synch} by factors of 4 according to the preamble symbol repetitions defined by IEEE 802.15.4a[1], where the depicted curves corresponds to $N_{\mathrm{synch}} = [16, 64, 256, 1024, 4096]$, $N_s = 31$, $T_I = 2$ ns, and $W_{\mathrm{RRC}} \approx 1$ GHz. The curves are separated when the quadratic noise term dominates and they merge if the linear noise term is dominant. Increasing E_{LOS}/N_0 by 6 dB leads to LSNR +12 dB in the quadratic part and to +6 dB in the linear

[1]The preamble length with $N_{\mathrm{synch}} = 256$ is shown for visibility and is not defined in the standard.

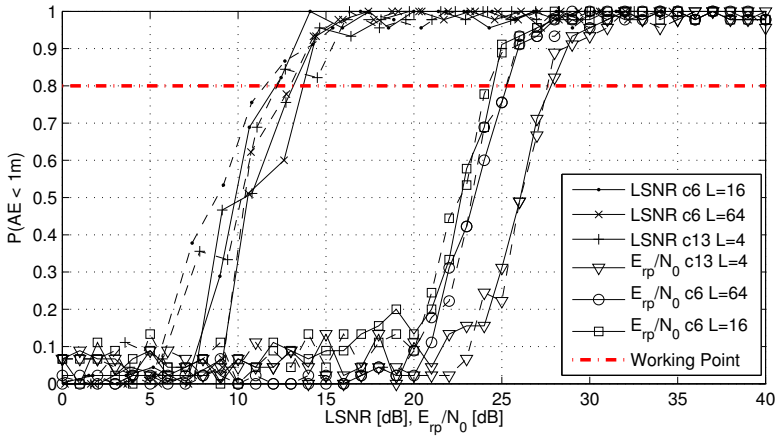

Figure 4.10 Probability of an abs. distance error < 1 m. The solid lines belong to $\tilde{\mathbf{c}}_{\mathrm{NZM}}$ and the dashed ones to $\tilde{\mathbf{c}}_{\mathrm{ZM}}$

one. The horizontal line illustrates the LSNR at a working point that corresponds to an outage probability of 20% for a leading edge detection algorithm (see Section 4.4.3). It can be seen that 3 dB more E_{LOS}/N_0 is required when the number of symbols is increased by a factor of 4. Note, the linear noise term is negligible at this working point. The dashed line illustrates the practical case when the transmitted signal energy increases proportionally with N_{sync}. It is evident that the LSNR increases at the same rate, despite the fact that the working point is within the region where the quadratic noise term dominates. This illustrates that increasing the number of preamble symbols is an efficient way to increase LSNR by transmitting more energy, although the ND is increased too.

4.4.3 Ranging Analysis

This section defines the working point of the energy detector based on E_{rp}/N_0 and LSNR. Figure 4.10 shows the probability of an absolute distance error less than 1 m with respect to the SNRs. The threshold of 1 m has been chosen, because the IEEE 802.15.4a standard is designed to achieve a localization accuracy of better than 1 m and so the working point can be determined. Artificial noise has been added to the measurements and 45 measurements are combined per SNR value. The detection of the LOS component is implemented according to the JBSF algorithm introduced in Section 4.3. The search back window has been defined by 30 ns (see [62] and [52]) and the optimal threshold has been chosen for each SNR value.

Since all curves are very steep, both SNRs show good correlation to the ranging error. We can also see that both despreading codes show similar performance. For the LSNR values the zero-mean codes shows slightly better performance, while for E_{rp}/N_0 no difference can be observed. As mentioned before, the c13 code uses 6 dB more energy but loses 3 dB due to the non coherent combining, which is observable in the discrepancy of the E_{rp}/N_0 curves. The performance of the c6 codes shows a slight better performance for $L = 16$. The working point with respect of LSNR varies slightly and a working point of $\mathrm{WP}_{\mathrm{LSNR}} = 12$ dB has been chosen for the rest of the work. As already shown in the previous section, the channel energy varies significantly between the scenarios and environments due to wall attenuations and multipath reflections. As the ranging accuracy depends on the detection of the LOS component, it depends on the LOS energy, which can be only a fraction of the whole

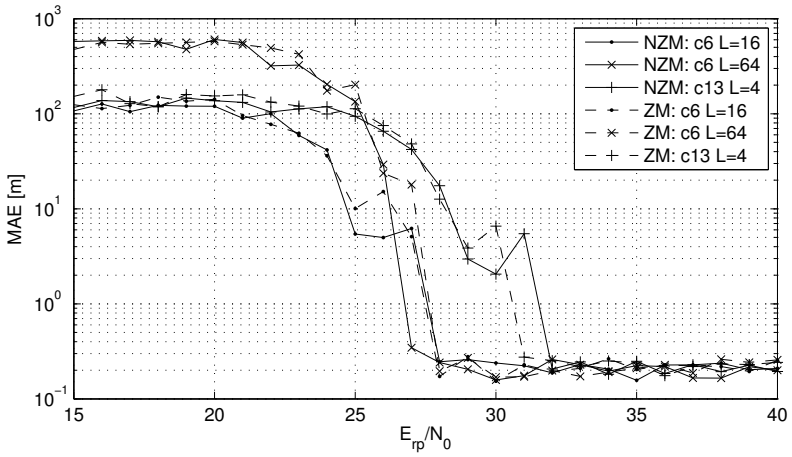

Figure 4.11 Mean Absolute Error (MAE) for ranging in the industrial LOS environment

channel energy. This makes the WP defined by the input SNR E_{rp}/N_0 dependent on the channel itself. Furthermore, the working point is dependent on the system parameters, which leads to no unique WP. Thus, $\mathrm{WP}_{\mathrm{LSNR}}$ is chosen as WP for the rest of the work.

Figure 4.11 shows the mean absolute error (MAE) for the specific codes using the two despreading codes. Again the optimal threshold per SNR is chosen to show the best possible performance. The error is for low SNRs uniformly distributed over the whole signal, where the larger error of c6 with $L = 64$ occurs from the longer preamble. Then the error is decreasing as the LOS component can be detected, but sometimes again noise samples are detected. The accuracy at high SNRs is defined by T_I and the pulse bandwidth B and all codes achieve an MAE ≈ 20 cm. Again the non-coherent combining loss of the c13 code can be observed in comparison to the c6 codes, where the performance of the c6 codes is again similar.

In contrast to [59], these results have been achieved by ranging on the amplitude not on the absolute value of the energy detector output. The work in [59] shows much more multipath dependency of $\tilde{\mathbf{c}}_{\mathrm{ZM}}$ especially for the long preamble symbols with $L = 4$. Thus, it is strongly recommended to apply the ranging on the amplitude of the energy detector output.

4.5 Summary

The energy detector has been analyzed for ranging with the IEEE 802.15.4a UWB air interface. A statistical model has been presented and the non-linear signal terms have been analyzed with respect to specific system parameters. Two despreading codes have been analyzed. The first one shows perfect crosscorrelation properties and the other one shows a zero-mean noise floor. Measured channel impulse responses of an industrial LOS environment were used to analyze the statistical model and the effect of the specific system parameters. Both despreading codes perform very similar within the experimental environment. The working point has been determined and the analysis shows that the linear noise term is negligible up to this point. Furthermore, the preamble code with a symbol length of 31 outperforms the one with 127 in the sense of energy efficiency and a spreading factor of 16 seems to

be appropriate in this multipath intensive environment. A mean absolute error (MAE) of 20 cm is achieved by all code combinations with low-complexity threshold-based ranging at high SNR.

5

Maximum Operating Distance Estimation for Ranging in IEEE 802.15.4a

In this section, the impact of system parameters of the IEEE 802.15.4a standard is studied in a signal-to-noise ratio (SNR) analysis for coherent receivers and energy detectors. The maximum allowed transmit power is analyzed according to the regulations of the Federal Communication Commission (FCC) [5] and the Conférence Européenne des Postes et Télécommunications (CEPT) [31], based on the results in [12]. The system performance is evaluated with respect to the maximum operating distance and the maximum allowed pathloss for the specific preambles and the 4a-channels. Especially the effects of preamble lengths, pulse repetition frequencies, pulse bandwidths and carrier frequencies are studied. Finally a complexity analysis of the coherent receiver and the energy detector is performed, comparing the processing effort for both receivers with respect to the system parameters. This analysis shows the best system settings for maximizing the allowed transmit energy and the operating distance.

The coherent receiver for ranging is shown in Figure 5.1. The difference to the coherent receiver shown in Figure 3.3 is that the input filters are directly matched to the pulse shape and the normalization by M_1 is not applied to the estimated channel response. The ranging is directly based on the magnitude of the estimated channel response. The signal model and the statistical analysis are shown in Appendix C. The signal model of Section 3 is still applicable with slight changes.

The major difference between the coherent receiver and the energy detector is the down-conversion. The coherent receiver applies a carrier based down-conversion, while the energy detector uses a squaring device with integration (see Figure 4.1). Thus, the coherent receiver needs high sampling rates according to the Nyquist theorem ($1/T \geq B$) with two sampling devices, one for the real and the other one for the imaginary part of the complex baseband signal. In other words, a higher bandwidth B requires higher sampling rates, which is not needed for the energy detector. Furthermore, the

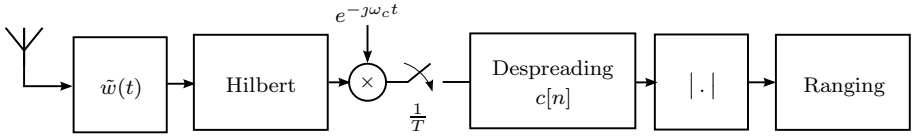

Figure 5.1 Coherent Receiver (cf. [57], © [2010] IEEE)

synchronization with the carrier frequency and phase is needed, which is a tough task as the pulses are hided in the noise floor. Due to these two problems, it is safe to assume that the coherent receiver is a high-complexity solution.

The chapter is organized as follows: Section 5.1 presents the SNR analysis and the definition of the performance metric. The FCC and CEPT regulations are discussed in Section 5.2 and the link budget is introduced in Section 5.3. This is followed by performance analysis and a summary in Sections 5.4 and 5.5.

5.1 SNR Analysis and Maximum Operating Distance Estimation

The goal of a ranging system is to find the line-of-sight (LOS) component in the channel response, as the detection of a reflected component may lead to very large ranging errors. The SNR of the LOS component (LSNR) correlates very well with the ranging performance (see Section 4.4.3), thus it is used to define the working point of the receivers. It is defined as

$$\mathrm{LSNR} := \frac{|y_s[n_{\mathrm{LOS}}]|^2}{\mathrm{var}\Big\{\hat{h}[n]\Big\}} \tag{5.1}$$

where $y_s[n_{\mathrm{LOS}}]$ is the desired signal part at sample n_{LOS} of the channel response, containing the LOS component, and $\mathrm{var}\{\hat{\mathrm{h}}[\mathrm{n}]\}$ is the noise variance of $\hat{h}[n]$. This section shows the relation between receiver input SNR—the energy of the despread LOS component related to the noise spectral density E_{LOS}/N_0—and LSNR. $E_{\mathrm{LOS}} = M_1 E^{(1)}_{\mathrm{LOS}}$, where $E^{(1)}_{\mathrm{LOS}}$ is the received energy for the LOS component of a single pulse.

5.1.1 Coherent Receiver

If only the LOS component is taken into account, $h[n]$ simplifies to $h_{\mathrm{LOS}}[n]{=}\sqrt{E^{(1)}_{\mathrm{LOS}}}w[n]{*}w[n]e^{j\varphi}$. Equation (C.5) simplifies to

$$\begin{aligned}\hat{h}_{\mathrm{LOS}}[n] =& M_1\sqrt{E^{(1)}_{\mathrm{LOS}}}\phi_w[n]e^{j\varphi} + \sum_{m=0}^{M-1} c_m \nu_{\mathrm{LP}}[n + mLN_{\mathrm{chip}}] \\ =& y_s[n] + y_\nu[n]\end{aligned} \tag{5.2}$$

where $\phi_w[n]$ is the autocorrelation of $w[n]$, $y_s[n]$ is the signal part and $y_\nu[n]$ is the noise part of the receiver output signal. The first and second order statistics at n_{LOS} are needed to obtain LSNR. It follows $\phi_w[n_{\mathrm{LOS}}] = \phi_w[0] = 1$ as $w(t)$ is energy normalized.

The expected value of the despread signal power is given by

$$\mathrm{E}\big\{|y_s[n_{\mathrm{LOS}}]|^2\big\} = E^{(1)}_{\mathrm{LOS}} M_1^2 = E_{\mathrm{LOS}} M_1 \tag{5.3}$$

and the variance of $\hat{h}_{\mathrm{LOS}}[n]$ is defined by (see C.8)

$$\mathrm{var}\Big\{\hat{h}_{\mathrm{LOS}}[n]\Big\} = \mathrm{var}\Big\{\hat{h}[n]\Big\} = N_0 M_1. \tag{5.4}$$

5.1.2 Energy Detector

A statistical analysis of the energy detector for ranging in IEEE 802.15.4a has been given in Chapter 4, which also included IPI. The current analysis is based on the LOS component and the despreading code with the perfect circular autocorrelation properties, $\mathbf{c}_{\mathrm{NZM}}$, is used. Thus it is sufficient to consider the IPI-free case, which is discussed in Appendix D.3. The final results are summarized below.

The expected value of the squared signal-by-signal term is given by (see Appendix D.3 (D.10))

$$\mathrm{E}\{y_{ss}^2[n_{\mathrm{LOS}}]\} \approx E_{\mathrm{LOS}}^2. \tag{5.5}$$

This approximation becomes exact for $T_I \geq T_p$, where T_p is the pulse length, assuming that the LOS signal falls in the integration interval. The variance of the signal-by-noise term is given by (see (D.16))

$$\mathrm{var}\{y_{s\nu}[n_{\mathrm{LOS}}]\} \approx 2E_{\mathrm{LOS}}N_0 \tag{5.6}$$

where it is observable that this term depends on the received signal energy. The variance of the noise-by-noise term is given by (see Equation (4.21))

$$\mathrm{var}\{y_{\nu\nu}[n]\} = \frac{N_0^2}{2} N_{\mathrm{synch}} N_s T_I W_{\mathrm{RRC}} \tag{5.7}$$

where W_{RRC} is an equivalent bandwidth defined as $W_{\mathrm{RRC}} = \int_{-T_{\tilde{w}}}^{T_{\tilde{w}}} \phi_{\tilde{w}}^2(\mu) d\mu$. A comparison to the coherent receiver shows that this noise term is proportional to N_0^2, while the noise term of the coherent receiver is linearly dependend on N_0 (see (5.4)).

5.1.3 Input-to-Output SNR Relation

Using (5.1) and (5.4), the Input-to-Output SNR relation is given for the coherent receiver by

$$\mathrm{LSNR}_{\mathrm{CR}} = \frac{|y_s[n_{\mathrm{LOS}}]|^2}{\mathrm{E}\{|y_\nu[n]|^2\}} = \frac{E_{\mathrm{LOS}}}{N_0}\,. \tag{5.8}$$

For the energy detector the relation is obtained from (5.1), (5.6), and (5.7) and is given by

$$\mathrm{LSNR}_{\mathrm{ED}} = \frac{2\left(\frac{E_{\mathrm{LOS}}}{N_0}\right)^2}{4\frac{E_{\mathrm{LOS}}}{N_0} + N_s N_{\mathrm{sync}} T_I W_{\mathrm{RRC}}} \tag{5.9}$$

The first term of the denominator corresponds to the linear and the second to the quadratic noise term. The quadratic noise term depends on the receiver parameters, which can be combined to the noise dimensionality ND=$N_s\, N_{\mathrm{sync}}\, T_I\, W_{\mathrm{RRC}}$ [14] (see Section 4.4.2).

Figure 5.2 shows the relation of input SNR, E_{LOS}/N_0, to the output SNR, LSNR, based on (5.8) and (5.9). In contrast to Figure 4.9, this figure also contains the noise characteristics of coherent receiver. As observeable from (5.8), the LSNR for the coherent receiver depends only on the transmitted energy. In other words, it does not matter if this energy is transmitted in a single pulse or in a sequence of pulses, while the system parameters are very important for the performance of the energy detector. This is seen from the noise dimensionality in (5.9).

Figure 5.3 shows the working point (WP) simulations for the coherent receiver and the energy detector. The probability for an absolute error (AE) less 1 m, $P(AE < 1m)$, using the optimum threshold c per SNR value and the NZM code is shown. In contrast to the working point simulations

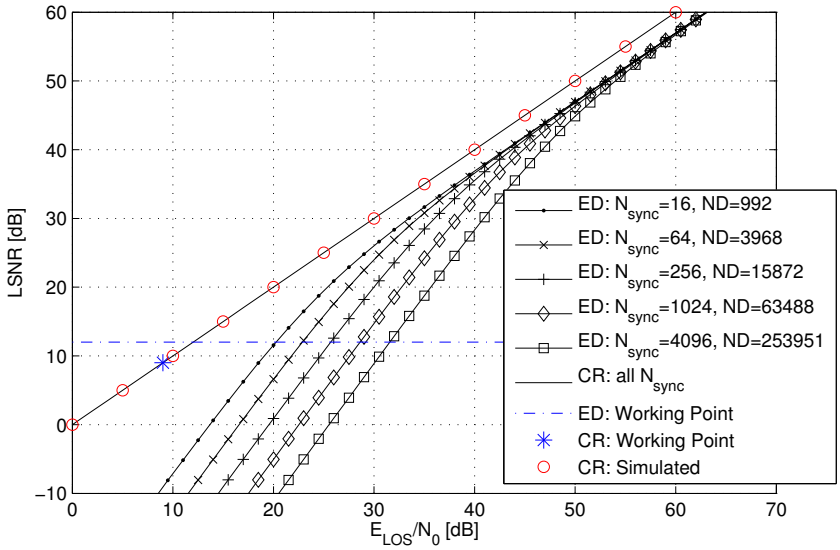

Figure 5.2 Relation between input SNR (E_{LOS}/N_0) and output SNR (LSNR) with respect to the noise dimensionality ND $= N_s\, N_{\mathrm{sync}}\, T_I\, W_{\mathrm{RRC}}$ for the energy detector (ED) and the coherent receiver (CR). The fixed parameters are $N_s = 31$, $T_I = 2.0032$ ns, and $W_{\mathrm{RRC}} = 1$ GHz. ([57], © [2010] IEEE)

of Figure 4.10, only the pulse shape is used without any multipath channel, which is usually called additive white Gaussian noise (AWGN) channel. This is the ideal case for the detection of the LOS component. The working point is defined at 80% $P(AE < 1m)$. First, it can be seen that the working point of the energy detector defined by LSNR ($\mathrm{WP}_{\mathrm{LSNR}}$) does not change for different values of N_{synch}, while the working point defined by E_{LOS}/N_0 ($\mathrm{WP}_{E_{\mathrm{LOS}}/N_0}$) changes due to the non-coherent combining loss. A comparison to Figure 4.10 shows that $\mathrm{WP}_{E_{\mathrm{LOS}}/N_0}$ changes also with the ratio of the LOS component and the total energy of the channel response E_{LOS}. Thus, the definition of the working point is only useful for LSNR. As already known from (5.8), both working points are the same for the coherent receiver. Anyway, $\mathrm{WP}_{\mathrm{LSNR}}$ is taken as the working point in the rest of the work, which is +9 dB for the coherent receiver and +12 dB for the energy detector. The discrepancy occurs due to the different probability distributions of the receiver outputs. The noise of the energy detector after despreading is Gaussian distributed, while the coherent receiver shows Rayleigh distributed output samples. For the 4a-standard, the coherent receiver shows a gain in the working point from 11 to 21 dB in comparison to the energy detector (see Figure 5.2).

5.1.4 Maximum Operating Distance Estimation

As N_0 is constant in the scenario, E_{LOS}/N_0 for the maximum operating distance $d_{\max}$ is obtained from the well-known pathloss model

$$\frac{E_{\mathrm{LOS}}}{N_0}(d_{\max}, f_c)_{\mathrm{dB}} = \frac{E_{\mathrm{LOS}}}{N_0}(d_0, f_c)_{\mathrm{dB}} - 10\eta \log\left(\frac{d_{\max}}{d_0}\right) \tag{5.10}$$

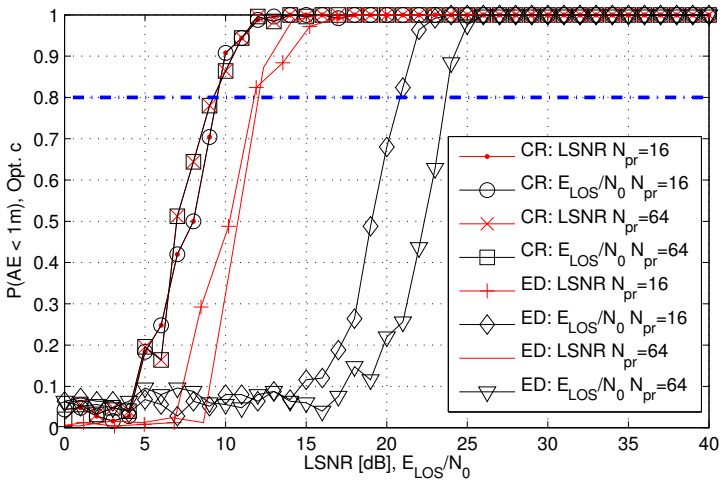

Figure 5.3 Working point simulations using only LOS component.

where η is the pathloss exponent and d_0 is a reference distance. E_{LOS}/N_0 depends on the free-space pathloss (see Table 5.1), which further depends on the carrier frequency f_c (see (5.17)). The maximum operating distance for the coherent receiver is obtained from (5.8) and (5.10):

$$d_{\max} = \left(\frac{\frac{E_{\mathrm{LOS}}}{N_0}(1\mathrm{m}, f_c)}{\frac{E_{\mathrm{LOS}}}{N_0}(d_{\max}, f_c)} \right)^{1/\eta} = \left(\frac{\frac{E_{\mathrm{LOS}}}{N_0}(1\mathrm{m}, f_c)}{\mathrm{LSNR}_{\mathrm{WP}}} \right)^{1/\eta} \tag{5.11}$$

where the reference distance is assumed to be 1 m. For the energy detector follows

$$d_{\max} = \left(\frac{\frac{E_{\mathrm{LOS}}}{N_0}(1\mathrm{m}, f_c)}{\mathrm{LSNR}_{\mathrm{WP}} + \sqrt{\mathrm{LSNR}_{\mathrm{WP}} \left(\mathrm{LSNR}_{\mathrm{WP}} + \mathrm{ND}/2\right)}} \right)^{1/\eta} \tag{5.12}$$

using (5.9) and (5.10). The derivation is shown in Appendix D.4.

5.1.5 Maximum Allowed Pathloss PL_{max}

A more general look at the achieveable range is given by the maximum allowed pathloss $\mathrm{PL}_{\max}$, which is independent of the channel model, fading margins, or implementation losses. Equation (5.8) can be rewritten to obtain $\mathrm{PL}_{\max}$ for the coherent receiver

$$\mathrm{PL}_{\max,\mathrm{dB}} = \left(\frac{E_{\mathrm{pr}}}{N_0}\right)_{\mathrm{dB}} - \frac{\tilde{E}_{\mathrm{LOS}}}{N_0}(d_{\max}, f_c)_{\mathrm{dB}} = \left(\frac{E_{\mathrm{pr}}}{N_0}\right)_{\mathrm{dB}} - \mathrm{LSNR}_{\mathrm{WP,dB}} \tag{5.13}$$

where E_{pr} is the transmitted preamble energy and $\tilde{E}_{\mathrm{LOS}}$ is the energy of the received LOS component at 1 m, which does not take fading margins or implementation losses into account (see Table 5.1). For the energy detector follows, using (5.9) and (5.10),

$$\mathrm{PL}_{\max,\mathrm{dB}} = \left(\frac{E_{\mathrm{pr}}}{N_0}\right)_{\mathrm{dB}} - 10\log\left(\mathrm{LSNR}_{\mathrm{WP}} + \sqrt{\mathrm{LSNR}_{\mathrm{WP}}\left(\mathrm{LSNR}_{\mathrm{WP}} + \mathrm{ND}/2\right)}\right). \tag{5.14}$$

To take also the carrier frequencies f_c into account, only the distance dependent part of the pathloss model $\mathrm{PL}^{(d)}$ can be taken as receiver SNR. Thus, the pathloss model can be rewritten to obtain $\mathrm{PL}^{(d)}_{\max}$

for the coherent receiver

$$\begin{aligned} \mathrm{PL}^{(d)}_{\mathrm{max,dB}}(f_c) =& \frac{\tilde{E}_{\mathrm{LOS}}}{N_0}(1\mathrm{m}, f_c)_{\mathrm{dB}} - \frac{\tilde{E}_{\mathrm{LOS}}}{N_0}(d_{\max}, f_c)_{\mathrm{dB}} \\ =& \left(\frac{E_{\mathrm{pr}}}{N_0}\right)_{\mathrm{dB}} - \mathrm{PL}_{\mathrm{FS}}(1\mathrm{m}, f_c)_{\mathrm{dB}} - \mathrm{LSNR}_{\mathrm{WP,dB}} \end{aligned} \tag{5.15}$$

with

$$\frac{\tilde{E}_{\mathrm{LOS}}}{N_0}(1\mathrm{m}, f_c)_{\mathrm{dB}} = \left(\frac{E_{\mathrm{pr}}}{N_0}\right)_{\mathrm{dB}} - \mathrm{PL}_{\mathrm{FS}}(1\mathrm{m}, f_c)_{\mathrm{dB}}\,. \tag{5.16}$$

The free space loss $\mathrm{PL}_{\mathrm{FS}}$ defined by [47]

$$\mathrm{PL}_{\mathrm{FS}}(d_0, f_c) = \frac{(4\pi)^2 d_0^2 f_c^2}{\zeta^2}, \tag{5.17}$$

where ζ is the speed of the light and the ratio $\zeta/f_c = \lambda_c$, in which λ_c is the wavelength of the carrier frequency.

It follows for the energy detector with (5.9) and (5.10) that

$$\mathrm{PL}^{(d)}_{\mathrm{max,dB}}(f_c) = \frac{\tilde{E}_{\mathrm{LOS}}}{N_0}(1\mathrm{m}, f_c)_{\mathrm{dB}} - 10\log\left(\mathrm{LSNR}_{\mathrm{WP}} + \sqrt{\mathrm{LSNR}_{\mathrm{WP}}\left(\mathrm{LSNR}_{\mathrm{WP}} + \mathrm{ND}/2\right)}\right)\,. \tag{5.18}$$

$E_{\mathrm{LOS}}/N_0(1\mathrm{m}, f_c)$ and $\tilde{E}_{\mathrm{LOS}}/N_0(1\mathrm{m}, f_c)$ are defined by E_{pr} (see Section 5.2) and the link budget (see Section 5.3).

5.2 FCC Regulations

In this section the maximum allowed transmit power is calculated w.r.t. the FCC regulations [5]. In principle, the same regulations have been adopted by the CEPT in Europe for the band between 6 and 8.5 GHz [31]. In the band between 3.1 and 4.8 GHz the CEPT requires detect and avoid (DAA) or low duty cycle (LDC) mitigation, but this does not influence this analysis. This analysis is based on results of [12].

The FCC constraints essentially consist of an average and a peak power limit. In any band of bandwidth B_{av}=1 MHz, the average transmit power is limited to $P^{\mathrm{FCC}}_{\mathrm{av}}$= − 41.3 dBm for an averaging window of T_{av}=1 ms. The peak power within the bandwidth B_{pk}=50 MHz is restricted to $P^{\mathrm{FCC}}_{\mathrm{pk}}$=0 dBm. Both peak and average transmit power are defined as the equivalent isotropically radiated power (EIRP). Further information about world wide regulations have been given in Section 2.2.

The 802.15.4a preamble is a sequence of non-uniformly spaced pulses whose polarities are chosen pseudo-randomly by the codes. According to [12], its average and peak power is determined by the effective pulse repetition frequency (ERF) and the peak repetition frequency (PRF) respectively. The pulse energy spectral density (ESD) for the average power limit is given by

$$\mathrm{ESD}_{\mathrm{av}} = E_{\mathrm{p,av}}|W(f_c)|^2 = \frac{P^{\mathrm{FCC}}_{\mathrm{av}}}{2B_{\mathrm{av}}ERF} \quad \text{if } ERF \geq 1/T_{\mathrm{av}} \tag{5.19}$$

where $E_{\mathrm{p,av}}$ is the pulse energy limited by the average power limit and $W(f_c)$ is the spectrum of the normalized pulse $w(t)$ at the center frequency f_c. The ERF is defined as

$$ERF = \begin{cases} MRF\frac{T_{\mathrm{synch}}}{T_{\mathrm{av}}} = \frac{M_1}{T_{\mathrm{av}}} & T_{\mathrm{synch}} < T_{\mathrm{av}} \\ MRF & T_{\mathrm{synch}} \geq T_{\mathrm{av}} \end{cases} \tag{5.20}$$

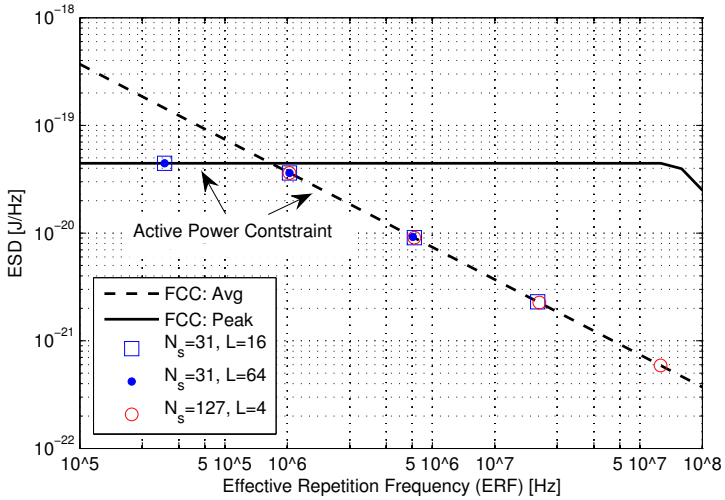

Figure 5.4 Allowed energy spectral density per pulse of the specific preamble symbols. The values are given for $N_{\text{sync}} = [16, 64, 256, 1024, 4096]$ (from left to right, see Table 3.1 for the corresponding *ERF* values). (cf. [57], © [2010] IEEE)

where $M_1 = (N_s + 1)/2$ is the number of non-zero code elements. As the mean power is limited by the number of pulses within 1 ms ($N_{1\text{ms}}$) (see Table 3.1), equation (5.19) is limited to $ERF \geq 1/T_{\text{av}}$, which is usually given for IR-UWB systems.

The peak power limit is defined by the *PRF*, where the sequenced pulses within an observation window $1/B_{\text{pk}} = 20$ ns are added. The energy spectral density for the peak power limit ESD_{pk} is obtained by

$$\text{ESD}_{\text{pk}} = E_{\text{p,pk}}|W(f_c)|^2 = \begin{cases} \frac{P_{\text{pk}}^{\text{FCC}}}{9B_{\text{pk}}^2} & PRF \leq (3/2)B_{\text{pk}} \\ \frac{P_{\text{pk}}^{\text{FCC}}}{4PRF^2} & PRF \geq (3/2)B_{\text{pk}} \\ & \text{and } \; f' \in [-B_{\text{pk}}/2, B_{\text{pk}}/2] \end{cases} \tag{5.21}$$

where $E_{\text{p,pk}}$ is the pulse energy limited by the peak power limit and f' denotes the considered frequencies. At low *PRFs* only one pulse occurs in the observation window, while at high *PRFs* the pulses start overlapping within the window. Hence, the two cases have to be distinguished.

The maximum FCC compliant ESD of the pulse with respect to peak and average power are shown in Figure 5.4. To find the active ESD for a specific preamble, the smaller value between ESD_{pk} at *PRF* and ESD_{av} at *ERF* is considered. It can be observed that only the short preamble sequences with $N_s = 31$ with a spreading of $L = 16$ and $L = 64$ are peak power limited, where $ERF = 0.256$ MHz (see also Table 3.1).[1]

Assuming a pulse with rectangular spectrum, the energy per pulse is E_p=2BERP, where B is the pulse bandwidth. Thus, the achieveable preamble energy can be calculated, which is shown in Figure 5.5. The long preamble codes with $N_s = 127$ are always restricted by the average power limit due to the high pulse repetition rate and four times more pulses than the others. Thus increasing N_{sync} does not lead to an increased preamble energy up to 1024 since $T_{\text{synch}} \leq 1$ ms. $N_{\text{sync}} = 4096$ leads to an

[1] It is reported in [63], that the supply voltage in low-rate handheld CMOS systems limits the transmit power, thus the peak power limit can not be exploited for low supply voltages.

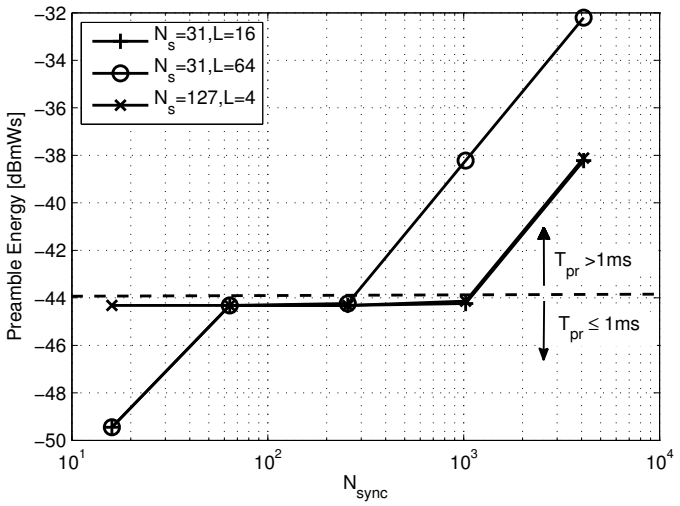

Figure 5.5 Achievable preamble energies. The dotted line shows the boundary for the mean power limit, which limits preambles with a length ≤ 1 ms. ([57], © [2010] IEEE)

improvement as $T_{\text{synch}} > 4$ ms, which means the preamble is more than four times longer than T_{av}. At $N_{\text{sync}} = 16$, the short preamble codes are limited by the peak power limit and the long preamble codes are limited by the average power limit. Both limits allow approx. the same ESD per pulse (see Figure 5.4). The short preamble codes with spreading 64 imply a four times longer preamble in contrast to the others, which means also a four times longer exceeding of the averaging window, thus a gain of 6 dB can be achieved.

5.3 Link Budget

As mentioned before, $E_{\text{LOS}}/N_0(1\text{m}, f_c)$ is the input SNR of the receiver at 1 m, which depends on the link budget. Table 5.1 shows an example link budget calculation for Channel (Ch) 3 of the 802.15.4a

Table 5.1 Example link budget for maximum operating distance estimation
$N_{\text{sync}} = 1024$, $N_s = 31$, $L = 16$, $f_c = 4.4928$ GHz, and $B = 499.2$ MHz.

Parameter		**Values**
Pulse Energy (incl. G_{TX})	E_p	-116.38 dBWs
Preamble Energy	E_{pr}	-74.31 dBWs
Free space loss @ 1 meter	$\text{PL}_{\text{FS}}(f_c)$	45.5 dB
Receiver antenna gain	G_{RX}	0 dBi
Received LOS component energy	$\tilde{E}_{\text{LOS}}(f_c)$	-119.81 dBWs
Noise Spectral Density	N_0	-198.93 dBW/Hz
Implementation Loss	L_{imp}	4 dB
Fading Margin	M_F	3 dB
Receiver Input SNR	$E_{\text{LOS}}/N_0(1\text{m}, f_c)$	72.12 dB

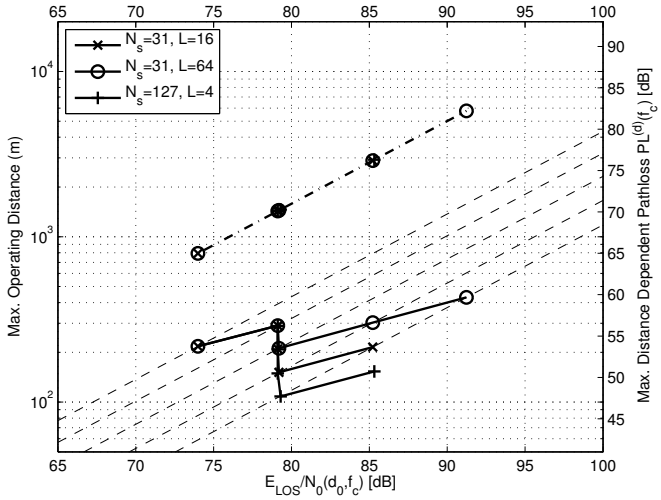

Figure 5.6 Code sequence analysis on the maximum operating distance and the maximum allowed pathloss. The solid lines correspond to the energy detector, the dashed-dotted lines belong to the coherent receiver and the dashed lines indicate constant noise dimensionality for the energy detector. The values are given for $N_{\text{sync}} = [16, 64, 256, 1024, 4096]$ (from left to right). (cf. [57], © [2010] IEEE)

standard, using $N_{\text{sync}} = 1024$, $N_s = 31$, $L = 16$, $f_c = 4.4928$ GHz, and a bandwidth of 499.2 MHz. In that case the average power limit of the FCC regulations applies and E_p is calculated from (5.19), including the transmit antenna gain $G_{\text{TX}} = 0$ dB. E_p is limited for 1006 sequences due to averaging over 1 ms (see Table 3.1). The preamble energy $E_{\text{pr}} = E_p M_1$. The free space loss PL_{FS} at 1 m is given by 45.5 dB using (5.17). Assuming the input structure of the receiver is linear, the noise spectral density is given by $N_0 = \kappa T_0 F$ [64], where the Boltzmann constant $\kappa = 1.38\,10^{-23}$ [J/K], the temperature of the environment is $T_0 = 293$ K, and the noise figure of the receiver input structure is $F = 5$ dB (cf. [65]). Implementation losses of 4 dB^2 and a LOS fading margin of 3 dB are assumed. Thus, $E_{\text{LOS}}/N_0(1\text{m}, f_c)$ is obtained and can be used to calculate the maximum operating range according to (5.10) and (5.12).

5.4 Performance Analysis

The maximum operating distance and the maximum acceptable pathloss are analyzed in this section. The maximum operating distance is based on the free space link budget, because the LOS component is needed for accurate ranging. The maximum acceptable pathloss is shown as a more general performance metric, which allows the implementer to analyze the effect of specific channel models, e.g. NLOS scenarios, or specific system parameters, e.g. lower noise figures.

5.4.1 Effect of Codes

Figure 5.6 shows the maximum operating distance $d_{\max}$ and the maximum allowed distance dependent pathloss $\mathrm{PL}_{\max}^{(d)}(f_c)$ with respect to the preamble sequences. Both values of the coherent receiver are directly proportional to E_{LOS}/N_0, which means that the same operating distance can be achieved for a single pulse or a sequence of pulses if the SNR is fixed (see (5.11)). By contrast, the ED suffers strongly from non-coherent combining losses, in which the noise dimensionality including the number of transmitted pulses is important for the final performance (see (5.12)). In the overall performance there is a big gap between the CR and the ED. The CR achieves a maximum operating distance up to several thousand meters and the ED achieves only several hundred meters. However, an operating distance of several hundred meters is usually sufficient for (low-complexity) indoor localization systems and sensor networks.

As expected from Section 5.2, the best performance is achieved by the short preamble codes with long spreading ($L = 64$) due to the highest transmitted energy. For them, a maximum operating distance of approximately 6000 m ($\mathrm{PL}_{\max}^{(d)}\approx$82 dB) is achieved by the CR and $\approx$ 430 m ($\mathrm{PL}_{\max}^{(d)}\approx$60 dB) is achieved by the ED. The CR reaches approx. half that distance ($\approx$3000 m; $\mathrm{PL}_{\max}^{(d)}\approx$76 dB) for the other two codes.

As mentioned before, the energy detector shows a more specific behavior, which is discussed in detail in the rest of this paragraph. As observable, increasing of N_{sync} does not necessarily lead to a better performance because of the non-coherent combining loss. Thus, a performance degradation is seen at around $E_{\mathrm{LOS}}/N_0(d_0, f_c)\approx$79 dB for increasing numbers of transmitted pulses due to constant transmitted energy (cf. Figure 5.5). This effect also significantly harms the performance of the long preamble codes ($N_s = 127$) and leads to the lowest achieveable performance. The performance with short preamble sequences ($N_s = 31$) and spreading $L = 16$ is best at $N_{\mathrm{sync}} = 64$ and with the long preamble sequences at $N_{\mathrm{sync}} = 16$, where a distance of approx. 300 m ($\mathrm{PL}_{\max}^{(d)}\approx$56 dB) is achieved. The preamble sequences with $L = 64$ show a local optimum for $N_{\mathrm{sync}} = 64$ with the same performance as the others. This performance is also reached for a much longer preamble with $N_{\mathrm{sync}} = 1024$ repetitions and slightly exceeded with $N_{\mathrm{sync}} = 4096$ despite of increased preamble energy (cf. Figure 5.5), much longer signals (see Table 3.1), and much higher processing effort (see Section 5.4.3). From these results, it seems inefficient for EDs to choose extremely long preambles with $N_{\mathrm{sync}} = 1024$ or 4096.

The IEEE 802.15.4a standard also defines different channels with specific bandwidths and carrier frequencies. An analysis of the various channels is given in the next section.

5.4.2 Effect of Channels

IEEE 802.15.4a defines 16 channels in three frequency bands, the Sub-Giga-Hertz Band(<1 GHz), the Low-Band ($3.2 - 4.8$ GHz), and the High-Band ($5.9 - 10.3$ GHz). The channel bandwidths B range from 499.2 to 1354.97 MHz. As mentioned in Section 5.2, the CEPT only allows the usage of the frequency bands $3.1 - 4.8$ and $6 - 8.5$ GHz for UWB, where for LDC the signals have to be shorter than 5 ms. Thus, the short preamble symbol with spreading $L = 64$ and $N_{\mathrm{sync}} = 4096$ is not allowed for LDC transmission. It is well-known that a higher carrier frequency f_c causes higher losses and thus less received signal strength according to Friis' equation [46]. A larger bandwidth leads to a higher allowed transmit power (see Section 5.2). To evaluate this trade-off, six channels are analyzed in this chapter using the short preamble codes with $L = 64$.

[2]This value was suggested by DecaWave (www.decawave.com)

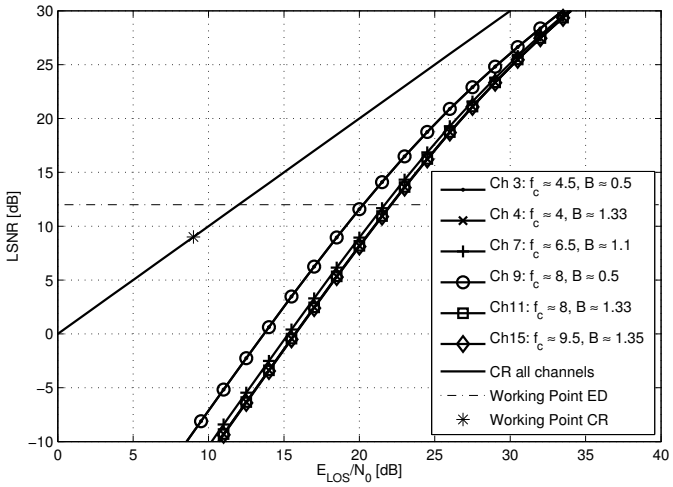

Figure 5.7 Relation between input SNR E_{LOS}/N_0 and output SNR LSNR for the short preamble codes with a spreading $L = 64$ and $N_{\mathrm{sync}} = 16$ with respect to the IEEE 802.15.4a channels. The channel parameters in the legend are in GHz. ([57], © [2010] IEEE)

Figure 5.7 shows the relation between input and output SNR for the specific channels. As seen from (5.8), the CR is again independent of the channel bandwidths. For the ED, variations occur due to the different bandwidths. It can be observed that the channels with the large bandwidths need up to 1.5 dB more E_{LOS}/N_0 in the working point to achieve the same LSNR.

Figure 5.8 shows the allowed preamble energies for the specific channels. The larger bandwidths allow an energy gain of up to 4 dB, which is sufficient to compensate the SNR loss of the ED shown in Figure 5.7. This is also seen from (5.9), where the equivalent bandwidth W_{RRC} influences LSNR linearly and the additional energy improves the SNR quadratically in the working point. Thus, a gain of up to 2.5 dB can be achieved. For the CR, the additional energy will directly improve the performance.

Figure 5.9(a) shows the maximum operating distance and the maximum allowed pathloss for the specific channels with respect to the receiver input SNR at d_0. It can be observed that the Low-Band channels Ch 3 and Ch 4 show better performance than the High-Band channels due to lower free-space losses. Half the operating range is obtained when f_c is increased from 4 to 8 GHz. It can be seen that a shift in the carrier frequency leads to a change of E_{LOS}/N_0, but it does not change the relation of input to output SNR because the ND is not changed (compare Ch 3 and Ch 9). A shift of the bandwidth changes this relation, which is observable for Ch 9 and Ch 11. A doubled operating range can be achieved with the CR when the bandwidth is increased from 500 MHz to 1.33 GHz, while only the 1.3-fold distance is achieved with the ED. The best performance is achieved at Ch 4, which has a low carrier frequency $f_c \approx 4$ GHz and a large bandwidth of $B \approx 1.33$ GHz. It reaches $d_{\max} \approx 10620$ m ($\mathrm{PL}_{\max}^{(d)} \approx 88$ dB) for the CR and $d_{\max} \approx 620$ m for the ED ($\mathrm{PL}_{\max}^{(d)} \approx 63$ dB). The mandatory Ch 3 of the Low-Band shows a significantly better performance in comparison to the mandatory channel in the High-Band Ch 9 due to the lower carrier frequency.

Figure 5.9(b) shows the effect of the transmitted preamble energy to noise ratio E_{pr}/N_0 on the

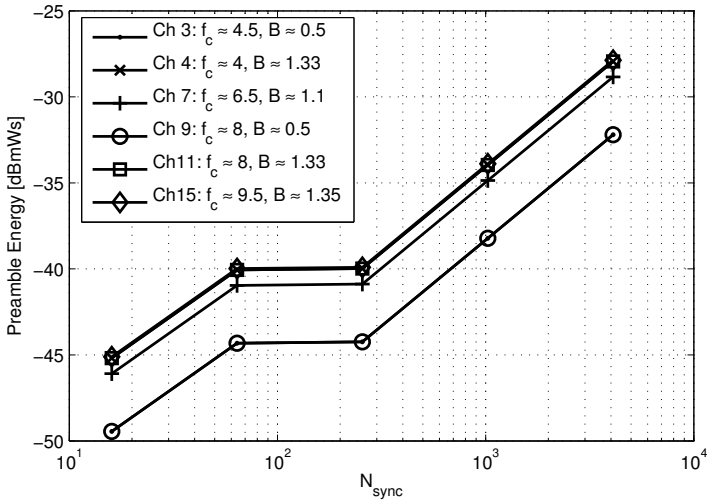

Figure 5.8 Allowed preamble energy for the specific IEEE802.15.4a channels.

estimated distance. It can be observed, that the same transmitted energy will lead to different maximum operating distances for different carrier frequencies (compare Ch 3 and Ch 9), which can be observed for both receiver architectures in the vertical axis. The specific bandwidths lead to a shift of the transmit energy in the horizontal axis. The specific transmit energies define the maximum allowed pathloss, which is independent of the carrier frequencies and is shown in Figure 5.9(c). $\mathrm{PL}_{\max}$ varies from 98 dB to 108 dB for the energy detector and from 110 to 132 dB for the coherent receiver.

5.4.3 Receiver Complexity Analysis

The digital processing effort for estimating a channel response is a good measure to evaluate the receiver complexity for ranging.

The despreading is defined in Appendix C and in Section 4.2 for the CR and the ED respectively. As $c_m \in \{-1, 0, 1\}$, the despreading consists only of additions and subtractions. Thus, the coherent receiver needs $O_{\mathrm{CR}} = 2M_1 = (N_s+1)N_{\mathrm{sync}}$ operations per sample, because the zero coded elements are discarded and two sampling devices are needed for the complex baseband. A different despreading code is used for the energy detector, where the zero-code elements are set to -1. Thus, all code elements have to be taken into account and the number of operations is $O_{\mathrm{ED}} = M = N_s N_{\mathrm{sync}}$. Assuming that at least the full channel impulse response has to be estimated, a maximum access delay $\tau_{\max} = 100$ ns is used for the analysis. This covers residential areas, were a maximum excess delay of 70 ns has been reported [66]. Thus the number of operations for estimating the channel response is given by

$$O_{\mathrm{CIR}} = \begin{cases} (N_s+1)N_{\mathrm{sync}}\frac{\tau_{\max}}{T} = 2M_1\frac{\tau_{\max}}{T} & \mathrm{CR} \\ N_s N_{\mathrm{sync}}\frac{\tau_{\max}}{T_I} = M\frac{\tau_{\max}}{T_I} & \mathrm{ED}. \end{cases} \tag{5.22}$$

The coherent receiver works in complex baseband, which requires a sampling rate of $1/T \geq B$ for each of the two channels, while the ED has only one sampling device and T_I is limited to the

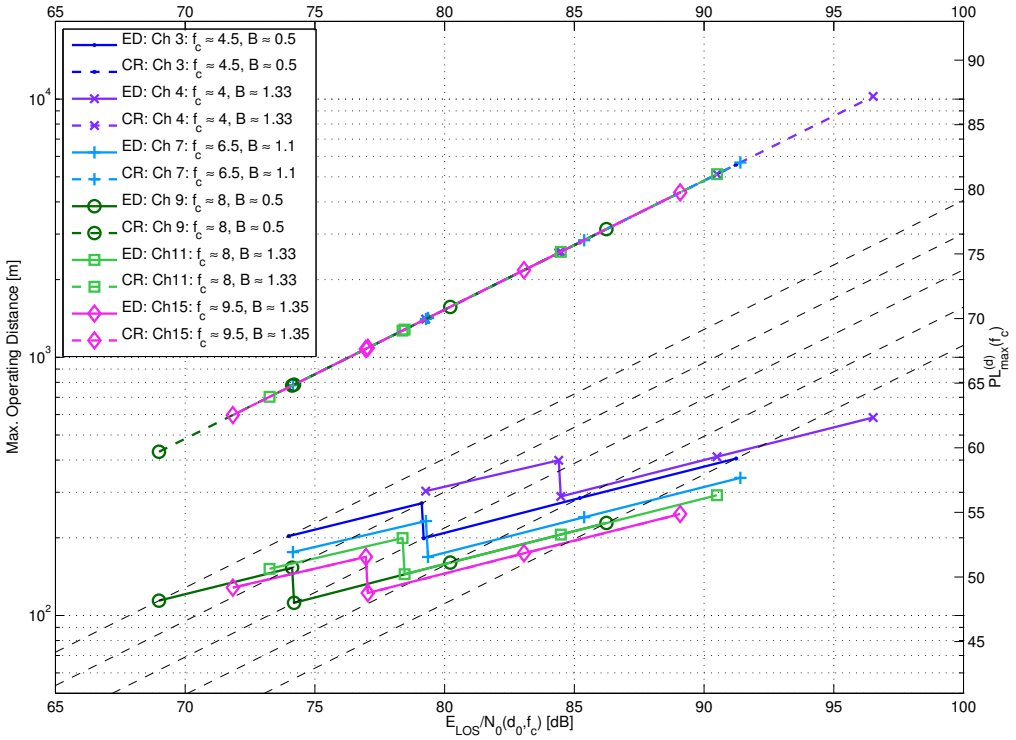

(a) (cf. [57], © [2010] IEEE)

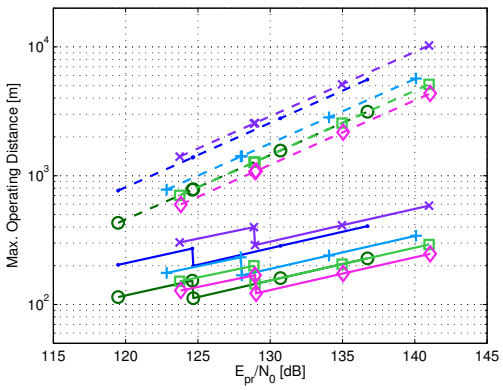

(b)

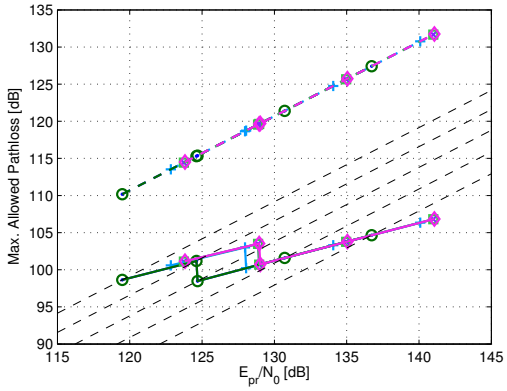

(c)

Figure 5.9 Performance analysis of the specific IEEE 802.15.4a channels. The dashed lines show the characteristic for a channel with $B = 499.2$ MHz with the ND of Figure 5.6. The values are given for $N_{\text{sync}} = [16, 64, 256, 1024, 4096]$ (from left to right). (a) shows the maximum operating distance and $\text{PL}_{\text{max}}^{(d)}(f_c)$ estimation related to the receiver input SNR at d_0, (b) shows the maximum operating distance related to the transmit SNR, and (c) shows the maximum allowed pathloss related to the transmit SNR.

Table 5.2 Complexity analysis

B				T_{synch}	$O_{\text{CIR}}\ \times 10^3$				
					ED $T_I =$			CR $T =$	
[MHz]	N_s	L	N_{sync}	[μs]	$T_{\text{chip}}/2$	T_{chip}	$2\,T_{\text{chip}}$	T_{chip}/k	k
499.2	31	16	64	63.6	198.1	99.0	49.5	102.2	1
499.2	31	64	64	254.4	198.1	99.0	49.5	102.2	1
499.2	127	4	64	65.1	811.5	405.7	202.9	408.9	1
1081.6	31	16	64	63.6	198.1	99.0	49.5	306.7	3
1081.6	31	64	64	254.4	198.1	99.0	49.5	306.7	3
1081.6	127	4	64	65.1	811.5	405.7	202.9	1226.8	3
1354.97	31	16	64	63.6	198.1	99.0	49.5	306.7	3
1354.97	31	64	64	254.4	198.1	99.0	49.5	306.7	3
1354.97	127	4	64	65.1	811.5	405.7	202.9	1226.8	3

application-defined accuracy of the ranging (see Section 4.1). For simple despreading, we choose $1/T = k/T_{\text{chip}} = \lceil BT_{\text{chip}} \rceil / T_{\text{chip}}$ for the CR.

The results of the complexity analysis are shown in Table 5.2. It can be observed that O_{CIR} can be reduced significantly by using longer integration times for the ED, which are independent of the pulse bandwidth. The gap between the ED and the CR is increasing for the higher bandwidths, but for $B = 500$ MHz the complexity is approximately the same for both receivers, as the same sampling rates can be applied. As (5.22) is independent of L, the short codes with $L = 64$ show the same number of operations as those with $L = 16$. The despreading is strongly dependent on the number of code elements, thus the long preamble codes lead to the most operations. The CR with $B = 1354.97$ GHz and the long preamble codes shows the highest complexity, where more than 1 million operations have to be performed to estimate one channel response. In contrast, the energy detector needs only a third of that when $T_I = T_{\text{chip}} \approx 2$ ns.

5.5 Summary

A coherent receiver and an energy detector have been studied for ranging in IEEE 802.15.4a, in the sense of maximum allowed transmit energy, maximum operating distance, and processing effort.

The maximum allowed transmit energy according to the FCC/CEPT regulations depends strongly on the parameters of the preamble. For most of the preamble code sequences the average power limit applies. A longer spreading of the preamble symbols leads to a performance gain, because a larger preamble energy is allowed. As the FCC/CEPT limits the power spectral density, a higher pulse bandwidth also yield a larger energy.

The maximum operating distance estimation is based on a link budget. It is shown that the coherent receiver is directly dependent on the receiver input SNR, while the energy detector depends strongly on the parameters of the preamble codes due to the non-coherent combining loss. It is shown that 64 preamble symbol repetitions are most efficient for the energy detector and the short preamble symbols are preferable due to lower non-coherent combining losses and less despreading effort. The low-frequency channels achieve longer ranges due to the lower pathloss. The mandatory low-frequency channel for example ($f_c = 4.5$ GHz) achieves almost twice the range in comparison to the mandatory

high-frequency channel ($f_c = 8$ GHz). A gain is also obtained for the high-bandwidth channels. Here the range is almost doubled for coherent receivers, while the energy detector reaches only a gain of 30 percent.

The highest processing effort in the digital receiver frontend has to be done for the despreading. The coherent and the non-coherent receiver show a similar number of operations, because approximately the same sampling rates are applied. However, the coherent receiver is limited to Nyquist sampling, thus larger bandwidths increase the processing effort, while the energy detector permits sub-Nyquist sampling. Furthermore, the coherent receiver needs two sampling devices and has to be synchronized with the carrier, which means that it is a high-complexity solution.

The low-complexity energy detector achieves maximum operating distances of several hundred meters, while the coherent receiver reaches distances up to several thousand meters in free space. Thus, both receiver architectures are appropriate approaches for real time locating systems and sensor networks.

6

UWB System-Level Simulator for Positioning and Tracking (U-SPOT)

Realistic simulation of Ultra-Wideband (UWB) positioning and tracking is a tough and challenging task. Lots of parameters have a significant impact on the final performance of the positioning system, such as parameters of the transmitted waveform, radio regulations, channel, receiver, ranging-, positioning-, and tracking-algorithm, and finally the geometric setup. Therefore, a realistic simulation framework is needed to develop and optimize UWB methods and algorithms.

This chapter presents a novel framework for realistic UWB positioning simulations, called UWB System-Level Simulator for Positioning and Tracking (U-SPOT). All stages of influence have been modeled carefully. While ray-tracing simulators focus on a given user defined scenario, our approach uses statistically defined environments. Random processes are used to select channel impulse responses from a measurement database, according to an algorithm which introduces realistic large and small-scale variability with space. In particular, line-of-sight (LOS) and non-LOS (NLOS) channels are used at a defined ratio. As an application example, this work investigates the localization capabilities of the IEEE 802.15.4a standard in mixed office LOS and NLOS environments. The performance of a least squares positioning algorithm, a standard Kalman filter and an extended Kalman filter is analyzed for a user-defined trajectory. The initialization of the Kalman filters and the handling of outliers is optimized using U-SPOT. The performance of a high-complexity coherent receiver and an energy detector is compared as well. Finally, the influence of NLOS links on the tracking performance is studied in detail.

Typically only parts of the UWB systems are studied, without investigation of the overall system performance. Current evaluations of UWB positioning simulators focus often on specific system parameters such as geometry [68]. Reference [69] analyze an overall system, but with focus on the hardware aspects of the positioning system. A completely different approach is followed in ray-tracing simulators [70, 71]: Realistic multipath propagation is obtained by simulating possible propagation paths. Drawbacks are the restriction of the scenario to the specified one, as well as the high computational effort. A hybrid approach has been chosen for the PARIS Simulation Framework [72, 73], in which deterministic ray-tracing is combined with stochastic modeling of the channel. This simulator is designed for research and development in ultra high frequency (UHF) RFID and includes detailed modeling of the RFID tag. It is able to handle (ultra)wideband signals [72–75]. Notably,

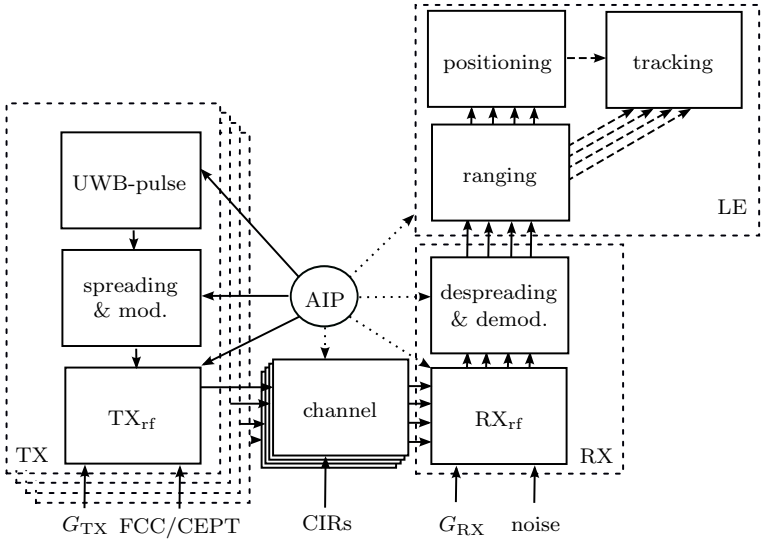

Figure 6.1 Architecture of a one-way ToA positioning system ([76], © [2010] IEEE)

also this simulator is restricted to a specific localization scenario. Our simulation framework uses measured channel impulse responses for realistic simulation with low computational effort. Channels are selected according to a statistical framework, thus the simulations are not limited to a specific scenario. The framework is highly appropriate for large-scale Monte Carlo simulations e.g. to tune system parameters for a given application and environment.

The rest of the chapter is organized as follows: Section 6.1 shows the overall layout of a ranging-based impulse-radio (IR) UWB positioning system and Section 6.2 describes the modular concept of our positioning simulator. Afterwards, Section 6.3 defines the simulation setup and explains the optimization of the algorithms. The simulator is evaluated by analyzing the tracking capabilities of Kalman filters with IEEE 802.15.4a in Section 6.4. Finally, in Section 6.5 we sum up our results.

6.1 Positioning System

Figure 6.1 shows the modular structure of a ranging-based IR-UWB positioning system. The air interface protocol (AIP) defines the transmission scheme (solid arrows) and thus also influences the channel and the receiver (RX) (dashed arrows). The location estimation block (LE) uses the estimated channel impulse responses as input signals, thus it does not directly depended on the AIP. On the other hand, the AIP defines which ranging and positioning method is applicable, e.g. two-way ranging, time-of-arrival (ToA) or time-difference of arrival (TDoA), etc. In this work, we focus on one-way ToA positioning with perfect synchronization.

First, the baseband pulse is generated in the transmitter (TX). Its bandwidth defines the achievable localization accuracy [27]. Second, the pulse is convolved with a standard-compliant code sequence in order to increase the transmit power and the signal-to-noise ratio (SNR). The radio frequency (RF)-frontend of the transmitter $\mathrm{TX_{rf}}$ contains an up-converter, an amplifier and a transmit antenna (G_{TX}), whose output power is calibrated to the RF-regulations. A detailed analysis of the FCC regulations

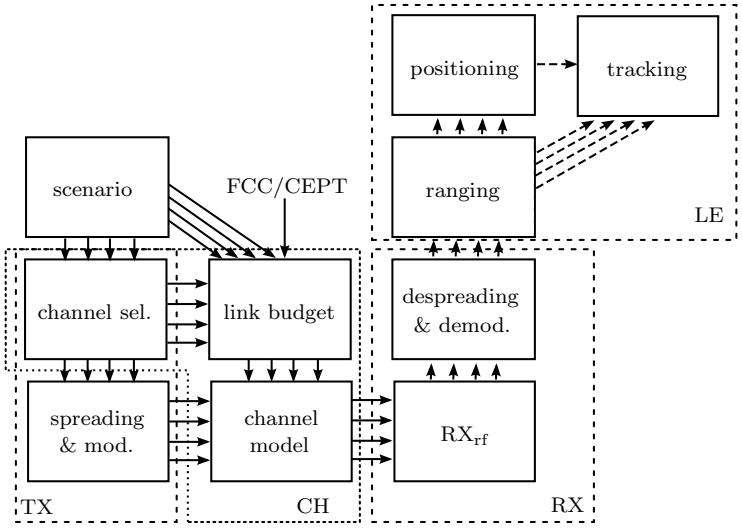

Figure 6.2 Structure of the positioning simulator ([76], © [2010] IEEE)

for IR-UWB can be found in [12] and in Chapter 5 concerning IEEE 802.15.4a preambles. At least three transmitters (base stations) are needed to calculate the position in 2D and four transmitters are needed for 3D. The signals are transmitted over multipath channels, where each signal is convolved with the channel impulse response (CIR) of the link. The signal is received by a UWB antenna and a low noise amplifier (LNA). Next, a coherent or non-coherent receiver is applied to transfer the passband signal into baseband and digital domain. The signal is despread in the demodulation block and the estimated channel response is obtained.

In the LE block, the times-of-arrival and thus the distances to the base stations are estimated by a ranging algorithm. Next, the estimated ranges are combined in the positioning block, where the coordinates of the mobile are estimated. The final block implements the tracking, where the mobile uses previous location estimates to improve the current estimate. The tracking algorithm uses the ranging or positioning estimates as input values.

6.2 Positioning Simulator

The structure of the positioning simulator is shown in Figure 6.2. As the simulator uses measured channel impulse responses and a user-defined geometrical setup, the structure of the simulator for TX and the channel (CH) is slightly changed in comparison to Figure 6.1. The simulator works in complex baseband for reasons of simulation speed. Its blocks are described in the next sub-sections.

6.2.1 Scenario

The first block defines the location of the base station and the location of the mobile. The placement of the mobile can be done according to a stochastic algorithm or to deterministic locations. If a tracking analysis is desired, a trajectory of the mobile has to be defined. The simulator uses virtual environments, which means that the kind of the link from the base station to the mobile is defined

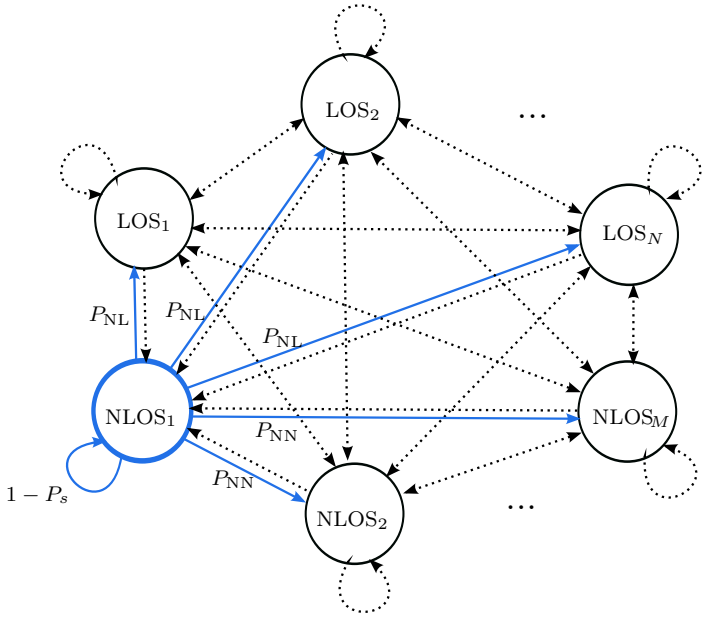

Figure 6.3 Channel Selection State Machine with the transition probabilities for a NLOS link. ([76], © [2010] IEEE)

statistically. In particular, the user defines the probability of an LOS link P_{LOS}. If we assume four base stations, we can see the probabilities for multiple NLOS links P_N per location in Table 6.1.

Table 6.1 Probability of N NLOS links
$P_N(P_{\mathrm{LOS}})$ with user defined LOS probability per link P_{LOS}.

N	$P_N(1)$	$P_N(0.9)$	$P_N(0.8)$	$P_N(0.7)$	$P_N(0.6)$	$P_N(0.5)$	Equation
0	1	0.656	0.410	0.240	0.130	0.063	P_{LOS}^4
1	0	0.292	0.410	0.412	0.346	0.250	$4\,P_{\mathrm{LOS}}^3(1-P_{\mathrm{LOS}})$
2	0	0.049	0.154	0.265	0.346	0.375	$6\,P_{\mathrm{LOS}}^2(1-P_{\mathrm{LOS}})^2$
3	0	0.004	0.026	0.076	0.154	0.250	$4\,P_{\mathrm{LOS}}(1-P_{\mathrm{LOS}})^3$
4	0	0	0.002	0.008	0.026	0.063	$(1-P_{\mathrm{LOS}})^4$

6.2.2 Channel Selection (channel sel.)

The simulator uses measured channel impulse responses. The CIRs are extracted from an extensive measurement campaign in LOS/NLOS indoor and outdoor environments (see Chapter 3). The bandwidth of the pulses $B = 500$ MHz and the measurements have been conducted according to the FCC and CEPT regulations. The CIRs have been measured on a 3×5 grid with a spacing of 10cm. One such grid builds a so-called measurement pool.

If the mobile moves along a trajectory, new CIRs are loaded for each position according to the channel selection state machine in Figure 6.3. The bold node NLOS$_1$ is assumed to be the current measurement pool. P_s defines the propability to switch to another measurement pool, while $1 - P_s$

defines the probability to stay in the current measurement pool. P_s is defined by the distance dependent correlation coefficient of the large scale fading (LSF) ρ_{LSF}. A model for ρ_{LSF} can be found in [77] and is given by

$$\rho_{\mathrm{LSF}} := e^{-\frac{\Delta d}{d_{\mathrm{decorr}}}} \tag{6.1}$$

where Δd is the distance change of the mobile and d_{decorr} is the decorrelation distance. The switching probability P_s is defined as

$$P_s(\mathbf{x}_i|\mathbf{x}_s) = 1 - \rho_{\mathrm{LSF}} = 1 - e^{-\frac{||\mathbf{x}_s - \mathbf{x}_i||}{d_{\mathrm{decorr}}}} \tag{6.2}$$

where $\mathbf{x}_i$ are the current coordinates $[x_i, y_i]^T$ and $\mathbf{x}_s$ are the coordinates of the state entry. Reference [78] shows that d_{decorr} can be between 0.3 and 2.7 m in indoor environments. The transition probabilities P_T to the other measurement pools are given by

$$P_T(\mathrm{LOS}|\mathrm{LOS}) = \quad P_{\mathrm{LL}} = \quad \frac{1}{N-1} P_s \, P_{\mathrm{LOS}} \tag{6.3}$$

$$P_T(\mathrm{NLOS}|\mathrm{LOS}) = \quad P_{\mathrm{LN}} = \quad \frac{1}{M} P_s \, (1 - P_{\mathrm{LOS}}) \tag{6.4}$$

$$P_T(\mathrm{LOS}|\mathrm{NLOS}) = \quad P_{\mathrm{NL}} = \quad \frac{1}{N} P_s \, P_{\mathrm{LOS}} \tag{6.5}$$

$$P_T(\mathrm{NLOS}|\mathrm{NLOS}) = \quad P_{\mathrm{NN}} = \quad \frac{1}{M-1} P_s \, (1 - P_{\mathrm{LOS}}). \tag{6.6}$$

The number of LOS pools is N and the number of NLOS pools is M. The finally selected pool and the CIR within the pool are randomly chosen.

6.2.3 Code Spreading & Modulation (spreading & mod.)

The measured CIR is convolved with the pulse shape and the preamble sequence of the AIP. The received signal from the i-th base station $\tilde{r}_i(t)$ is given by

$$\tilde{r}_i(t) = \sqrt{E_p} \sum_{m=0}^{M-1} c[m] w \left(t - \frac{m}{R} \right) * h_{c,i}(t) \tag{6.7}$$

where E_p is the pulse energy, $w(t)$ is the UWB pulse shape, $c[m]$ is the m-th preamble code element, M is the number of preamble code elements, R is the pulse repetition rate, and $h_{c,i}(t)$ is the CIR occurring at the i-th base station.

6.2.4 Link Budget

The maximum allowed transmit pulse energy E_p is limited by local regulations, which are further defined by the AIP. For instance, the IEEE 802.15.4a standard contains many parameters that have a strong influence on the allowed transmit energy. The analysis of the FCC/CEPT regulations is described in detail for the IEEE 802.15.4a in Section 5.2. It is shown, that in general longer spreading of the pulse sequences leads to higher allowed transmit energy. On the other hand, the complexity of the whole system will increase, which leads to a trade-off between maximum operating distance and samples that have to be processed (see Section 5.4.3). The input signal-to-noise ratio E_{rp}/N_0 is calculated in the link budget block. The noise spectral density $N_0 = \kappa T_0 F$, where κ is the Boltzmann constant, T_0 is the operating temperature, and F is the noise figure of the receiver input structure. Finally, implementation losses have to be taken into account. The link budget for the analysis at reference distance $d_0 = 1$ m is shown in Table 6.2.

6.2.5 Large-Scale Channel Model

A large-scale channel model is needed to obtain the input SNR for the receivers E_{rp}/N_0 at the receiving distance d_i, which is given by

$$\frac{E_{\mathrm{rp}}}{N_0}(d_i, f_c)_{\mathrm{dB}} = \frac{E_{\mathrm{rp}}}{N_0}(d_0, f_c)_{\mathrm{dB}} - 10\eta \log\left(\frac{d_i}{d_0}\right) + S_{\mathrm{dB}} \tag{6.8}$$

where η is the pathloss exponent and S_{dB} is a log-normal random variable with standard deviation σ_s in dB. Experimentally evaluated values for η and σ_s can be found in Chapter 3. As a measurement pool corresponds to a small area, the large scale fading (LSF) is constant within a measurement pool. Furthermore, the small scale fading (SSF) is contained in the measurements, since the energy of the CIRs has been normalized to the mean of their measurement pool. Finally, artificial additive white Gaussian noise $n_i(t)$ according to $E_{\mathrm{rp}}/N_0(d_i, f_c)$ is added to $\tilde{r}_i(t)$. The received signal is given by

$$r_i(t) = \tilde{r}_i(t) + n_i(t). \tag{6.9}$$

6.2.6 Analog Receiver Input Structure $\mathrm{RX_{rf}}$ / Despreading & demodulation

The analog part of a UWB receiver is responsible for receiving, filtering, amplifying, down-converting[1], and sampling of the UWB signals. The large bandwidth of the signals implies strong requirements for the hardware. Especially the design of low-power devices is very challenging, because the large bandwidth leads to very high sampling rates. A high-performance coherent receiver and a low-complexity energy detector have been discussed and analyzed in the previous chapters and are both used in the simulator. A major focus of the previous analyses was on the despreading, where the sequence of channel responses is combined to a single one to improve the SNR.

6.2.7 Ranging

A ranging algorithm is applied on the channel impulse response $\hat{h}[n]$ to estimate the exact time of arrival of the LOS-component. As we focus on low complexity ranging, e.g. threshold based ranging can be applied. The LOS component is not necessarily the strongest component even in LOS scenarios (e.g. [52]). Thus a search-back algorithm needs to be applied, where the LOS component is found within a search-back window ahead of the strongest component of $\hat{h}[n]$ (e.g. [52, 61], Section 4.3).

6.2.8 Positioning

The estimated distances in ToA ranging describe circles on which the actual position lies. Thus a non-linear system of equations, which maybe over-determined, has to be solved to obtain the coordinates of the mobile. Several approaches are reported in the literature. Many perform a linearization first and solve the resulting linear system of equations e.g. with least squares (e.g. [79, 80]). The location estimation is based only on a single observation, thus ranging errors caused by NLOS scenarios or linearization errors can lead to large estimation errors. In tracking, the current estimate also takes past estimates into account, which usually leads to better performance.

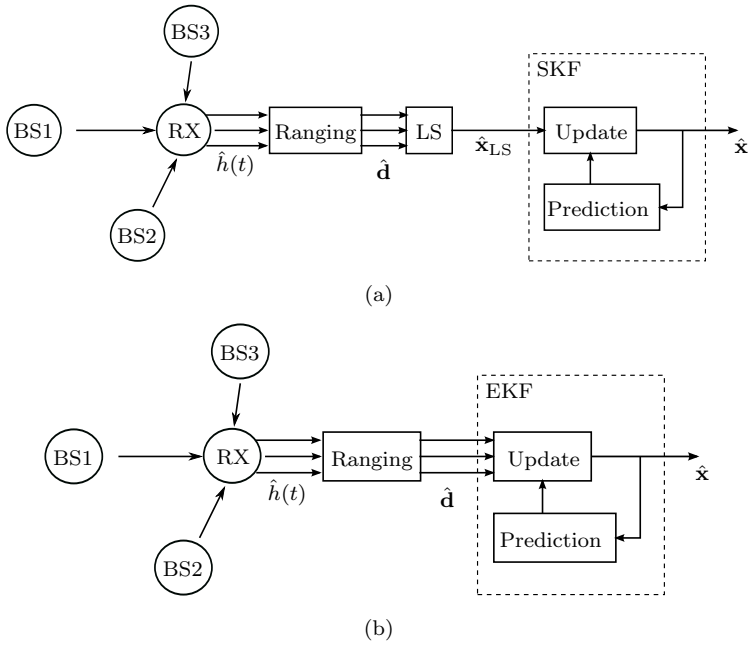

Figure 6.4 Kalman Filter Principles (a) Standard Kalman Filter (SKF) (b) Extended Kalman Filter (EKF)

6.2.9 Tracking

Tracking refers to the sequential estimation of the position of the mobile also taking previous estimates into account. Outliers can be detected, attenuated, or completely canceled. Furthermore, other motion parameters can also be tracked, e.g. velocity and acceleration. A common approach for the tracking problem is Kalman filtering. Unfortunately, Kalman filters provide only the optimal solution if the noise is zero-mean white Gaussian[2] with known variances and the problem has to be linear [82]. As the position estimation problem is non-linear, a linearization can be done with the positioning algorithm, that delivers the estimated coordinates to the tracking algorithm. This enables for example the use of a standard Kalman filter (SKF), which is shown in Figure 6.4(a). As a second option, the extended Kalman filter(EKF) can be used, which can also handle the non-linearity and can process the range estimates directly (see Figure 6.4(b)). It solves the non-linearity problem in a sub optimal way, but again a Gaussian approximation is done (e.g. [81]). If both non-linearity and non-Gaussianity should be considered, one can resort to particle approximation techniques [81]. As we focus on low-complexity positioning and those techniques require a rather high computational effort [83], the rest of the work deals with Kalman-filter based tracking.

6.3 Simulation Setup

In this work U-SPOT is used for the analysis of the localization capabilities of the IEEE 802.15.4a standard. An LS-positioning algorithm, an SKF, and an EKF are compared using measurements of

[1] As the simulator is in complex baseband, this part is not included in the simulation framework.
[2] If the Gaussian assumption is not valid, the filter is still the best linear filter [81].

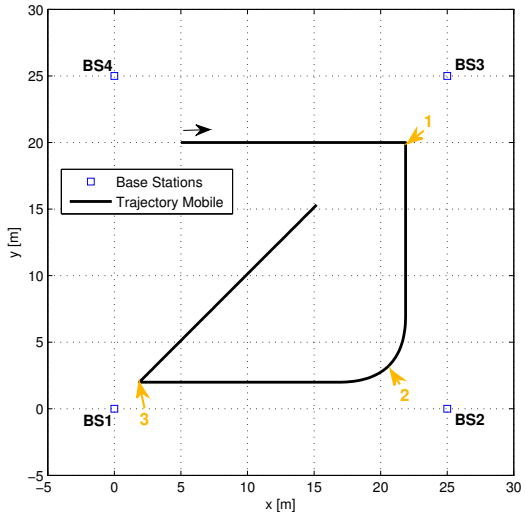

(a)

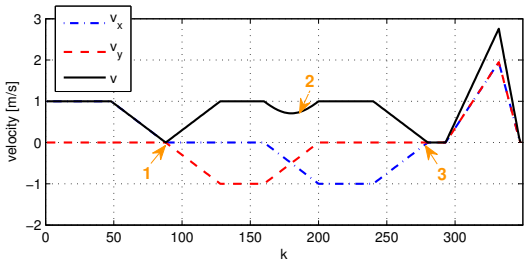

(b) ([76], © [2010] IEEE)

Figure 6.5 Positioning scenario with the trajectory of the mobile, (a) shows the map and (b) shows the velocities of the trajectory.

Table 6.2 Link budgets for U-SPOT evaluation,
$N_{\text{sync}} = 1024$, $N_s = 31$, $L = 16$, $f_c = 4.4928$ GHz, and $B = 499.2$ MHz

Parameter		LOS Values	NLOS Values	Unit
Preamble Energy (incl. G_{TX})	E_{pr}	-68.22	-68.22	dBWs
Pathloss @ 1 meter	$\text{PL}(1\text{m}, f_c)$	43.89	48.22	dB
Receiver antenna gain	G_{RX}	0	0	dBi
Received preamble energy	$\tilde{E}_{\text{rp}}(1\text{m}, f_c)$	-112.11	-116.44	dBWs
Noise Spectral Density	N_0	$-198,93$	$-198,93$	dBW/Hz
Implementation Loss	L_{imp}	4	4	dB
Receiver Input SNR	$\frac{E_{\text{rp}}}{N_0}(1\text{m}, f_c)$	82.62	78.49	dB

office LOS and NLOS environments. Figure 6.5(a) shows the positioning scenario, where four base stations are placed on a square of 25×25 m. A base stations separation of 25 m is chosen, as still good ranging is achieved in NLOS situations for both receiver types. Higher separations will lead to a loss in reliability and the detection and cancellation of NLOS links will become much more important. The velocities of the defined trajectory are shown in Figure 6.5(b). Point 1 shows a stopping of the mobile, while Point 2 is in the middle of the curve, where the velocities are continuously changing. In Point 3 the mobile stops for 3 seconds and afterwards the mobile accelerates and decelerates strongly.

All channel impulse responses have been measured with a bandwidth of 500 MHz and a carrier frequency of 4.5 GHz. For NLOS two offices have been measured with one wall inbetween, made of plaster or concrete depending on the position[3]. The LOS scenario is an office floor environment surrounded by concrete walls. A detailed description of the measurements and the corresponding channel models can be found in Chapter 3. The channel models are used with a pathloss exponent $\eta_{\text{LOS}} = 1.49$ and $\eta_{\text{NLOS}} = 2.92$ for LOS and NLOS respectively. The standard deviation of the large scale fading $\sigma_s = 1.15$ dB and $\sigma_s = 5.12$ dB respectively. The decorrelation distance of the large scale fading is $d_{\text{decorr}} = 1$ m.

Only the IEEE 802.15.4a preamble is transmitted in the simulations, using a preamble symbol length of $N_s = 31$, the spreading factor $L = 64$, and $N_{\text{sync}} = 1024$ symbol repetitions. This preamble leads to a high maximum allowed transmit energy according to the FCC regulations (see Section 5.4.1).

6.3.1 Link Budget

The corresponding link budget is shown in Table 6.2 for LOS and NLOS links. The receiver input SNR $E_{\text{rp}}/N_0(1\text{m})$ is the input SNR of the receiver at 1 m, which depends on the link budget. The average power limit of the FCC regulations applies for the used preamble sequence and the exact maximum allowed preamble energy E_{pr} is calculated according to Section 5.3. The pathloss $\text{PL}(1m)$ is given by 43.89 and 48.22 dB for the office LOS and NLOS environment respectively (see Table 3.3). Thus a four dB higher input SNR is achieved at 1 m for LOS in comparison to NLOS. In contrast to the link budget of 5.3, this one yields the received preamble energy with multipath components. The other parameters are defined as in Section 5.3.

[3]The outdoor location has been canceled for the simulations due to a lack of connectivity

6.3.2 Receivers

The localization performance of the energy detector (see Figure 4.1) and the coherent receiver (see Figure 5.1) are analyzed in this chapter. The preamble for the IEEE 802.15.4a standard shows perfect circular auto correlation properties for both receivers. The despreading sequence c_i is the same as the spreading sequence for the coherent receiver, while for the energy detector a modified sequence $\tilde{c}_i$ is necessary, as the polarity information gets lost due to squaring. The preamble code sequence c_i has to be squared that all active code elements become +1, and all non-active code elements are set to -1 [44]. Our simulations have shown, that for the energy detector and pulses with a bandwidth of 500 MHz, an integration time of 2 ns delivers the best results [62], thus $T_I = 2$ ns and the sampling rate $1/T = 0.5$ Gsamples/s will be used for the rest of this analysis. The sampling rate for the coherent receiver is fixed to 2 Gsamples/s.

6.3.3 Threshold-Based Ranging

The detection of the LOS component for range estimation is implemented as a jump-back search-forward algorithm (see Section 4.3) applied on the estimated channel impulse response $\hat{h}[n]$. The optimal threshold for the scenario has been obtained by Monte-Carlo simulations, where the position of the mobile has been varied uniformly distributed inbetween the base stations. As the system should be optimized for NLOS scenarios, the simulations are performed with 100% NLOS. The optimal threshold c_{opt} is 0.1 and 0.15 for the energy detector and the coherent receiver respectively. It is defined as

$$c_{\text{opt}} = \underset{c}{\text{argmin}}\{\text{MAE}'\} \tag{6.10}$$

with

$$\text{MAE}' = \text{mean}\left\{|e_d[n]|\big||e_d[n]| \leq T_{\text{sb}}\zeta\right\} \tag{6.11}$$

where $e_d[n] = \hat{d}[n] - d[n]$ is the distance error, T_{sb} is the duration of the search back window and ζ is the speed of the light. The length of the search-back window has been defined to be 30 ns [62]. The standard deviation of the ranging error $\sigma_r = 0.63$ m and $\sigma_r = 0.32$ m for the energy detector and the coherent receiver respectively.

6.3.4 Least Squares Positioning

As we estimated the range to the base stations, we know that the mobile is on a circle with radius d to the base stations. Thus it is necessary to solve a system of non-linear equations to obtain the coordinates of the mobile,

$$\begin{aligned}
\hat{d}_{\text{BS1}} &= h(\mathbf{x}_{\text{BS1}}, \hat{\mathbf{x}}_c) = \sqrt{(x_{\text{BS1}} - \hat{x})^2 + (y_{\text{BS1}} - \hat{y})^2} \\
\hat{d}_{\text{BS2}} &= h(\mathbf{x}_{\text{BS2}}, \hat{\mathbf{x}}_c) = \sqrt{(x_{\text{BS2}} - \hat{x})^2 + (y_{\text{BS2}} - \hat{y})^2} \\
&\vdots \qquad\qquad\qquad\qquad \vdots \\
\hat{d}_{\text{BS}i} &= h(\mathbf{x}_{\text{BS}i}, \hat{\mathbf{x}}_c) = \sqrt{(x_{\text{BS}i} - \hat{x})^2 + (y_{\text{BS}i} - \hat{y})^2} \\
&\vdots \qquad\qquad\qquad\qquad \vdots \\
\hat{d}_{\text{BS}N} &= h(\mathbf{x}_{\text{BS}N}, \hat{\mathbf{x}}_c) = \sqrt{(x_{\text{BS}N} - \hat{x})^2 + (y_{\text{BS}N} - \hat{y})^2}
\end{aligned}$$

$h(\mathbf{x}_{\mathrm{BS}i}, \hat{\mathbf{x}}_c)$ describe the circle equation centered at the i-th base station coordinates $\mathbf{x}_{\mathrm{BS}i} = [x_{\mathrm{BS}i}, y_{\mathrm{BS}i}]^T$, $\hat{\mathbf{x}}_c = [\hat{x}, \hat{y}]^T$ are the unknown coordinates of the mobile, and $\hat{d}_{\mathrm{BS}i}$ is the estimated distance to the i-th base station. The set of non-linear equations is linearized using Taylor series expansion. After discarding all the higher order components, we obtain

$$\hat{d} = h(x_0, y_0) + \left.\frac{\partial h}{\partial \hat{x}}\right|_{(x_0,y_0)} (\hat{x} - x_0) + \left.\frac{\partial h}{\partial \hat{y}}\right|_{(x_0,y_0)} (\hat{y} - y_0) \tag{6.12}$$

where (x_0, y_0) is the linearization point. It is initialized as the mean of the base station coordinates. $h(x_0, y_0)$ is the value of the non-linear function at the linearization point. $\frac{\partial h}{\partial \hat{x}}|_{(x_0,y_0)}$ denotes the derivative with respect to $\hat{x}$ at (x_0, y_0). Equation (6.12) can be rearranged to

$$\underbrace{\hat{d} - h(x_0, y_0) + \left.\frac{\partial h}{\partial \hat{x}}\right|_{(x_0,y_0)} x_0 + \left.\frac{\partial h}{\partial \hat{y}}\right|_{(x_0,y_0)} y_0}_{=\hat{d}'} = \left.\frac{\partial h}{\partial \hat{x}}\right|_{(x_0,y_0)} \hat{x} + \left.\frac{\partial h}{\partial \hat{y}}\right|_{(x_0,y_0)} \hat{y}. \tag{6.13}$$

and the left side can be combined to $\hat{d}'$ because all terms are known. The least squares (LS) solution for the estimated coordinates in matrix notation is given by

$$\hat{\mathbf{x}}_{\mathrm{LS}} = (\mathbf{J}^T\mathbf{J})^{-1}\mathbf{J}^T\hat{\mathbf{d}}' \tag{6.14}$$

where $\mathbf{J}$ is the Jacobian matrix that is defined as

$$\mathbf{J} = \left.\begin{bmatrix} \frac{\partial h(\mathbf{x}_{\mathrm{BS}1}, \hat{\mathbf{x}}_c)}{\partial x} & \frac{\partial h(\mathbf{x}_{\mathrm{BS}1}, \hat{\mathbf{x}}_c)}{\partial y} \\ \vdots & \vdots \\ \frac{\partial h(\mathbf{x}_{\mathrm{BS}N}, \hat{\mathbf{x}}_c)}{\partial x} & \frac{\partial h(\mathbf{x}_{\mathrm{BS}N}, \hat{\mathbf{x}}_c)}{\partial y} \end{bmatrix}\right|_{(x_0,y_0)}. \tag{6.15}$$

As the optimal linearization point is unknown, the obtained coordinates are used as a new linearization point. This procedure is repeated until the estimated coordinates converge. The full derivation of the algorithm can be found in [84].

6.3.5 Tracking

An Standard Kalman Filter and an Extended Kalman Filter are analyzed in this chapter.

Standard Kalman Filter (SKF)

The standard Kalman filter is only usable for linear equation systems, hence the LS position estimation is used as input to the filter (see Figure 6.4(a)). The Kalman filter smoothes the estimated coordinates obtained from the LS solution, and estimates a so-called state vector $\hat{\mathbf{x}} = [\hat{x}, \hat{y}, \hat{v}_x, \hat{v}_y, \hat{a}_x, \hat{a}_y]^T$, where $[\hat{x}, \hat{y}]$ are the estimated coordinates of the mobile, $[\hat{v}_x, \hat{v}_y]$ are the estimated velocities in $[x, y]$ direction, and $[\hat{a}_x, \hat{a}_y]$ are the estimated accelerations. This is usually called the position, velocity and acceleration (PVA) motion model. The Kalman filter consists of a prediction and correction stage. First, it performs a prediction of the next state vector based on the motion model, and as a second step the prediction is corrected by the measurement (the LS position estimate).

A state transition model (motion model) describes the state change from one position to the other and is defined by

$$\mathbf{x}_k = \mathbf{A}\mathbf{x}_{k-1} + \mathbf{B}\mathbf{u}_k \tag{6.16}$$

where $\mathbf{x}_k$ is the actual state vector at time step k and the state noise vector is given by $\mathbf{u}_k = [\tilde{a}_x, \tilde{a}_y]^T$, where $\tilde{a}_x$ and $\tilde{a}_y$ model the noise of the accelerations in x- and y-direction. $\mathbf{A}$ is the state transition matrix and $\mathbf{B}$ relates the state noise to the state variables. The matrices are defined as follows:

$$\mathbf{A} = \begin{bmatrix} 1 & 0 & \Delta t & 0 & \frac{\Delta t^2}{2} & 0 \\ 0 & 1 & 0 & \Delta t & 0 & \frac{\Delta t^2}{2} \\ 0 & 0 & 1 & 0 & \Delta t & 0 \\ 0 & 0 & 0 & 1 & 0 & \Delta t \\ 0 & 0 & 0 & 0 & 1 & 0 \\ 0 & 0 & 0 & 0 & 0 & 1 \end{bmatrix} \quad \mathbf{B} = \begin{bmatrix} \frac{\Delta t^2}{2} & 0 \\ 0 & \frac{\Delta t^2}{2} \\ \Delta t & 0 \\ 0 & \Delta t \\ 1 & 0 \\ 0 & 1 \end{bmatrix}. \tag{6.17}$$

The update interval is $\Delta t = 0.25$ s in the simulations. The prediction and updating procedure of the SKF are shown in equation (6.18) to (6.22).

Prediction

Equation (6.16) directly implies the first Kalman equation, skipping the unknown state noise.

$$\hat{\mathbf{x}}_k^- = \mathbf{A}\hat{\mathbf{x}}_{k-1} \tag{6.18}$$

$$\mathbf{P}_k^- = \mathbf{A}\mathbf{P}_{k-1}\mathbf{A}^T + \mathbf{Q} \tag{6.19}$$

where $\hat{\mathbf{x}}_k^-$ is the predicted state vector, $\mathbf{P}_k^-$ and $\mathbf{P}_{k-1}$ is the predicted and previous error covariance matrix, respectively. The matrix $\mathbf{Q}$ is the state covariance matrix, which is a 6×6 zero matrix except for $Q_{5,5} = \sigma_{a_x}^2$ and $Q_{6,6} = \sigma_{a_y}^2$.

Correction

$$\mathbf{K}_k = \mathbf{P}_k\mathbf{H}^T\mathbf{C}^{-1} = \mathbf{P}_k^-\mathbf{H}^{\mathrm{T}}(\mathbf{H}\mathbf{P}_k^-\mathbf{H}^T + \mathbf{C})^{-1} \tag{6.20}$$

$$\hat{\mathbf{x}}_k = \hat{\mathbf{x}}_k^- + \mathbf{K}_k(\hat{\mathbf{x}}_{\mathrm{LS},k} - \mathbf{H}\mathbf{x}_k^-) \tag{6.21}$$

$$\mathbf{P}_k = (\mathbf{I} - \mathbf{K}_k\mathbf{H})\mathbf{P}_k^- \tag{6.22}$$

where $\mathbf{K}_k$ is the Kalman gain, $\hat{\mathbf{x}}_{\mathrm{LS},k}$ is the LS-position estimate, $\mathbf{C}$ is the measurement covariance matrix, and $\mathbf{I}$ is the identity matrix. $\mathbf{H}$ is the observation matrix defined as a 2x6 zero matrix except $H_{1,1} = H_{2,2} = 1$. The tuning of the Kalman filter is done using $\mathbf{Q}$ and $\mathbf{C}$. As the state noise of the given trajectory is not Gaussian (see Figure 6.6(c)), Monte Carlo simulations are necessary to optimize these variances for the initialization of $\mathbf{Q}$ (see Section 6.3.6). Matrix $\mathbf{C}$ is obtained from the ranging simulation of Section 4.3 applying the positioning algorithm on the estimated ranges using the optimal threshold. Thus, the reliability of the Kalman filter on the measurements is defined according to a 100% NLOS (worst case) scenario. The standard deviations of the LS estimation for the coordinates x and y are given by $\sigma_{\hat{x}} = \sigma_{\hat{y}} = 1.21$ m for the energy detector and $\sigma_{\hat{x}} = \sigma_{\hat{y}} = 1.33$ m for the coherent receiver, and $\mathbf{C} = [\sigma_{\hat{x}}^2\ 0; 0\ \sigma_{\hat{y}}^2]$.

Note, $\mathbf{K}_k$, $\mathbf{P}_k$, and $\mathbf{P}_k^-$ are independent of the measurements. Thus, they can be calculated offline and stored in the memory to save processing power. This can make the difference to achieve real-time processing or not [82]. In contrast, the EKF performs a linearization dependent on the estimated coordinates and so an offline precalculation of these values is not possible. To be fair, the SKF needs also a linearization, which is performed outside of the filter, and so similar processing effort is needed.

Extended Kalman Filter

In contrast to the SKF, the EKF can cope with non-linear equations, as the linearization is directly done in the filter. The updating process is the same as for the SKF but the correction procedure is different.

Correction

$$\mathbf{K}_k = \mathbf{P}_k \mathbf{H}_k^T \mathbf{C}^{-1} = \mathbf{P}_k^- \mathbf{H}_k^{\mathrm{T}} (\mathbf{H}_k \mathbf{P}_k^- \mathbf{H}_k^T + \mathbf{C})^{-1} \tag{6.23}$$

$$\hat{\mathbf{x}}_k = \hat{\mathbf{x}}_k^- + \mathbf{K}_k (\hat{\mathbf{d}}_k - \mathbf{h}(\mathbf{x}_k^-)) \tag{6.24}$$

$$\mathbf{P}_k = (\mathbf{I} - \mathbf{K}_k \mathbf{H}_k) \mathbf{P}_k^- \tag{6.25}$$

where $\hat{\mathbf{d}}_k$ are the estimated ranges, $\mathbf{h}(\mathbf{x}_k^-)$ are the circle equations from (6.12) using the predicted coordinates and $h_i(\mathbf{x}_k^-) = h(\mathbf{x}_{\mathrm{BS}i}, \mathbf{x}_k^-)$, and $\mathbf{H}_k$ is the Jacobian of the observation matrix at the predicted coordinates $(\hat{x}_k^-, \hat{y}_k^-)$

$$\mathbf{H}_k = \left[\begin{array}{cccccc} \frac{\partial h(\mathbf{x}_{\mathrm{BS}1}, \hat{\mathbf{x}}_c)}{\partial x} & \frac{\partial h(\mathbf{x}_{\mathrm{BS}1}, \hat{\mathbf{x}}_c)}{\partial y} & 0 & 0 & 0 & 0 \\ \vdots & \vdots & \vdots & \vdots & \vdots & \vdots \\ \frac{\partial h(\mathbf{x}_{\mathrm{BS}N}, \hat{\mathbf{x}}_c)}{\partial x} & \frac{\partial h(\mathbf{x}_{\mathrm{BS}N}, \hat{\mathbf{x}}_c)}{\partial y} & 0 & 0 & 0 & 0 \end{array} \right] \Bigg|_{(\hat{x}_k^-, \hat{y}_k^-)} . \tag{6.26}$$

The measurement covariance matrix $\mathbf{C} = \sigma_r^2 \mathbf{I}$, where σ_r^2 is the variance of the ranging. The standard deviation $\sigma_r = 0.63$ m for the energy detector and $\sigma_r = 0.32$ m for the coherent receiver (see Section 6.3.3). The predicted coordinates deliver already a good starting point for the linearization, thus it is not necessary to perform iterations as for the SKF with LS. The system complexity should be kept as low as possible, thus we don't consider iterative EKF approaches.

6.3.6 Optimization of the Kalman Filters

The position estimation shows outliers, which are mainly caused by NLOS links, because the LOS component is not correctly detected. As these outliers lead to strong variations of the estimates and forces the Kalman filter to diverge, a proper handling is needed. We introduce the maximal acceleration change within the trajectory $\Delta a_{\max}$, which is calculated offline. The acceleration of the i-th trajectory sample is given by $\mathbf{a}_i = [a_x[i], a_y[i]]^T$. The maximal change is defined by $\Delta a_{\max} = \max_{i=[1 \ldots X-1]} \left\{ \left| \, ||\mathbf{a}_i|| - ||\mathbf{a}_{i-1}|| \, \right| \right\} / \Delta t$, where X is the length of the trajectory and $||.||$ is the Euclidean norm. The estimated accelerations at time k are given by $\hat{\mathbf{a}}_k = [\hat{a}_x[k], \hat{a}_y[k]]^T$ and the instantaneous change of the estimated acceleration is given by $\Delta \hat{a} = \left| \, ||\hat{\mathbf{a}}_k|| - ||\hat{\mathbf{a}}_{k-1}|| \, \right| / \Delta t$. The correction of the estimated state vector for the SKF is modified to (cf. (6.21))

$$\hat{\mathbf{x}}_k = \begin{cases} \hat{\mathbf{x}}_k^- + \mathbf{K}_k (\hat{\mathbf{x}}_{\mathrm{LS},k} - \mathbf{H} \mathbf{x}_k^-) & \Delta \hat{a}_k \leq \beta \, n_{\mathrm{out}} \Delta a_{\max} \\ \hat{\mathbf{x}}_k^- & \text{else} \end{cases} \tag{6.27}$$

and for the EKF to (cf. (6.24))

$$\hat{\mathbf{x}}_k = \begin{cases} \hat{\mathbf{x}}_k^- + \mathbf{K}_k (\hat{\mathbf{d}}_k - \mathbf{h}(\mathbf{x}_k^-)) & \Delta \hat{a}_k \leq \beta \, n_{\mathrm{out}} \Delta a_{\max} \\ \hat{\mathbf{x}}_k^- & \text{else} \end{cases} \tag{6.28}$$

Table 6.3 Parameters optimized with U-SPOT

Paremeter		ED		CR		Unit
Optimal threshold	c_{opt}	0.1		0.15		
Std.dev. ranging	σ_r	0.63		0.32		[m]
Std.dev. positioning	$\sigma_{\hat{x}} = \sigma_{\hat{y}}$	1.21		1.33		[m]
		SKF	EKF	SKF	EKF	
State variance parameter	α	110	380	130	550	
Acceleration threshold	β	$\frac{1}{4}$	$\frac{1}{4}$	$\frac{1}{4}$	$\frac{1}{4}$	

with

$$n_{\text{out}} = \begin{cases} 1 & \Delta\hat{a}_k \leq \beta\, n_{\text{out}} \Delta a_{\max} \\ n_{\text{out}} + 1 & \text{else} \end{cases} \tag{6.29}$$

If β is chosen too small the filter gets problems to follow the trajectory and if it is too large the outliers may not be rejected sufficiently. n_{out} is the current number of consecutive outliers, which multiplies the threshold β. This approach is necessary in order to be able to return to the real trajectory if the estimate has diverged due to a long NLOS period. As the defined trajectory does not have Gaussian accelerations, the initialization for optimal performance has been determined by Monte Carlo simulations. We define the state variances as

$$\sigma_{a_x}^2 = \sigma_{a_y}^2 = \left(\frac{1}{\alpha}\Delta a_{\max}\right)^2. \tag{6.30}$$

A lower allowed α implies less trust in the predicted value, as the state variance is assumed to be too high. In other words, the higher variance of the state noise leads to a higher trust in the measurements (high Kalman gain). If α is chosen too small the filter believes too much on the predicted value and can not follow the trajectory (low Kalman gain). Both parameters depend on each other, thus a two dimensional optimization problem occurs.

The Kalman filters are optimized for $P_{\text{LOS}} = 70\%$, to the given trajectory and the mean error. 20 runs has been performed for the optimization. The optimal values for α and β are shown in Table 6.3. It was observed that high values of β lead to greater errors, because the outliers are not attenuated enough. Below 1/4, the filter cannot follow the last decelerate of the mobile (see Figure 6.5(b)). Thus, the threshold was fixed to $\beta = 1/4$. All concepts achieved very similar mean absolute errors of approx. 0.9 m.

6.3.7 Summary of the Initialization and Optimization using U-SPOT

U-SPOT is used to initialize the Kalman filters. Thus, the variances of the ranging and positioning are obtained for the coherent receiver and the energy detector. Furthermore, the optimal threshold for the ranging in NLOS is determined. Finally, the Kalman filters are optimized for NLOS situations and outliers. The obtained parameters can be found in Table 6.3. Table 6.4 shows a summary of the most important simulation parameters.

Table 6.4 Summary of simulation parameters

Parameter	Abbreviation	Value	
Scenario			
Number of base stations	N	4	
Base station separation		25	[m]
Update rate	$1/\Delta t$	4	[Hz]
IEEE 802.15.4a Standard Parameters			
Pulse bandwidth	B	499.2	[MHz]
Carrier frequency	f_c	4492.8	[MHz]
Preamble code number (with $N_s = 31$)		c6	
Number of preamble symbol repetitions	N_{synch}	1024	
Spreading factor	L	64	
Channel Parameters			
LOS pathloss at 1 m	$\text{PL}(1m, f_c)$	43.89	[dB]
LOS pathloss exponent	η_{LOS}	1.49	
LOS std.dev. LSF	$\sigma_{s,\text{LOS}}$	1.15	[dB]
NLOS pathloss at 1 m	$\text{PL}(1m, f_c)$	48.22	[dB]
NLOS pathloss exponent	η_{NLOS}	2.92	
NLOS std.dev. LSF	$\sigma_{s,\text{NLOS}}$	5.12	[dB]
LSF decorrelation distance	d_{decorr}	1	[m]
Link Budget			
TX antenna gain	G_{TX}	0	[dB]
RX antenna gain	G_{RX}	0	[dB]
Noise figure	F	5	[dB]
Reference temperature	T_0	293	[K]
Implementation losses	L_{imp}	4	[dB]
Energy Detector			
Integration time	T_I	2	[ns]
Coherent Receiver			
Sampling frequency	$1/T$	2	[Gs]

6.4 Performance Evaluation

6.4.1 Tracking Analysis

Figure 6.6 shows the positioning scenario and localization results with four base stations and $P_{\mathrm{LOS}} = 0.7$. Figures 6.6(a) and 6.6(b) shows the localization results of the energy detector and the coherent receiver respectively. It is observable, that the LS estimates deviate significantly from the trajectory, which is typically caused by NLOS links. As mentioned before, the LS estimates are used as input for the SKF and it is obvious that an outlier rejection is necessary. It is observable that the SKF and EKF smooth the estimates and do not show any large outliers, but both Kalman filters are occasionally pushed away from the trajectory. Note that they generally follow the LS estimates. Figure 6.7 shows the CDF of the absolute error averaged over 20 runs. The ranging delivers highly precise results, in which 80% of the estimates show a distance error less than 40 cm. More than 90% of the estimates are within 1 m of the true position. Hence around 2/3 of the NLOS links still lead to sufficient ranging results. Roughly 20% of the range estimates deliver moderately or highly inaccurate results that influence the reliability of the LS-estimation. The robustness of the LS estimation can be significantly improved by the Kalman filters for errors below 2 m. The gain of the Kalman filters for accuracies better than 1 m – the goal of the IEEE 802.15.4a standard – is around 10%, but is still too weak for reliable positioning. Surprisingly, the CR shows only slightly better performance for the positioning in comparison to the ED. The performance of both Kalman filters is very similar in the given scenario.

6.4.2 NLOS Link Analysis

This analysis shows the influence of P_{LOS} on the localization accuracy for the CR and the ED using the previously defined trajectory. The optimization of the Kalman filters was done for $P_{\mathrm{LOS}} = 0.7$. Figure 6.8 shows the mean CDFs of the localization methods, averaged over 20 runs, for specific P_{LOS} values. It is observable that the reliability and accuracy of all approaches decreases significantly with decreasing P_{LOS}. The LS positioning shows the worst performance with high distance errors already at high P_{LOS} values. The Kalman filters increase the reliability significantly even for high ratios of NLOS links ($P_{\mathrm{LOS}} \geq 40\%$), but an accuracy better than 1 m with sufficient reliability is only achieved at very low ratios ($P_{\mathrm{LOS}} \geq 80\%$). The Kalman filters show similar performance between 40 and 100% LOS. Below the SKF shows better robustness in comparison to the EKF. Furthermore, only in NLOS dominated environments the highly complex coherent receiver shows an advantage in comparison to the energy detector. The best robustness is achieved with the CR and the SKF, which works in 100% NLOS within 3 m with 70% reliability.

As the goal of IEEE 802.15.4a with accuracies better than 1 m has not been achieved, it is necessary to improve the given concepts for the specific scenario. A detailed analysis of enhanced channel estimation and ranging methods for energy detectors is given in [55, 56]. Other simple approaches can be used for more robustness e.g. using only the three strongest signals for the localization.

6.5 Summary

A novel UWB positioning simulator has been presented, which uses statistically defined virtual environments to enable mixed line-of-sight and non-line-of-sight simulations. A channel selection algorithm is introduced for realistic simulations with experimental data. The simulator has been used for the

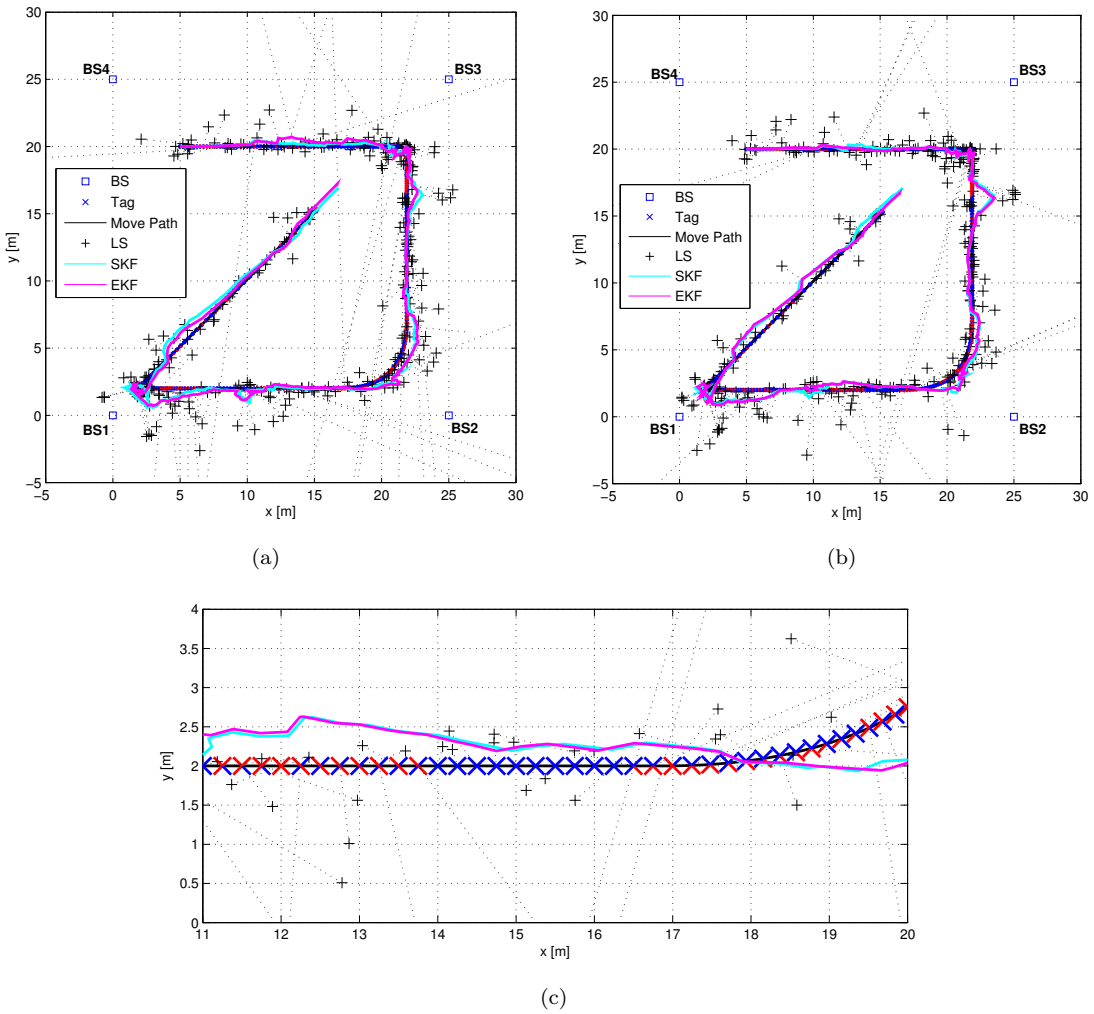

Figure 6.6 Positioning scenario and results for $P_{\mathrm{LOS}} = 0.7$ with (a) the energy detector and (b) the coherent receiver, (c) is a zoom into (b). The crosses indicate the real position of the mobile, in which a blue part indicates a LOS and a red one an NLOS link to the specific base station. The dotted lines connect the LS estimates to their real locations.

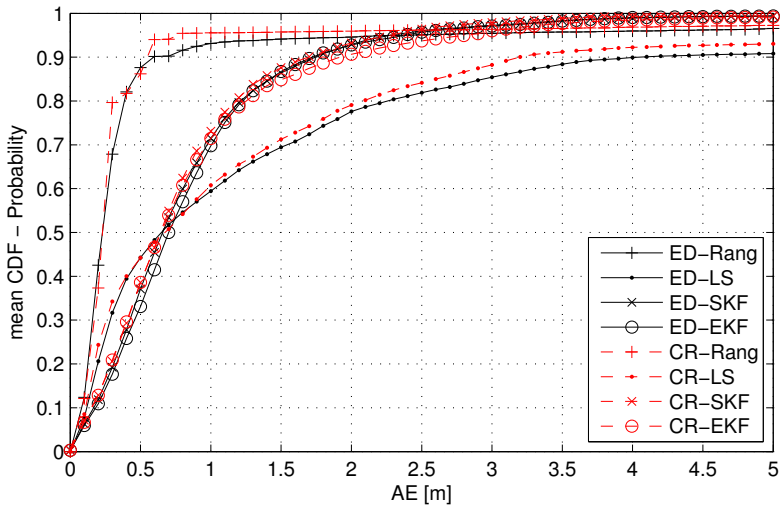

Figure 6.7 CDF of the mean absolute error averaged over 20 repetitions.

analysis of the IEEE 802.15.4a standard with respect to its positioning and tracking capabilities. Furthermore, the parameters for the ranging, positioning and tracking using energy detectors and coherent receivers have been determined and optimized with U-SPOT. It has been shown that the coherent receiver is more robust than the energy detector in scenarios with a high probability of NLOS situations. A least squares positioning algorithm is compared with a standard and an extended Kalman filter. The tracking algorithms can significantly improve the reliability of NLOS position estimations by rejecting and smoothing of outliers. Finally, it is shown that the performance of all algorithms drops significantly for a high ratio of NLOS links. The best performance has been achieved with the coherent receiver and a standard Kalman filter. The goal of the IEEE 802.15.4a standard to achieve positioning with an accuracy better than 1 m with sufficient reliability is only achieved in scenarios with a high probability of LOS links.

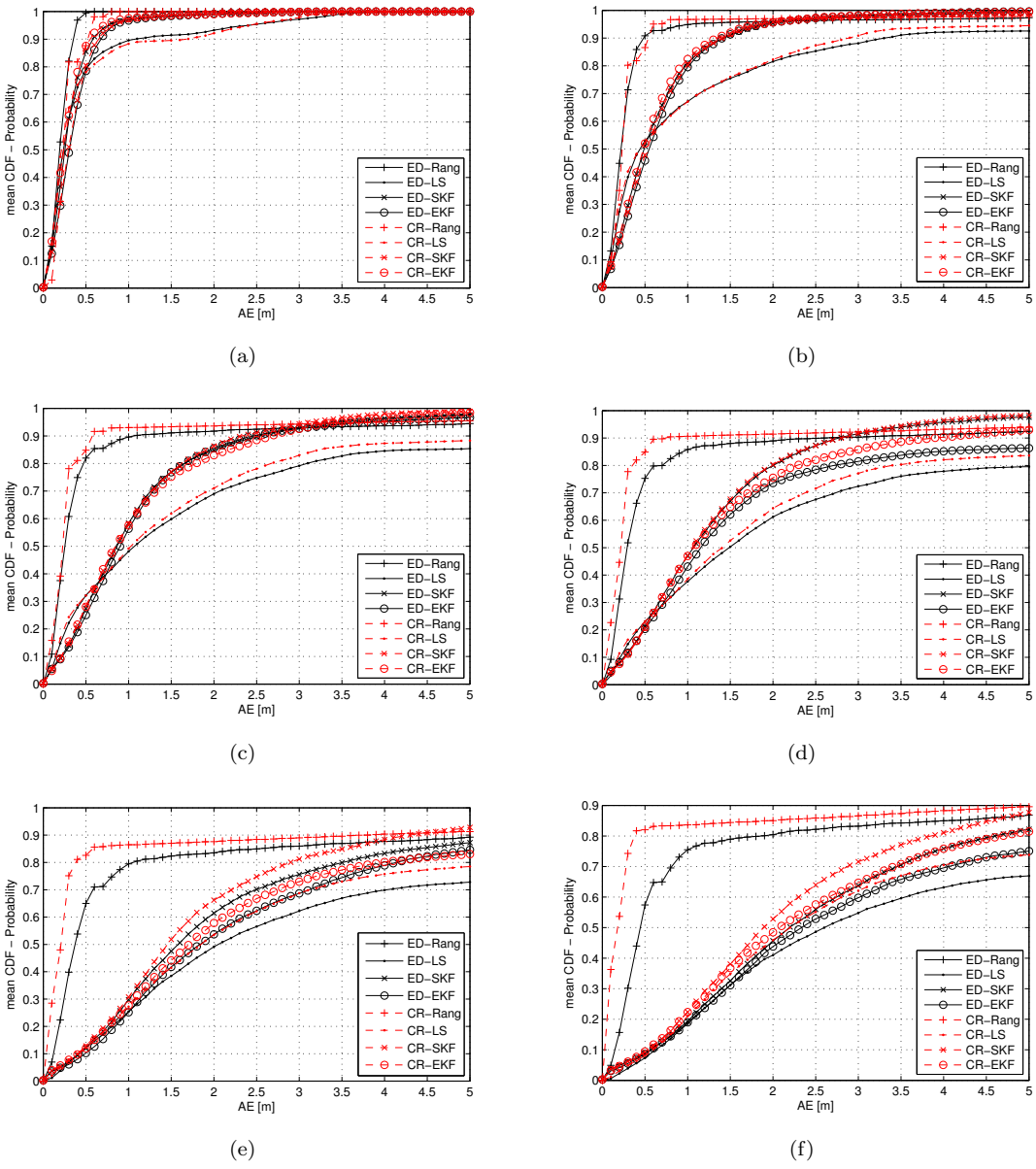

Figure 6.8 Line-of-Sight Analysis for energy detector (solid, black) and the coherent receiver (dashed, red) with respect to (a) 100% LOS, (b) 80% LOS, (c) 60% LOS, (d) 40% LOS, (e) 20% LOS, (f) 0% LOS

7 Conclusions and Recommendations

This thesis analyzes low-complexity impulse-radio (IR) Ultra-Wideband (UWB) localization systems based on time-of-arrival (ToA) ranging. A key element of a low-complexity IR-UWB localization system is the receiver, thus the analysis, modeling, and simulation of low-complexity energy detectors is of special interest.

7.1 Coherent and Non-Coherent Receiver Architectures

Within the entire work, the energy detector is compared with a high-complexity coherent receiver and the trade-off between complexity and performance is studied. It is shown that the ranging performance of the energy detector significantly depends on the input SNR, but also on the system parameters, which are pulse bandwidth, integration time and number of combined pulses. The energy detector suffers from the squared noise leading to non-coherent combining loss, which has a strong influence on the output SNR of the detector. The performance of the coherent receiver only depends on the input SNR, but has to apply Nyquist sampling and is so dependent on the bandwidth of the signals, while the energy detector is independent. The integration time of the energy detector is directly related to the achieveable ranging accuracy, which limits the integration time to a few ns. It is shown that the despreading effort for both receivers is similar for signals with a bandwidth of 500 MHz. On the other hand, the coherent receiver needs to estimate the carrier frequency, which is a quite tough task due to the very short UWB pulses hidden in the noise floor. This could be an interesting topic for further studies.

7.2 The IEEE 802.15.4a Standard

A central goal of this thesis is the analysis of the IEEE 802.15.4a standard, which defines a large set of signal parameters. Their impact on the performance of the receivers and the ranging accuracy is studied. The codes of the IEEE 802.15.4a standard show perfect circular autocorrelation properties for coherent an non-coherent receivers with the intention of preventing inter-pulse-interference (IPI). It is shown that IPI can only be canceled for coherent receivers, while for the energy detector the squaring prevents a complete cancellation. A large spacing of the pulse sequences allows two advantages: First, it reduces IPI and second, it allows for the transmission of more power. The latter is possible due to the long averaging time for the mean power calculation according to FCC/CEPT regulations. Furthermore, more bandwidth also implies more transmit power. A higher transmit power leads

to a longer maximum operating distance. However, this directly relates to the output SNR of the receiver and therefore, the energy detector depends again strongly on the system parameters. Ranging based on the preambles of the IEEE 802.15.4a standard achieve maximum operating distances (in free space) up to several hundred meters for the energy detector and up to several thousand meters for the coherent receiver. It follows that both receivers are very suitable for real-time localization systems, wireless sensor networks and navigation systems for indoor and short-range outdoor. Other important factors of influence are the bandwidths and the carrier frequencies of the frequency channels. It is shown that the Low-Band channels outperform the High-Band channels by achieving up to 3-fold range for both receiver architectures, which cannot be compensated with larger bandwidths. As many standardization activities are currently ongoing, the presented framework could be used for the evaluation and development of the new standards.

7.3 The UWB Demonstrator System

A modular UWB demonstrator system has been developed for ranging and positioning experiments. The central element of the system is an FPGA, which implements the signalling schemes defined by the IEEE 802.15.4a standard. Furthermore, the system is satisfying the FCC/CEPT regulations. The data processing is held offline for highest flexibility and so the receiver and ranging algorithms are implemented in software. An extensive measurement campaign has been performed in LOS and NLOS scenarios of outdoor, industrial, office, and residential environments using the demonstrator. The pathloss model, the large scale fading, and the RMS delay spread have been determined. It has been shown that all parameters are strongly dependent on the scenario. These measurements form a database for the other analyses.

7.4 The System-Level Simulator for Positioning and Tracking (U-SPOT)

The final outcome of this thesis is the System-Level Simulator for Positioning and Tracking (U-SPOT). The simulator implements all stages of influence of a positioning systems and is intended to show the effect of specific system parameter settings and algorithms on the total localization system performance using Monte Carlo simulations. The simulator is based on statistically defined environments, where the probability for a LOS link can be defined by the user. A novel scheduling algorithm selects appropriate measured channel impulse responses from a database.

In this work, the simulator is used to compare specific localization methods for a user defined trajectory. Tracking-based localization methods can significantly improve the reliability of the position estimates. It is shown, that the performance of the coherent receiver and the energy detector is very similar for low ratios of NLOS links. A performance gain for the coherent receiver can only be achieved for higher NLOS ratios due to the better noise performance. On the other hand the performance of both receivers drops at high NLOS ratios.

The simulator is a powerful tool and allows for many more analyses. E.g. there exist many Kalman filter engineering approaches or particle filters, which may lead to better tracking robustness for high NLOS ratios; Or the analysis for algorithms to weight or reject weak link connections for LS-positioning, etc.

7.5 Key Outcomes of the Thesis and Implemented Tools

The following analysis tools have been created during the PhD Thesis:

- A UWB demonstrator system, that implements the IEEE 802.15.4a standard and satisfies the FCC/CEPT regulations
- A measurement database of the received IEEE 802.15.4a signals and the corresponding channel responses
- A large-scale channel model for indoor and outdoor environments
- A signal and statistical model of the energy detector for ranging in IEEE 802.15.4a, including IPI and the non-linear noise characteristic
- A signal and statistical model of the coherent receiver for ranging in IEEE 802.15.4a
- An analytical model for maximum operating distance estimation for ranging is shown, including a link budget and modeling of the FCC/CEPT regulations
- A UWB System-Level Simulator for Positioning and Tracking (U-SPOT)

A

UWB Demonstrator for Pseudo Real-Time Positioning

Figure A.1 shows the UWB demonstrator system for pseudo real-time positioning. The system is based on the demonstrator of Chapter 2, but shows two additional receiver paths. The three receiver paths can be used as base stations and the coordinates of the mobile can be estimated in 2D. As the system allows only one-way communication, time difference of arrival (TDoA) has been implemented for the positioning. In TDoA all base stations have to be synchronized, which is easily achieved in the current setup only requires calibration for the cable delays. The data transfer time from the oscilloscope to the PC depends on the length of the measurements (data signals) and can take up to several tens of seconds[1]. Hence, and as most of the processing is done offline, the system is called "pseudo real-time" localization system.

As there is no synchronization between pulse transmission and data capturing, the oscilloscope triggers at random times[2]. The time window of the oscilloscope is chosen that always a full signal is included in the measurements. In the next step the full signal has to be detected. For that, the signal is down-converted to baseband with an energy detector. The complete signal is detected by correlation with the synchronization header (SHR) preamble. The maximum peak of the correlated signal indicates the full signal (preamble). Thus, the measurements can be cutted according to the desired length and the broken signal is discarded.

The measurements are processed by an energy detector (see Figure 4.1), which is used for signal detection, despreading, and estimation of the channel response. The threshold-based ranging algorithm of Section 4.3 is applied for the estimation of the arrival time of the LOS component. As all base stations are synchronized, the TDoA between the base stations can be calculated and the coordinates of the transmitter are estimated. A detailed description and the experimental evaluation of the system are presented in [42].

Graphical User Interface

Figure A.2 shows the graphical user interface (GUI), which allows the user to control the system and to observe the results. The GUI allows the user to autoscale the oscilloscope, to reset the GUI, and to

[1] This value is given for $N_{\text{sync}} = 64$.

[2] The synchronization, shown in Figure A.1, is only for the synchronization of the laboratory equipment and not for the synchronization between transmitter and receiver (see Chapter 3).

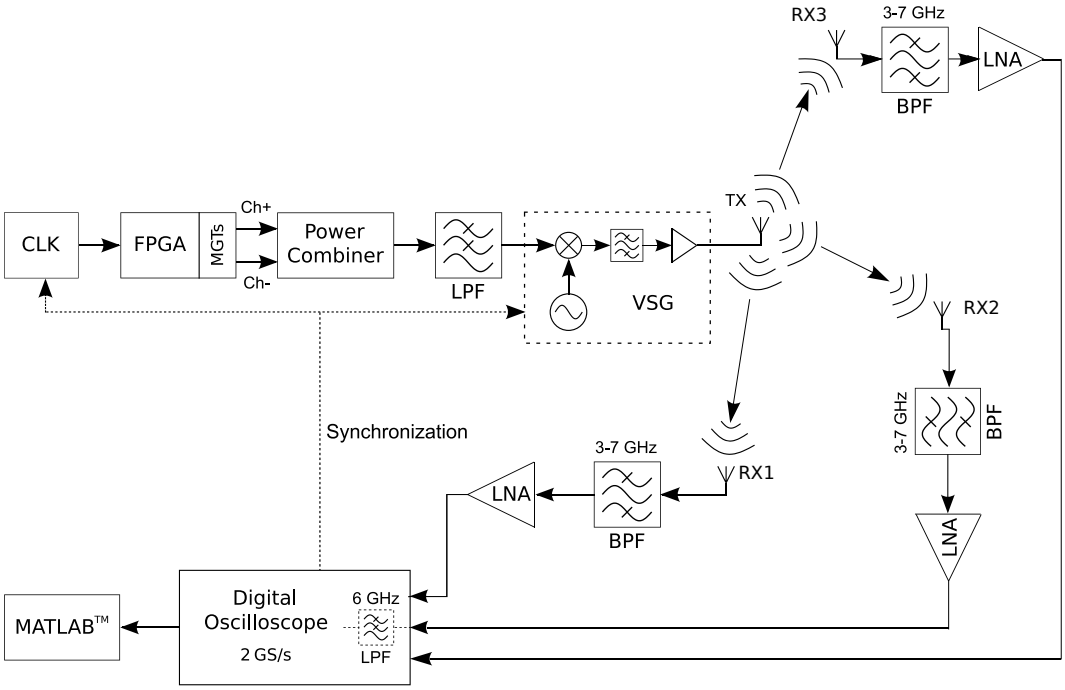

Figure A.1 UWB demonstrator for pseudo real-time positioning (cf. [42])

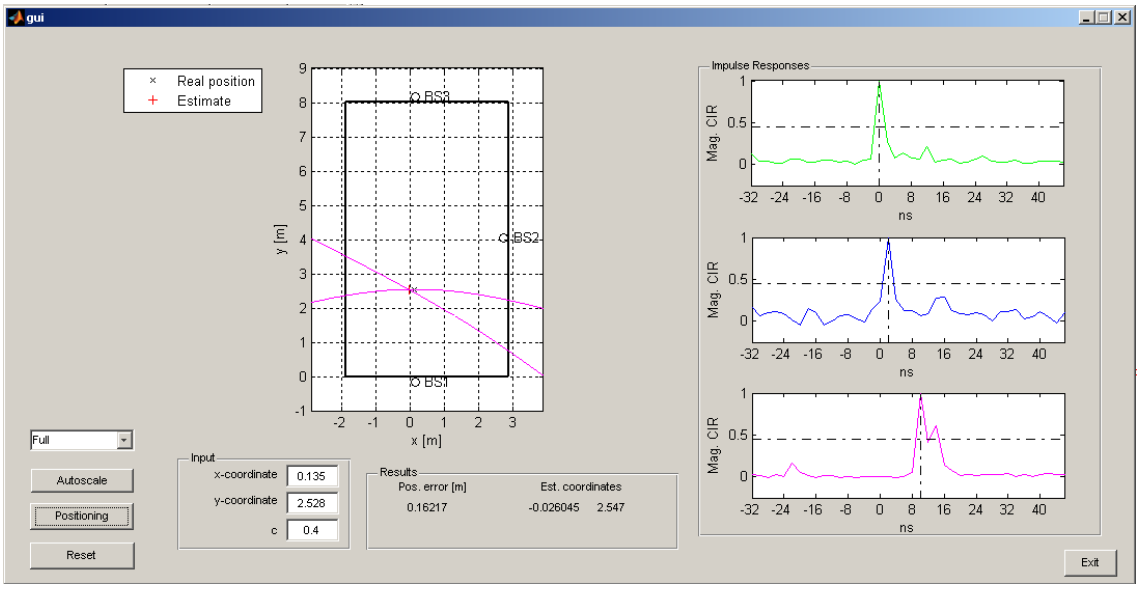

Figure A.2 GUI for UWB demonstrator

perform a position estimation. The real coordinates of the transmitter and the user defined threshold for the ranging algorithm c can be defined in the input block. The three estimated channel responses are shown on the right handside of the GUI. The ranging threshold and the detection point of the LOS component are also shown. The positioning scenario is depicted in the middle of the GUI, where BS1, BS2, and BS3 indicate the base stations. If the TDoA of two base stations is known, it is known that the mobile is on a hyperbola. In the given example the two estimated hyperbolas are depicted and the crossing point is the estimated location of the mobile. Finally, the positioning error and the estimated coordinates are shown.

B

Hardware Configuration and Practical Implementation

The hardware setup of the UWB demonstrator for ranging and channel estimation is shown in Figure B.1. The following list presents the used hardware components.

1. CLK: Stanford Research Systems - Modul CG635 (synchronized clock generator)
2. FPGA: Xilinx Virtex 2 pro - development board - CX2VP30
3. Power Combiner: Printed Circuit Board (PCB) design [25]
4. Attenuator: Mini Circuits 15542 VAT-10+
5. PCB: Pulse Shaping Filter [41]
6. VSG: Agilent PSG Vector Signal Generator E8267C
7. 1dB Step Attenuator: Agilent 8494B
8. Power Amplifier: Miteq AMF-3D-02001200-43-20P
9. 5-cent UWB-Antenna [86]
10. Skycross-Antenna SMT-3T010M
11. High Pass Filter (HPF): Mini Ciruits VHP-26
12. LNA: Narda DBS-0208N315
13. DSO: Agilent Infiniium 54855A

Figure 3.1 shows the principle setup of the demonstrator system, but some additional hardware components are necessary to improve the performance. The Attenuator 4 is used to reduce the effect of mismatches, between the power combiner 3 and the pulse shaping filter 5. The output power of the VSG is not sufficient to fully exploit the FCC and CEPT regulations, thus an external power amplifier 8 is needed after the VSG. Furthermore, the VSG output power is only tuneable in approx. 5 dB steps, thus an 1 dB step-wise attenuator 7 is used for precise calibration. Several antenna types are useable, where two types are depicted in the figure. The HPF and the Low-pass input filter of the DSO form together a bandpass filter from 3-6 GHz.

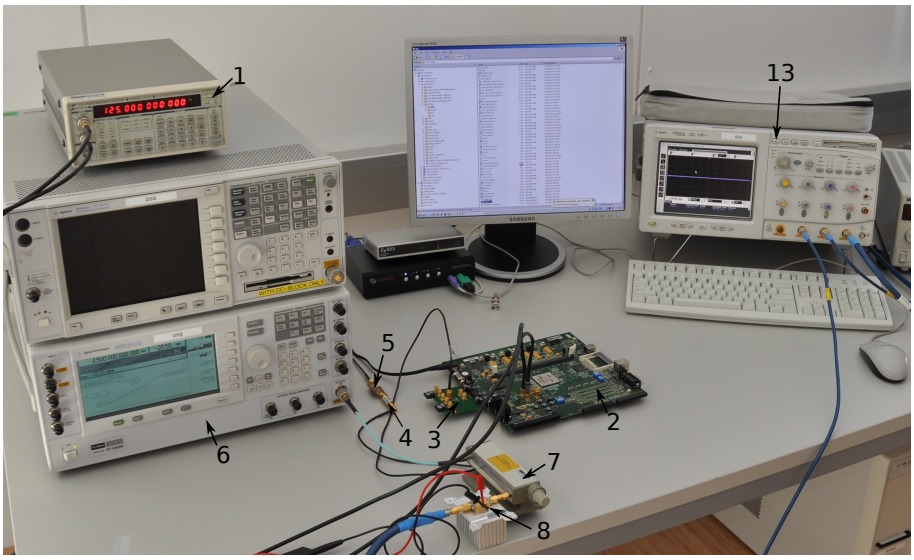

(a)

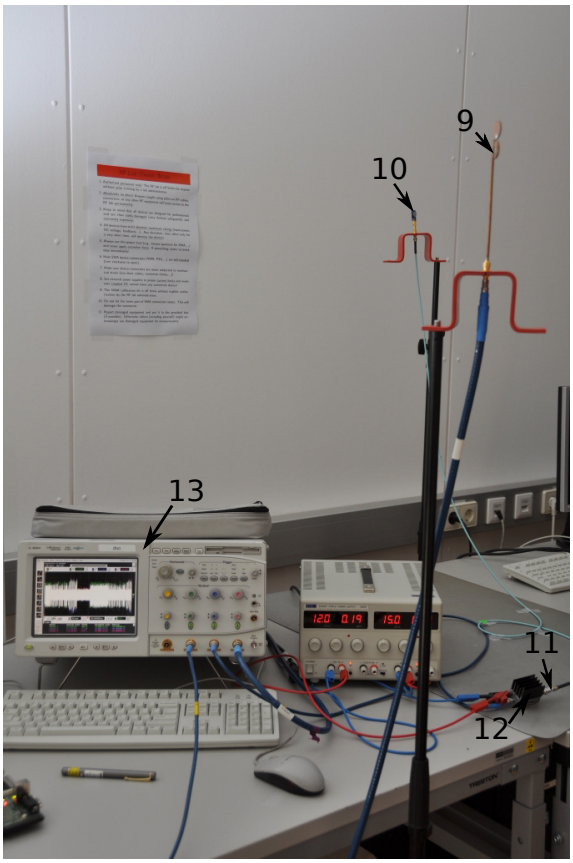

(b)

Figure B.1 UWB demonstrator for ranging and channel estimation - hardware setup: B.1(a) Transmitter B.1(b) Receiver

C

Coherent Receiver for Ranging

This section presents the signal model and the statistical analysis of the coherent receiver for ranging.

C.1 Signal Model

The analog received signal is given by (3.3). Then the signal is pulse matched filtered by $\tilde{w}(-t)$, where $\tilde{w}(t) = \tilde{w}(-t)$ due to symmetry. It follows that

$$r_{\mathrm{BP}}(t) = s(t) * h_c(t) * \tilde{w}(t) + \nu(t) * \tilde{w}(t). \tag{C.1}$$

Next, the negative frequencies are canceled by a Hilbert filter $h_{\mathrm{hilb}}(t)$ and the complex baseband signal is obtained by down-converting the signal with the estimated carrier frequency $\hat{\omega}_c$. The resulting baseband signal is given by

$$r(t) = (r_{\mathrm{BP}}(t) * h_{\mathrm{hilb}}(t))\; e^{-j(\hat{\omega}_c t + \varphi)}. \tag{C.2}$$

After sampling it follows

$$r(nT) = \sum_{m=0}^{M-1} c_m h(nT - mLT_{\mathrm{chip}}) e^{j[\omega_c - \hat{\omega}_c]nT} + \nu_{\mathrm{LP}}(nT) \tag{C.3}$$

where $h(t)$ is an equivalent channel response incorporating the channel $h_c(t)$, the unknown carrier phase φ, the pulse $\sqrt{E_p}w(t)$, and the downconverted matched filter $w(t)$. The noise $\nu_{\mathrm{LP}}[n]$ is the band limited input noise $\nu_{\mathrm{LP}}[n] = \nu[n] * w[n]$ in complex baseband. The carrier frequency is assumed to be known in this analysis. Thus, (C.3) simplifies to

$$r[n] = \sum_{m=0}^{M-1} c_m h[n - mLN_{\mathrm{chip}}] + \nu_{\mathrm{LP}}[n] \tag{C.4}$$

where $r[n]{=}r(nT)$. The number of samples within a chip is defined by $N_{\mathrm{chip}}{=}T_{\mathrm{chip}}/T$. Assuming synchronization, the estimation of the despread channel response $\hat{h}[n]$ is given by

$$\begin{aligned} \hat{h}[n] &= \sum_{q=0}^{N_{\mathrm{sync}}-1} \sum_{m=0}^{N_s-1} c_m\, r[n + (m + qN_s)LN_{\mathrm{chip}}] \\ &= M_1 h[n] + \sum_{m=0}^{M-1} c_m \nu_{\mathrm{LP}}[n + mLN_{\mathrm{chip}}] \end{aligned} \tag{C.5}$$

where the despreading is first performed sequence-wise ($\sum_m$) and then over the sequence repetitions ($\sum_q$). Since $c_m^2 = 1$ for the non-zero code elements, it follows that $\sum_q$ and $\sum_m$ is simply the number of non-zero code elements in the preamble, M_1. In other words, M_1 is the number of transmitted pulses. As the preamble codes show perfect circular autocorrelation properties, inter pulse interference (IPI) is canceled by despreading (see Section 3.4).

C.2 Statistical Analysis

The first and second-order statistics are analyzed in this section. The expected value of the despread channel response is obtained by

$$\begin{aligned} \mathrm{E}\Big\{\hat{h}[n]\Big\} &= M_1 h[n] + \sum_{m=0}^{M-1} c_m \mathrm{E}\{\nu_{\mathrm{LP}}[n + mLN_{\mathrm{chip}}]\} \\ &= M_1 h[n] \end{aligned} \tag{C.6}$$

due to the zero-mean noise term. The variance is given by

$$\begin{aligned} \mathrm{var}\Big\{\hat{h}[n]\Big\} =& \mathrm{E}\Big\{\hat{h}[n]\hat{h}^*[n]\Big\} - \mathrm{E}\Big\{\hat{h}[n]\Big\}\,\mathrm{E}\Big\{\hat{h}^*[n]\Big\} \\ =& \mathrm{E}\left\{\left(M_1 h[n] + \sum_{m=0}^{M-1} c_m \nu_{\mathrm{LP}}[n + mLN_{\mathrm{chip}}]\right)\left(M_1 h^*[n] + \sum_{m=0}^{M-1} c_m \nu_{\mathrm{LP}}^*[n + mLN_{\mathrm{chip}}]\right)\right\} \\ & - M_1^2 h[n]h^*[n] \\ =& M_1^2 h[n]h^*[n] + \sum_{m=0}^{M-1}\sum_{m'=0}^{M-1} c_m c_{m'} \mathrm{E}\{\nu_{\mathrm{LP}}[n + mLN_{\mathrm{chip}}]\nu_{\mathrm{LP}}^*[n + m'LN_{\mathrm{chip}}]\} \\ & + M_1 h[n] \sum_{m=0}^{M-1} c_m \underbrace{\mathrm{E}\{\nu_{\mathrm{LP}}^*[n + mLN_{\mathrm{chip}}]\}}_{=0} + M_1 h^*[n] \sum_{m=0}^{M-1} c_m \underbrace{\mathrm{E}\{\nu_{\mathrm{LP}}[n + mLN_{\mathrm{chip}}]\}}_{=0} \\ & - M_1^2 h[n]h^*[n] \\ =& \sum_{m=0}^{M-1}\sum_{m'=0}^{M-1} c_m c_{m'} \mathrm{E}\{\nu_{\mathrm{LP}}[n + mLN_{\mathrm{chip}}]\nu_{\mathrm{LP}}^*[n + m'LN_{\mathrm{chip}}]\}\,. \end{aligned} \tag{C.7}$$

The noise $\nu_{\mathrm{LP}}[n]$ is uncorrelated for samples spaced by $\geq LN_{\mathrm{chip}}$, thus it follows that $m' = m$ and (C.7) simplifies to

$$\mathrm{var}\Big\{\hat{h}[n]\Big\} = N_0 \sum_{m=0}^{M-1} c_m^2 \phi_w[0] = N_0 M_1. \tag{C.8}$$

It can be seen in (C.6) and (C.8), that signal amplitude and noise power scale with the number of transmitted pulses M_1.

D

Analyses of the Energy Detector

D.1 Covariance Terms

This section presents the proof for $\text{cov}\{y_{ss}, y_{s\nu}\} = \text{cov}\{y_{ss}, y_{\nu\nu}\} = \text{cov}\{y_{s\nu}, y_{\nu\nu}\} = 0$. First, the $\text{cov}\{y_{ss}, y_{s\nu}\}$ is given by

$$\text{cov}\{y_{ss}, y_{s\nu}\} = \text{E}\{(y_{ss}[n] - \bar{y}_{ss}[n])(y_{s\nu}[n] - \bar{y}_{s\nu}[n])\} \tag{D.1}$$

where $\bar{y}_{ss}[n] = \text{E}\{y_{ss}[n]\} = y_{ss}[n]$ due to y_{ss} is deterministic. The mean $\bar{y}_{s\nu}[n] = 0$, see (4.12). It follows that

$$\begin{aligned} \text{cov}\{y_{ss}, y_{s\nu}\} &= (y_{ss}[n] - y_{ss}[n])\text{E}\{(y_{s\nu}[n]\} \\ &= 0\,. \end{aligned} \tag{D.2}$$

As the deterministic part also occurs in $\text{cov}\{y_{ss}, y_{\nu\nu}\}$, it implies that $\text{cov}\{y_{ss}, y_{\nu\nu}\} = 0$. The last covariance is also zero, because simulations have shown that $y_{s\nu}$ and $y_{\nu\nu}$ are independent.

D.2 Expected Value of Filtered White Gaussian Noise

This section shows the derivation of $\text{E}\{\nu_{\text{BP}}(t)\nu_{\text{BP}}(t')\} = N_0/2\phi_h(\epsilon)$, where ν_{BP} is filtered white Gaussian noise $\nu_{\text{BP}} = \nu(t) * h(t)$ and $\phi_h(\epsilon)$ is the autocorrelation function of the filter $h(t)$.

$$\begin{aligned} \text{E}\{\nu_{\text{BP}}(t)\nu_{\text{BP}}(t')\} &= \text{E}\left\{ \int_{-\infty}^{\infty} \int_{-\infty}^{\infty} \nu(\tau)h(t-\tau)\nu(\tau')h(t'-\tau')d\tau d\tau' \right\} \\ &= \int_{-\infty}^{\infty} \int_{-\infty}^{\infty} \text{E}\{\nu(\tau)\nu(\tau')\}\, h(t-\tau)h(t'-\tau')d\tau d\tau'. \end{aligned} \tag{D.3}$$

As $\nu(t)$ is uncorrelated, it follows $E\{\nu(\tau)\nu(\tau')\} = N_0/2\delta(\tau - \tau')$, where $N_0/2$ is the two sided noise spectral density. Thus, $\tau' = \tau$ and $\text{E}\{\nu^2(\tau)\} = N_0/2$. Thus, (D.3) simplifies to

$$\text{E}\{\nu_{\text{BP}}(t)\nu_{\text{BP}}(t')\} = \frac{N_0}{2} \int_{-\infty}^{\infty} h(t-\tau)h(t'-\tau)d\tau. \tag{D.4}$$

With $t' = t + \epsilon$ this can be rewritten as

$$\begin{aligned} \mathrm{E}\{\nu_{\mathrm{BP}}(t)\nu_{\mathrm{BP}}(t+\epsilon)\} &= \frac{N_0}{2} \int_{-\infty}^{\infty} h(t-\tau)h(t+\epsilon-\tau)d\tau \\ &= \frac{N_0}{2}\phi_h(\epsilon). \end{aligned} \tag{D.5}$$

Finally, if $t = t'$, which implies $\epsilon = 0$, then (D.5) simplifies further to

$$\mathrm{E}\{\nu_{\mathrm{BP}}(t)\nu_{\mathrm{BP}}(t)\} = \frac{N_0}{2}\phi_h(0) \tag{D.6}$$

where $\phi_h(0)$ is the equivalent bandwidth of the filter.

D.3 IPI-Free Statistics of the Energy Detector

This section shows the derivation of the first and second-order statistics of the energy detector without inter pulse interference (IPI). Starting from (4.3), the expected value $\mathrm{E}\{y[n]\} = \mathrm{E}\{y_{ss}[n]\}+\mathrm{E}\{y_{s\nu}[n]\}+\mathrm{E}\{y_{\nu\nu}[n]\}$ and the variance $\mathrm{var}\{y[n]\} = \mathrm{var}\{y_{ss}[n]\}+\mathrm{var}\{y_{s\nu}[n]\}+\mathrm{var}\{y_{\nu\nu}[n]\}$, because all covariance terms are zero.

D.3.1 Signal-by-Signal Term $y_{ss}[n]$

$y_{ss}[n]$ is the deterministic part of the signal, thus $\mathrm{E}\{y_{ss}[n]\} = y_{ss}[n]$ and $\mathrm{var}\{y_{ss}[n]\} = 0$. It is assumed for simplicity that the code appears circularly and the sidelobes at the beginning and the end of the correlation sequence are ignored. Thus, the first sum in (4.3) simplifies to a factor of N_{sync} and

$$y_{ss}[n] = N_{\mathrm{sync}} \sum_{i=0}^{N_s-1} \sum_{m=0}^{M-1} \sum_{k=-m}^{M-m-1} c_m c_{(m+k)} \tilde{c}_i \int_{nT_I}^{(n+1)T_I} g(t-(m-i)LT_{\mathrm{chip}})g(t-(m+k-i)LT_{\mathrm{chip}})dt. \tag{D.7}$$

Assuming the IPI-free case, the delay $k = 0$ and due to the perfect circular autocorrelation properties, $i = m$. Thus, it follows

$$y_{ss}[n] = N_{\mathrm{sync}} \sum_{m=0}^{N_s-1} c_m^2 \tilde{c}_m \int_{nT_I}^{(n+1)T_I} g^2(t)dt \ . \tag{D.8}$$

We are considering only the LOS component for this analysis, thus $g(t) = \sqrt{E_{\mathrm{LOS}}^{(1)}}\phi_{\tilde{w}}(t)$. As only the non-zero-coded elements contribute, (D.8) reduces to

$$y_{ss}[n] = E_{\mathrm{LOS}}^{(1)} N_{\mathrm{sync}} \frac{N_s+1}{2} \int_{nT_I}^{(n+1)T_I} \phi_{\tilde{w}}^2(t)dt. \tag{D.9}$$

Assuming $y_{ss}[n_{\mathrm{LOS}}]$ contains approx. the entire pulse, where n_{LOS} is the sample containing the LOS component, it follows that $\int_{nT_I}^{(n+1)T_I} \phi_{\tilde{w}}^2(t)dt \approx 1$ and

$$y_{ss}[n_{\mathrm{LOS}}] \approx E_{\mathrm{LOS}}. \tag{D.10}$$

D.3.2 Signal-by-Noise $y_{s\nu}[n]$

As shown in (4.12) $\mathrm{E}\{y_{s\nu}[n]\}=0$, because the noise term is zero mean. Thus, $\mathrm{var}\{y_{s\nu}[n]\} = \mathrm{E}\{y_{s\nu}^2[n]\}$ and

$$\begin{aligned}\mathrm{var}\{y_{s\nu}[n]\} = 4 \sum_{q=0}^{N_{\mathrm{sync}}-1} \sum_{q'=0}^{N_{\mathrm{sync}}-1} \sum_{i=0}^{N_s-1} \sum_{i'=0}^{N_s-1} \sum_{m=0}^{N_s-1} \sum_{k=-m}^{M-m-1} c_m c_{(m+k)} \tilde{c}_i \tilde{c}_{i'} \int_{nT_I}^{(n+1)T_I} \int_{nT_I}^{(n+1)T_I} \\ \times g(t+(i-m)LT_{\mathrm{chip}}+qT_{\mathrm{psym}}) g(\tau+(i'-m-k)LT_{\mathrm{chip}}+q'T_{\mathrm{psym}}) \\ \times \mathrm{E}\{\nu_{\mathrm{BP}}(t+iLT_{\mathrm{chip}}+qT_{\mathrm{psym}}) \nu_{\mathrm{BP}}(\tau+i'LT_{\mathrm{chip}}+q'T_{\mathrm{psym}})\}\, d\tau\, dt\,.\end{aligned} \tag{D.11}$$

The noise is uncorrelated for a time delay of (a multiple of) T_{psym}, which forces $q{=}q'$ and $\sum_q(...){=}N_{\mathrm{sync}} \times (...)$. Furthermore, the noise is also uncorrelated for a lag of (a multiple of) LT_{chip}. Hence it follows that $i = i'$. $\tilde{c}_i{}^2 = 1$, because $\tilde{c}_i \in \{1, -1\}$. By substituting $\tau = t + \mu$ and using $E\{\nu_{\mathrm{BP}}(t)\nu_{\mathrm{BP}}(t+\mu)\} = N_0/2\, \phi_{\tilde{w}}(\mu)$, (D.11) reduces to

$$\begin{aligned}\mathrm{var}\{y_{s\nu}[n]\} =& 2N_0 N_{\mathrm{sync}} \sum_{i=0}^{N_s-1} \sum_{m=0}^{M-1} \sum_{k=-m}^{M-m-1} c_m c_{(m+k)} \int_{nT_I}^{(n+1)T_I} \int_{nT_I-t}^{(n+1)T_I-t} g(t+(i-m)LT_{\mathrm{chip}}) \\ &\times g(t+\mu+(i-m-k)LT_{\mathrm{chip}})\, \phi_{\tilde{w}}(\mu)\, d\mu\, dt\,.\end{aligned} \tag{D.12}$$

Defining $l = i - m$ and substituting m, the integrals become independent of i. Next, the perfect autocorrelation properties of $\mathbf{c}$ are used, thus the term is only non-zero at $k = 0$. This also means that the signal-by-noise term does not depend on sidelobes of the code despreading or the channel correlation function. Thus, (D.12) further reduces to

$$\mathrm{var}\{y_{s\nu}[n]\} = 2N_0 N_{\mathrm{sync}} \sum_{i=0}^{N_s-1} \sum_{l=i}^{M+i-1} c_{(i-l)}^2 \int_{nT_I}^{(n+1)T_I} \int_{nT_I-t}^{(n+1)T_I-t} g(t+lLT_{\mathrm{chip}}) g(t+\mu+lLT_{\mathrm{chip}})\, \phi_{\tilde{w}}(\mu)\, d\mu\, dt \tag{D.13}$$

It can be shown, that $\int\int g(t)g(t+\mu)\phi_{\tilde{w}}(\mu)\, dt\, d\tau \approx \int \tilde{g}^2(t)dt$, where $\tilde{g}(t) = g(t) * \tilde{w}(-t)$ (see Section 4.2.2). Furthermore, $\tilde{g}(t) \approx g(t)$, since the bandwidth of the pulse shape is equal to the bandwidth of the input filter. Thus, (D.13) can be approximated by

$$\mathrm{var}\{y_{s\nu}[n]\} \approx 2N_0 N_{\mathrm{sync}} \sum_{i=0}^{N_s-1} \sum_{l=i}^{M+i-1} c_{(i-l)}^2 \int_{nT_I}^{(n+1)T_I} g^2(t+lLT_{\mathrm{chip}}) dt \tag{D.14}$$

Assuming the IPI free case, $l{=}0$ and considering only the LOS component it follows

$$\mathrm{var}\{y_{s\nu}[n]\} \approx E_{\mathrm{LOS}}^{(1)} (N_s+1) N_{\mathrm{sync}} N_0 \int_{nT_I}^{(n+1)T_I} \phi_{\tilde{w}}^2(t) dt \tag{D.15}$$

For n_{LOS}, (D.15) simplifies to

$$\mathrm{var}\{y_{s\nu}[n_{\mathrm{LOS}}]\} \approx 2E_{\mathrm{LOS}} N_0 \tag{D.16}$$

D.3.3 Noise-by-Noise Term $y_{\nu\nu}[n]$

This term is analyzed in Section 4.2.3.

D.4 Maximal Operating Distance Estimation

The maximal operating distance is given by

$$d_{\max} = \left(\frac{\frac{E_{\mathrm{LOS}}}{N_0}(1\mathrm{m}, f_c)}{\frac{E_{\mathrm{LOS}}}{N_0}(d_{\max}, f_c)} \right)^{1/\eta}. \tag{D.17}$$

As the working point is defined with LSNR, $E_{\mathrm{LOS}}/N_0(d_{\max})$ has to be substituted with $\mathrm{LSNR}_{\mathrm{WP}}$. The input to output SNR relation is given by

$$\mathrm{LSNR}_{\mathrm{WP}} = \frac{2\left(\frac{E_{\mathrm{LOS}}}{N_0}(d_{\max}, f_c)\right)^2}{4\frac{E_{\mathrm{LOS}}}{N_0}(d_{\max}, f_c) + \mathrm{ND}} \tag{D.18}$$

and can be rewritten to

$$\left(\frac{E_{\mathrm{LOS}}}{N_0}(d_{\max}, f_c)\right)^2 \underbrace{-2\mathrm{LSNR}_{\mathrm{WP}}}_{=p} \frac{E_{\mathrm{LOS}}}{N_0}(d_{\max}, f_c) \underbrace{-\frac{1}{2}\mathrm{ND} \cdot \mathrm{LSNR}_{\mathrm{WP}}}_{=q} = 0. \tag{D.19}$$

This quadratic equation can be solved with $x_{1,2} = p/2 \pm \sqrt{(p/2)^2 - q}$ and it follows

$$\frac{E_{\mathrm{LOS}}}{N_0}(d_{\max}, f_c) = \mathrm{LSNR}_{\mathrm{WP}} \pm \sqrt{\mathrm{LSNR}_{\mathrm{WP}}^2 + \mathrm{LSNR}_{\mathrm{WP}} \cdot \mathrm{ND}/2}. \tag{D.20}$$

As the part within the square root is always greater than LSNR and $\frac{E_{\mathrm{LOS}}}{N_0}(d_{\max}) \geq 0$, the second solution can be dropped and (D.21) reduces to

$$\frac{E_{\mathrm{LOS}}}{N_0}(d_{\max}, f_c) = \mathrm{LSNR}_{\mathrm{WP}} + \sqrt{\mathrm{LSNR}_{\mathrm{WP}}(\mathrm{LSNR}_{\mathrm{WP}} + \mathrm{ND}/2)}. \tag{D.21}$$

Finally, the maximal operating distance for the energy detector is obtained by using (D.17) and (D.21) and it follows

$$d_{\max} = \left(\frac{\frac{E_{\mathrm{LOS}}}{N_0}(1\mathrm{m}, f_c)}{\mathrm{LSNR}_{\mathrm{WP}} + \sqrt{\mathrm{LSNR}_{\mathrm{WP}}\left(\mathrm{LSNR}_{\mathrm{WP}} + \mathrm{ND}/2\right)}} \right)^{1/\eta}. \tag{D.22}$$

Curriculum Vitae

Personal details	
Name	Dipl.-Ing. ***Thomas Gigl***, Bakk. techn.
Date of birth	16.04.1979
Place of birth	Weiz (Austria)
Nationality	Austrian

Education	
Since 2007	***PhD Student of Electrical Engineering*** Graz University of Technology, Austria, Signal Processing and Speech Communication Laboratory (SPSC)
2006	***Master Thesis*** Delft University of Technology, the Netherlands Wireless and Mobile Communications Group Duration 6 Months, in cooperation with the SPSC
2004-2006	***Master programme Telematics***[a] Graz University of Technology Specialization: Telecommunications and Mobile Computing Graduated with distinction
1999-2004	***Bachelor programme Telematics*** Graz University of Technology
1993-1998	***Technical college for industrial engineering and management (A-Level)*** HTBLA Weiz

[a] Telecommunications and Computer Science

Experience	
Since 2007	***Research Assistant*** Graz University of Technology, SPSC
Since 2007	***System and Application Engineer*** CISC Semiconductor
2005-2006	***Project Employee*** CISC Semiconductor
2000-2004	***Student Employee*** Andritz VA Tech Hydro / VA Tech ELIN EBG IT - Networking Division / Electrical Calculation Division
Publications	
Papers	***14 published papers*** (see Table 1.1)
Plenary talk	"Real Time Locating Systems Using Ultra Wideband Signals" International Conference of Impact on Ubiquitous IT Co-Design to Industry, Korean and Australian Conference Alliances (KOALA 2010), Perth, Australia, 2010
Talks	Several presentations on international and national conferences and standardization meetings
Awards	
2010	***IEEE Outstanding Best Paper Award*** International Conference of Impact on Ubiquitous IT Co-Design to Industry, Korean and Australian Conference Alliances (KOALA 2010), Perth, Australia, 2010
2009	***Best Student Award*** 4th IEEE UWB Forum on Sensing and Communications, TU Vienna won by Bernhard Geiger (advised by Thomas Gigl)
2009	***IEEE 2009 Region 8 Student Paper Competition*** won by Bernhard Geiger (advised by Thomas Gigl)
Standardization	
ISO	Member of the standardization group ISO/IEC JTC1/SC31/WG5- Real Time Localization Systems (RTLS)
EPCglobal	Member of the Hardware Action Group Active Tagging (HAT) ad hoc Committee

Bibliography

[1] Z. Sahinoglu, S. Gezici, and I. Guvenc, *Ultra-wideband Postioning Systems*. Cambridge University Press, 2008.

[2] D. Harmer, M. Russell, E. Frazer, T. Bauge, S. Ingram, N. Schmidt, B. Kull, A. Yarovoy, A. Nezirovic, L. Xia, V. Dizdarevic, and K. Witrisal, "EUROPCOM: Emergency Ultrawideband RadiO for Positioning and COMmunications," in *Ultra-Wideband, 2008. ICUWB 2008. IEEE International Conference on*, 2008, pp. 85 –88.

[3] J. Rantakokko, P. Händel, and M. Fredholm, "User Requirements for Localization and Tracking Technology," in *Indoor Positioning and Indoor Navigation, IPIN 2010, International Conference on*, Sept. 2010, pp. 221–222.

[4] A. Molisch, P. Orlik, Z. Sahinoglu, and J. Zhang, "UWB-based sensor networks and the IEEE 802.15.4a standard - a tutorial," in *Communications and Networking in China, 2006. ChinaCom '06. First International Conference on*, 2006, pp. 1 –6.

[5] *Revision of part 15 of the commission's rules regarding ultra-wideband transmission systems*, FCC, First Report and Order, ET-Docket 98-153, FCC 02-28 Std., 2002.

[6] M. Win, D. Dardari, A. Molisch, W. Wiesbeck, and J. Zhang, "History and Applications of UWB," *Proceedings of the IEEE*, vol. 97, no. 2, pp. 198 –204, feb. 2009.

[7] M. Chiani and A. Giorgetti, "Coexistence Between UWB and Narrow-Band Wireless Communication Systems," *Proceedings of the IEEE*, vol. 97, no. 2, pp. 231 –254, feb. 2009.

[8] *ECMA-368: High Rate Ultra Wideband PHY and MAC Standard*, ECMA international Std. 3, 2008.

[9] *ECMA-369: MAC-PHY Interface for ECMA-368*, ECMA international Std. 3, 2008.

[10] M. Win and R. Scholtz, "Impulse radio: how it works," *Communications Letters, IEEE*, vol. 2, no. 2, pp. 36 –38, feb 1998.

[11] J. Ryckaert, M. Badaroglu, C. Desset, V. De Heyn, G. ven der Plas, P. Wambacq, B. van Poucke, and S. Donnay, "Carrier-based UWB impulse radio: simplicity, flexibility, and pulser implementation in 0.18-micron CMOS," in *Ultra-Wideband, 2005. ICUWB 2005. 2005 IEEE International Conference on*, sep. 2005, pp. 432 – 437.

[12] F. Troesch, "Novel Low Duty Cycle Schemes: From Ultra Wide Band to Ultra Low Power," Ph.D. dissertation, ETH Zurich, 2010.

[13] C. Duan, P. Orlik, Z. Sahinoglu, and A. Molisch, "A Non-Coherent 802.15.4a UWB Impulse Radio," in *Ultra-Wideband, 2007. ICUWB 2007. IEEE International Conference on*, 2007, pp. 146 –151.

[14] K. Witrisal, G. Leus, G. Janssen, M. Pausini, F. Troesch, T. Zasowski, and J. Romme, "Noncoherent ultra-wideband systems," *Signal Processing Magazine, IEEE*, vol. 26, no. 4, pp. 48–66, july 2009.

[15] *Information technology - Real Time Locating Systems (RTLS) - Part 2: 2.4 GHz air interface*, ISO/IEC 24730-2 Std., 2006.

[16] WhereTag IV Model TFF-2000 - DataSheet. Zebra Technologies Corporation. Seen Aug. 2010. [Online]. Available: http://www.zebra.com

[17] *Information technology - Real Time Locating Systems (RTLS) - Part 5: Chirp spread spectrum (CSS) at 2.4 GHz air interface*, ISO/IEC 24730-5 Std., 2008.

[18] Data sheet: nanoLOC TRX Transceiver. Nanotron Technologies GmbH. Seen Aug. 2010. [Online]. Available: http://www.nanotron.com

[19] i-Q350 RTLS - DataSheet. Identec Solutions AG. Seen Aug. 2010. [Online]. Available: http://www.identecsolutions.com

[20] *Part 15.4: Wireless Medium Access Control (MAC) and Physical Layer (PHY) Specifications for Low-Rate Wireless Personal Area Networks (WPANs), Amendment 1: Add Alternate PHYs*, IEEE Std., 2007.

[21] *Part 15.4: Wireless Medium Access Control (MAC) and Physical Layer (PHY) Specifications for Low-Rate Wireless Personal Area Networks (WPANs)*, IEEE Std., 2006.

[22] ScenSor, Advanced Product Information DW4aSS1000. Decawave. Seen Aug. 2010. [Online]. Available: http://www.decawave.com

[23] Ubisense UWB Real Time Locating System. Ubisense. Seen Nov. 2010. [Online]. Available: http://www.ubisense.net

[24] Ekahau WLAN Real Time Locating System. Ekahau. Seen Nov. 2010. [Online]. Available: http://www.ekahau.com

[25] S. Egger, "UWB Demonstrator with Scope on Synchronisation," in *Diploma Thesis, Graz Univerisity of Technology*, 2007.

[26] Overview of IEEE 802.15 WPAN Low Rate Alternative PHY Task Group 4a (TG4a). IEEE. Seen Oct. 2010. [Online]. Available: http://www.ieee802.org/15/pub/TG4a.html

[27] Y. Qi and H. Kobayashi, "On relation among time delay and signal strength based geolocation methods," in *Global Telecommunications Conference, 2003. GLOBECOM '03. IEEE*, vol. 7, dec. 2003, pp. 4079–4083.

[28] Z. Sahinoglu and S. Gezici, "Ranging in the IEEE 802.15.4a Standard," in *Wireless and Microwave Technology Conference, 2006. WAMICON '06. IEEE Annual*, 4-5 2006, pp. 1 –5.

[29] J. Reed, *Introduction to ultra wideband communication systems*. Prentice Hall Press, 2005.

[30] *Commission Decision of 21 February 2007: On allowing the use of the radio spectrum for equipment using Ultra-wideband technology in a harmonized manner in the community*, EC, Official Journal of the European Union L 55/33 Std., Feb. 2007.

[31] *Commission Decision of 21 April 2009: amending Decision 2007/131/EC on allowing the use of the radio spectrum for equipment using ultra-wideband technology in a harmonised manner in the community*, EC, Official Journal of the European Union L 105/9 Std., April 2009.

[32] ACMA, "Planning for Ultra-Wideband (UWB)," Australian Communications and Media Authority (ACMA), Tech. Rep., 2010. [Online]. Available: http://www.acma.gov.au/WEB/STANDARD/pc=PC_312114

[33] N. Guo, J. Zhang, P. Zhang, Z. Hu, Y. Song, and R. Qiu, "UWB Real-time testbed with waveform-based precoding," in *Military Communications Conference, 2008. MILCOM 2008. IEEE*, 2008, pp. 1 –7.

[34] L. Stoica, A. Rabbachin, and I. Oppermann, "A low-complexity noncoherent IR-UWB transceiver architecture with TOA estimation," *Microwave Theory and Techniques, IEEE Transactions on*, vol. 54, no. 4, pp. 1637 –1646, june 2006.

[35] G. George, X. Artiga, A. Moragrega, C. Ibars, and M. di Renzo, "Flexible FPGA-DSP solution for an IR-UWB testbed," in *Ultra-Wideband, 2009. ICUWB 2009. IEEE International Conference on*, 2009, pp. 413 –417.

[36] A. Mallat, P. Gerard, M. Drouguet, F. Keshmiri, C. Oestges, C. Craeye, D. Flandre, and L. Vandendorpe, "Testbed for IR-UWB based ranging and positioning: Experimental performance and comparison to CRLBs," in *Wireless Pervasive Computing (ISWPC), 2010 5th IEEE International Symposium on*, 2010, pp. 163 –168.

[37] A. Mollfulleda, M. Najar, P. Miskovsky, J. Leyva, L. Berenguer, C. Ibars, and M. Navarro, "QUETZAL: qualified ultra-wideband testbed for reduced data-rates and location," in *Testbeds and Research Infrastructures for the Development of Networks and Communities, 2006. TRIDENTCOM 2006. 2nd International Conference on*, 2006, pp. 7 –191.

[38] A. Adalan, T. Gigl, M. Fischer, and K. Witrisal, "A modular impulse radio ultra-wideband research & development platform for IEEE802.15.4a," in *Wireless Technology Conference, 2009. EuWIT 2009. European*, Sept. 2009, pp. 116–119.

[39] T. Gigl, T. Buchgraber, A. Adalan, J. Preishuber-Pfluegl, M. Fischer, and K. Witrisal, "UWB channel characterization using IEEE 802.15.4a demonstrator system," in *Ultra-Wideband, 2009. ICUWB 2009. IEEE International Conference on*, Sept. 2009, pp. 230–234.

[40] T. Buchgraber, "Experimental Evaluation of the IEEE 802.15.4a Standard," in *Diploma Thesis, Graz Univerisity of Technology*, 2008.

[41] A. Adalan, M. Fischer, T. Gigl, K. Witrisal, A. Scholtz, and C. Mecklenbrauker, "Ultra-Wideband Radio Pulse Shaping Filter Design for IEEE 802.15.4a Transmitter," in *Wireless Communications and Networking Conference, 2009. WCNC 2009. IEEE*, April 2009, pp. 1–6.

[42] J. B. Till, "IEEE 802.15.4a-UWB compliant Positioning using Energy Detectors," in *Master Thesis, Graz Univerisity of Technology*, 2010.

[43] T. Gigl, J. Preishuber-Pfluegl, D. Arnitz, and K. Witrisal, "Experimental characterization of ranging in IEEE802.15.4a using a coherent reference receiver," in *Personal, Indoor and Mobile Radio Communications, 2009 IEEE 20th International Symposium on*, Sept. 2009, pp. 92–96.

[44] Y.-S. Kwok, F. Chin, and X. Peng, "Ranging Mechanism, Preamble Generation, and Performance with IEEE 802.15.4a Low-Rate Low-Power UWB Systems," in *Spread Spectrum Techniques and Applications, 2006 IEEE Ninth International Symposium on*, 2006, pp. 430–434.

[45] Z. Irahhauten, G. Janssen, H. Nikookar, A. Yarovoy, and L. Ligthart, "UWB Channel Measurements and Results for Office and Industrial Environments," in *Ultra-Wideband, IEEE 2006 International Conference on*, 2006, pp. 225 –230.

[46] T. S. Rappaport, *Wireless Communications: Principles and Practice*, 2nd ed. Prentice Hall, 2002.

[47] A. F. Molisch, *Wireless Communications*. John Wiley & Sons Ltd., 2005.

[48] D. Cox, "Delay Doppler characteristics of multipath propagation at 910 MHz in a suburban mobile radio environment," *Antennas and Propagation, IEEE Transactions on*, vol. 20, no. 5, pp. 625–635, Sep 1972.

[49] T. Gigl, T. Buchgraber, B. Geiger, A. Adalan, J. Preishuber-Pfluegl, and K. Witrisal, "Pathloss and Delay-Spread Analysis of Multipath Intensive Environments using IEEE 802.15.4a UWB Signals," in *COST2100 Management Committee Meeting*, Sept. 2009.

[50] H. Urkowitz, "Energy detection of unknown deterministic signals," *Proceedings of the IEEE*, vol. 55, no. 4, pp. 523 – 531, apr. 1967.

[51] S. Dubouloz, B. Denis, S. de Rivaz, and L. Ouvry, "Performance analysis of LDR UWB non-coherent receivers in multipath environments," in *Ultra-Wideband, 2005. ICUWB 2005. 2005 IEEE International Conference on*, Sept. 2005.

[52] I. Guvenc and Z. Sahinoglu, "Threshold-based TOA estimation for impulse radio UWB systems," in *Ultra-Wideband, 2005. ICUWB 2005. 2005 IEEE International Conference on*, Sept. 2005, pp. 420–425.

[53] D. Dardari, A. Conti, U. Ferner, A. Giorgetti, and M. Win, "Ranging With Ultrawide Bandwidth Signals in Multipath Environments," *Proceedings of the IEEE*, vol. 97, no. 2, pp. 404–426, feb. 2009.

[54] H. Luecken, C. Steiner, and A. Wittneben, "ML timing estimation for generalized UWB-IR energy detection receivers," in *Ultra-Wideband, 2009. ICUWB 2009. IEEE International Conference on*, sep. 2009, pp. 829 –833.

[55] B. Geiger, "Enhanced Accuracy Channel Estimation and Ranging for Energy Detectors," Diploma Thesis, Graz University of Technology, 2009.

[56] B. C. Geiger, T. Gigl, and K. Witrisal, "Enhanced-Accuracy Channel Estimation and Ranging for IR-UWB Energy Detectors," in *Ultra-Wideband, 2010. ICUWB 2010. IEEE International Conference on*, Sept. 2010, pp. 513–518.

[57] T. Gigl, F. Troesch, J. Preishuber-Pfluegl, and K. Witrisal, "Maximal Operating Distance Estimation for Ranging in IEEE 802.15.4a Ultra Wideband," in *Positioning, Navigation and Communication, 2010 7th Workshop on*, March 2010, p. in press.

[58] B. Geiger, "Ranging in the IEEE 802.15.4a standard using energy detectors," in *EUROCON 2009, EUROCON '09. IEEE*, 2009, pp. 1956 –1963.

[59] T. Gigl, J. Preishuber-Pfluegl, and K. Witrisal, "Statistical analysis of a UWB energy detector for ranging in IEEE 802.15.4a," in *Ultra-Wideband, 2009. ICUWB 2009. IEEE International Conference on*, Sept. 2009, pp. 129–134.

[60] D. G. Manolakis, V. K. Ingle, and S. Kogon, *Statistical and Adaptive Signal Processing*. Artech House, 2005.

[61] V. Dizdarevic and K. Witrisal, "Statistical UWB range error model for the threshold leading edge detector," in *Proc. 6th International Conference on Information, Communications & Signal Processing*, Dec. 2007, pp. 1–5.

[62] B. Geiger, T. Gigl, J. Preishuber-Pfluegl, and K. Witrisal, "Experimental Characterization of System Parameters for Ranging in IEEE 802.15.4a using Energy Detectors," *Radioengineering*, vol. 18, no. 3, pp. 249–257, 2009.

[63] G. Kolumbán, C. Krébesz, T. Tse, and F. Lau, "Derivation of Circuit Specification for the UWB Impulse Radio Transceivers," in *Circuits and Systems, ISCAS 2010, 2010, IEEE International Symposium on*, 2010, p. in press.

[64] L. Couch, *Digital and Analog Communication Systems*, 7th ed. Pearson Prentice Hall, 2007.

[65] G. Fischer, O. Klymenko, and D. Martynenko, "Time-of-Arrival measurement extension to a non-coherent impulse radio UWB transceiver," in *Positioning, Navigation and Communication, 2008. WPNC 2008. 5th Workshop on*, mar. 2008, pp. 265–270.

[66] S. Ghassemzadeh, R. Jana, C. Rice, W. Turin, and V. Tarokh, "A statistical path loss model for in-home UWB channels," in *Ultra Wideband Systems and Technologies, 2002. Digest of Papers. 2002 IEEE Conference on*, 2002, pp. 59 – 64.

[67] T. Gigl, F. Troesch, J. Preishuber-Pfluegl, and K. Witrisal, "Maximal Operating Distance Estimation for Ranging in IEEE 802.15.4a Ultra Wideband," in *Impact on Ubiquitous IT Co-Design to Industry, 2010, International Conference of, Korea-Australia International Conference Alliances (KOALA 2010)*, Jan. 2010, pp. 84–92.

[68] J. Schroeder, S. Galler, K. Kyamakya, and K. Jobmann, "Practical considerations of optimal three-dimensional indoor localization," in *Multisensor Fusion and Integration for Intelligent Systems, 2006 IEEE International Conference on*, sep. 2006, pp. 439–443.

[69] M. Kuhn, C. Zhang, S. Lin, M. Mahfouz, and A. Fathy, "A system level design approach to UWB localization," in *Microwave Symposium Digest, 2009. MTT '09. IEEE MTT-S International*, jun. 2009, pp. 1409–1412.

[70] C. Sturm, W. Sorgel, T. Kayser, and W. Wiesbeck, "Deterministic UWB Wave Propagation Modeling for Localization Applications based on 3D Ray Tracing," jun. 2006, pp. 2003–2006.

[71] I. Zwirello, M. Janson, C. Ascher, U. Schwesinger, G. Trommer, and T. Zwick, "Localization in Industrial Halls via Ultra-Wideband Signals," in *Positioning, Navigation and Communication, 2010 7th Workshop on*, March 2010, p. in press.

[72] The paris simulation framework. Graz University of Technology / NXP Semiconductors. Open-Source (GNU GPL v3). [Online]. Available: http://www.spsc.tugraz.at/research-topics/wireless-communications/paris-osf/

[73] D. Arnitz, "Position Aware RFID systems," PhD thesis, Graz University of Technology, 2011.

[74] D. Arnitz, U. Muehlmann, and K. Witrisal, "Tag-Based Sensing and Positioning in Passive UHF RFID: Tag Reflection," in *3rd Int. EURASIP workshop on RFID Techn.*, Cartagena, Spain, sept 2010.

[75] D. Arnitz, U. Muehlmann, T. Gigl, and K. Witrisal, "Wideband System-Level Simulator for Passive UHF RFID," in *Proc. IEEE Int. Conf. on RFID*, Orlando, Florida, apr 2009.

[76] T. Gigl, P. Meissner, J. Preishuber-Pfluegl, and K. Witrisal, "Ultra-Wideband System-Level Simulator for Positioning and Tracking (U-SPOT)," in *Indoor Positioning and Indoor Navigation, 2010, IPIN2010, IEEE International Conference on*, Sept. 2010.

[77] A. Hong, C. Schneider, G. Sommerkorn, M. Milojevic, R. Thoma, and W. Zirwas, "Experimental Evaluation of Correlation Properties of Large Scale Parameters in an Indoor LOS Environment," in *Wireless Communication Systems, 2006. ISWCS '06. 3rd International Symposium on*, 2006, pp. 55–59.

[78] N. Jalden, P. Zetterberg, B. Ottersten, A. Hong, and R. Thoma, "Correlation Properties of Large Scale Fading Based on Indoor Measurements," in *Wireless Communications and Networking Conference, 2007.WCNC 2007. IEEE*, 2007, pp. 1894–1899.

[79] N. Sirola, "Closed-form Algorithms in Mobile Positioning: Myths and Misconceptions," in *Positioning, Navigation and Communication, 2010 7th Workshop on*, March 2010, p. in press.

[80] T. Gigl, G. J. M. Janssen, V. Dizdarevic, K. Witrisal, and Z. Irahhauten, "Analysis of a UWB Indoor Positioning System Based on Received Signal Strength," in *Proc. 4th Workshop on Positioning, Navigation and Communication WPNC '07*, March 2007, pp. 97–101.

[81] M. Arulampalam, S. Maskell, N. Gordon, and T. Clapp, "A tutorial on particle filters for online nonlinear/non-Gaussian Bayesian tracking," *Signal Processing, IEEE Transactions on*, vol. 50, no. 2, pp. 174–188, Feb. 2002.

[82] D. Simon, *Optimal State Estimation*, 1st ed. Wiley, 2006.

[83] V. Fox, J. Hightower, L. Liao, D. Schulz, and G. Borriello, "Bayesian filtering for location estimation," *Pervasive Computing, IEEE*, vol. 2, no. 3, pp. 24–33, july-sept. 2003.

[84] T. Gigl, "Uwb indoor positioning based on received signal strength," Master Thesis, Graz University of Technology, Delft University of Technology, 2006.

[85] P. Meissner, T. Gigl, and K. Witrisal, "UWB Sequential Monte Carlo Positioning using Virtual Anchors," in *Indoor Positioning and Indoor Navigation, 2010, IPIN2010, IEEE International Conference on*, Sept. 2010.

[86] C. Krall, "Signal Processing for Ultra Wideband Transceivers," in *Doctoral Thesis, Graz Univerisity of Technology*, April 2008.